Ph.D. Program in Civil, Chemical and Environmental Engineering
Curriculum in Chemical, Materials and Process Engineering

Department of Civil, Chemical and Environmental Engineering
Polytechnic School, University of Genoa, Italy.

Simulation of a Natural Gas Steam Reforming Reactor at Different Scales

Federico PUGLIESE

Simulation of a Natural Gas Steam Reformer Reactor at Different Scales

BY

Federico Pugliese

Dissertation discussed in partial fulfillment of
the requirements for the Degree of

DOCTOR OF PHILOSOPHY

Civil, Chemical and Environmental Engineering
curriculum in Chemical, Materials and Process Engineering,
Department of Civil, Chemical and Environmental Engineering, University of Genoa, Italy

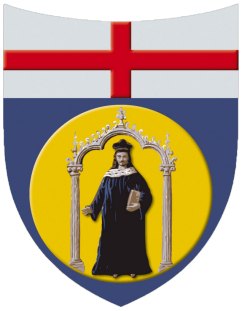

9th April, 2020

Adviser:
Prof. Paola Costamagna – Department of Chemistry and Industrial Chemistry (DCCI), University of Genoa

External Reviewers:
Prof. Alessandro Donazzi – Department of Energy, Polytechnic of Milan
Prof. Henrik Lund Frandsen – Department of Energy Conversion and Storage, Technical University of Denmark

Examination Committee:
Prof. Antonio Barbucci – Department of Civil, Chemical and Environmental Engineering (DICCA), University of Genoa
Prof. Camilla Costa – Department of Chemistry and Industrial Chemistry (DCCI), University of Genoa
Prof. Cristiano Nicolella – Dipartimento di Ingegneria Civile e Industriale (DICI), University of Pisa

Ph.D. program in Civil, Chemical and Environmental Engineering

Curriculum in Chemical, Materials and Process Engineering

Cycle XXXII

Abstract

Simulation of a Natural Gas Steam Reforming Reactor at Different Scales

by Federico PUGLIESE

The concept of sustainable energy is often associated to the so-called hydrogen economy. However, hydrogen cannot be regarded as an energy source, since it is not present in nature as free H_2. Therefore, it must be produced using chemical processes. Among them, natural gas steam reforming (NGSR) is the most widespread and economically feasible process. Natural gas (NG) is a mixture with no well-defined and constant composition. However, methane is the prevailing component (around 85-90%), but also higher hydrocarbons (*i.e.* ethane, propane, butane...) can be found.

NGSR involves the proper endothermic reaction of reforming which produces syngas (a mixture of H_2, CO and CO_2). Then, the slight exothermic reaction of water gas shift, further converts CO in CO_2 producing more hydrogen. The overall process is highly endothermic, so requires a large amount of heat. Therefore, the reactors are tubes placed in a furnace which provides direct heat to the tubes. Even though this process implements a well-established technology, it still presents some issues, such as carbon formation and deposition. Usually, a high steam to carbon (S/C) ratio allows to reduce carbon formation and its deposition: a value of S/C higher than 2.5 is generally believed to be safe for coke-free operation, nevertheless the problem of carbon formation and deposition is still not solved.

The aim of the first part, is the development of an accurate model for these reactors. The mathematical model underlying the chemical and physical system is made of the mass and energy balances. The constitutive equations are then coupled with the kinetic equations for all the reaction involved in the process. The kinetic equations for the NGSR process are retrieved from the literature (*i.e.* Xu and Froment) but, with a simplified approach, they are adapted to our specific case. The overall set constitutes a partial differential and algebraic equation (PDAE) system which and requires boundary conditions which generally are chosen to be flowrate and composition of the feeding mixture. The resolution of the PDAE system needs the implementation of a numerical method through a finite element method (FEM), implemented through COMSOL Multiphysics®. The major problem which has shown up is the numerical method convergence. However, at the end of the simulation it is possible to obtain plots and maps of the main physical and chemical quantities of interest.

Furthermore, an experimental analysis of end-of-life commercial catalyst coming from a full-scale industrial SMR reactor is carried out. This experimental analysis provides interesting results regarding catalyst structure and the eventual carbon deposition. Therefore, a possible qualitative explanation for the carbon formation can be given.

Contents

List of Figures

List of Tables

Chapter 1

An Introduction to the Steam Reforming Process

Clean and alternative energy have become major areas of research worldwide for sustainable energy development. Among the important research and development areas are hydrogen and synthesis gas (syngas) production and purification as well as fuel processing for fuel cells. The researches and technology developments on hydrogen and syngas production, purification and fuel processing for fuel cells have great potential in addressing three major challenges in energy area: (i) to supply more clean fuels to meet the increasing demands for liquid and gaseous fuels and electricity, (ii) to increase the efficiency of energy utilization for fuels and electricity production, and (iii) to eliminate the pollutants and decouple the link between energy utilization and greenhouse gas emissions in end-use systems [1].

The above three challenges can be highlighted by reviewing the status of energy supply and demand and energy efficiency. Figure 1.1 [2] shows the energy supply and demand in the U.S. in 2007 [3]. The existing energy system in the U.S. and in the world today is largely based on combustion of fossil fuels – petroleum, natural gas and coal – in stationary systems and transportation vehicles. It is clear that fossil fuels are the largest sources of primary energy consumption in the U.S. Renewable energies are important but are small parts (6.80%) of the U.S. energy flow, although they have potential to grow.

Figure 1.2 [2] illustrates the energy input and the output of electricity from electric power plants in the U.S. in 2007 [3]. As is well known, electricity is the most convenient form of energy in industry and in daily life. The electric power plants are the largest consumers of coal. Great progress has been made in the electric power industry with respect to pollution control and generation technology with certain improvements in energy efficiency.

What is also very important, but not apparent from the energy supply–demand shown in Figure 1.1, is the following: the energy input into electric power plants represents 41.4% of the total primary energy consumption in the U.S., but the electrical energy generated represents only 35.5% of the energy input. The majority of the energy input into the electric power plants, over 64%, is lost and wasted as conversion losses in the process. The same trend of conversion losses is also applicable for the fuels used in transportation, which represents 28.6% of the total primary energy consumption. Over 70% of the energy contained in the fuels used in transportation vehicles is wasted as conversion loss. This energy waste is largely due to the thermodynamic limitations of heat engine operations dictated by the maximum efficiency of the Carnot cycle.

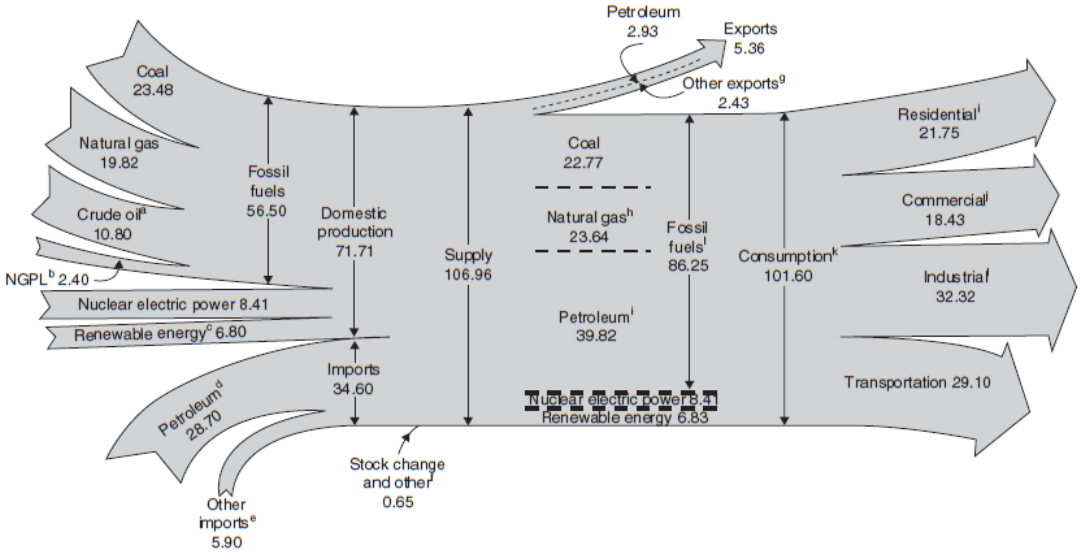

FIGURE 1.1: Energy supply by sources and demand by sectors in the U.S. in 2007 (in quadrillion BTU, 1 BTU = 1.055 kJ) [2].

Therefore, the current energy utilization systems are not sustainable in multiple aspects, and one aspect is their wastefulness. Fundamentally, all fossil hydrocarbon resources are non-renewable and thus it is important to develop more effective and efficient ways to utilise these energy resources for sustainable development. The new processes and new energy systems should be much more energy efficient, and also environmentally benign. Hydrogen and syngas production technology development represent major efforts toward more efficient, responsible, comprehensive, and environmental friendly use of the valuable fossil hydrocarbon resources, toward sustainable development.

Hydrogen (H_2) and syngas (mixture of H_2 and carbon monoxide, CO) production technologies can utilize energy more efficiently, supply ultraclean fuels, eliminate pollutant emissions at end-use systems, and significantly cut emissions of greenhouse gases, particularly carbon dioxide, CO_2. For example, syngas production can contribute to more efficient electrical power generation through advanced energy systems, such as coal-based Integrated Gasification Combined Cycle (IGCC), as well as syngas-based, high-temperature fuel cells such as solid oxide fuel cells (SOFCs) [4]. Syngas from various solid and gaseous fuels can be used for synthesizing ultraclean transport fuels such as liquid hydrocarbon fuels, methanol, dimethyl ether, and ethanol for transportation vehicles.

1.1 Syngas and Hydrogen Production

With gaseous and liquid hydrocarbons and alcohols as well as carbohydrate feedstock, there are many process options for syngas and hydrogen production. They are steam reforming, partial oxidation, and autothermal reforming or oxidative steam reforming. With solid feedstock such as coal, petroleum coke, or biomass, there are various gasification processes that involve endothermic steam gasification and exothermic oxidation reaction to provide the heat *in situ* to sustain the reaction process. Most reactions require (or can be promoted by) specific catalysts and process conditions.

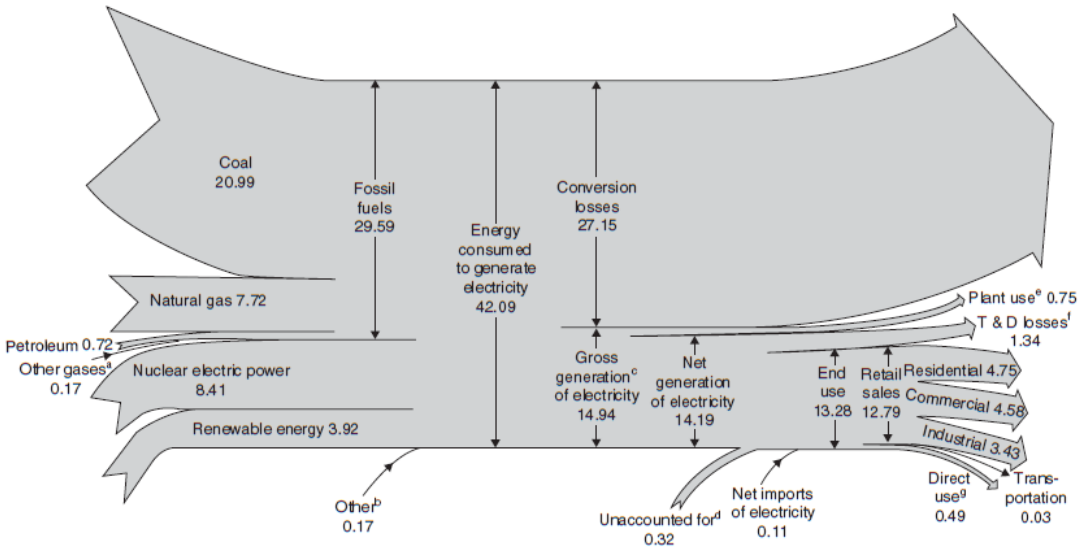

FIGURE 1.2: Energy consumption for electricity generation in the U.S. in 2007 (in quadrillion BTU) [2].

Reforming or gasification processes produce syngas whose H_2/CO ratio depends on the feedstock and process conditions such as feed steam to carbon (S/C) ratio and reaction temperature and pressure. Water gas shift (WGS) reaction ($CO + H_2O \rightleftharpoons CO_2 + H_2$) can further increase the H_2/CO ratio of syngas to the desired range for the following chemical processes. This reaction is also an important step for hydrogen production in commercial hydrogen, ammonia and methanol plants that use natural gas or coal as feedstock.

1.1.1 Options for Hydrogen and Syngas Production

Both non-renewable and renewable energy sources are important for hydrogen and syngas production. As an energy carrier, H_2 (and syngas) can be produced from catalytic processing of various hydrocarbon fuels, alcohol fuels and biofuels such as oxygenates. H_2 can also be produced directly from water, the most abundant source of hydrogen atom, by electrolysis, thermochemical cycles (using nuclear heat), or photocatalytic splitting (although this process is in the early stage of laboratory research).

Current commercial processes for syngas and H_2 production largely depends on fossil fuels both as the source of hydrogen and as the source of energy for the production processing [5]. Fossil fuels are non-renewable energy resources, but they provide a more economical path to hydrogen production in the near term (next 5 – 20 years) and perhaps they will continue to play an important role in the midterm (20 – 50 years from now). Alternative processes that do not depend on fossil hydrocarbon resources for either the hydrogen source or the energy source need to be developed. Such alternative processes need to be economical, environmentally friendly and, of course, competitive. Hydrogen separation is also a major issue as H_2 coexists with other gaseous products from most industrial processes, such as CO_2 from chemical reforming or gasification processes. Pressure swing adsorption (PSA) is used in current industrial practice. Several types of membranes are being developed that would enable more efficient gas separation. Overall, in order for hydrogen energy to penetrate widely into transportation and stationary applications, the costs of H_2 production and

separation need to be reduced significantly from the current technology, for example, by a factor of 2.

1.2 The Steam Reforming Process

Historically, steam reforming has been the most popular method of converting light hydrocarbons to hydrogen. The fuel is heated then injected with superheated steam into the reaction vessel. The steam to carbon (S/C) ratio is usually around 2.5 to force the reaction to completion as well as to inhibit soot formation. However, developers strive for lower ratios to improve cycle efficiency. Steam reforming is usually carried out using nickel-based catalysts whose activity depends on metal surface area. Steam reforming is endothermic, thus favoured by high temperatures.

The exothermic water-gas shift reaction occurs in the steam reformer reactor since WGS is catalyzed by the same Ni-based catalyst of steam reforming. However, the combined reaction, steam reforming and water gas shift, is endothermic. As such, an indirect high temperature heat source is needed to operate the reactor. This heat source usually takes the form of an adjacent, high-temperature furnace that combusts a small portion of the fuel. Efficiency improves by using rejected heat from other parts of the system.

Steam pre-reforming of hydrocarbons, as a process step in the manufacture of hydrogen, ammonia, methanol, carbon monoxide, and syngas, is an established technology. All higher hydrocarbons are converted over a nickel-based catalyst into a gas mixture containing hydrogen, methane, and carbon oxides. Establishment of methanation and shift reaction equilibria at the process conditions determines the composition of the pre-reformed gas. By proper design of fuel processing systems, a wide variety of fuels may be converted to a suitable reformate. For each type of fuel, optimum operating parameters such as temperature, S/C ratio, and catalyst must be established.

One of the most cost effective and industrially established methods to produce hydrogen is through steam reforming of hydrocarbons (especially methane), which accounts for over 40% of the world's hydrogen production [6]. However, the expression reforming could be misleading due to its use for the well-known process to improve the octane number of gasoline. Some authors suggested calling this process oxygenolysis (analogously to pyrolysis and hydrogenolysis) because it produces a gaseous mixture from hydrocarbons thanks to oxygen atoms.

Steam reforming process is an oxidative method to produce H_2, such as autothermal reforming and partial oxidation, with the method's general reaction scheme given by Muradov [7]:

$$C_nH_m + nH_2O \rightleftharpoons nCO + \frac{n+2m}{2} H_2 \tag{1.1}$$

where water acts as an oxidant. In this case, the reaction is highly endothermic (i.e. $\Delta H_{298K} > 0$ kJ mol^{-1}). Since the reactant mixture is rather inert, catalysts are widely used to accomplish these processes at the practical range of temperatures (between 750 °C and 950 °C) [7].

In industrial practice, the overall process includes a desulphurisation unit (DSU), where sulphur is removed from natural gas (NG). Subsequently the higher hydrocarbons (C2+) in NG are converted to CH_4, carbon oxides and H_2 in a pre–reforming

(PreRe) unit, and then they are directed to the MSR catalytic packed–bed multitubular reactor, where hydrogen is produced in substantial quantities along with carbon oxides. Carbon monoxide is further reduced in two sequential water-gas shift (WGS) adiabatic reactors, the high (HT) and the low temperature (LT) WGS reactors, which provide a further source of H_2. The latter is separated from CO_2 usually in pressure swing adsorption (PSA) units. Depending on the amount of carbon monoxide remaining after the WGS reactors and the final use of the produced H_2, CO concentration can be further diminished in the methanator, or the preferential oxidation (PrefOxid) unit.

Figure 1.3 [6] illustrates the simplified process flow sheet. Steam is needed in order to facilitate the reforming reactions in both the MSR and the WGS reactors: in the latter, the unreacted steam coming from the MSR unit might be adequate without the need for providing additional quantities.

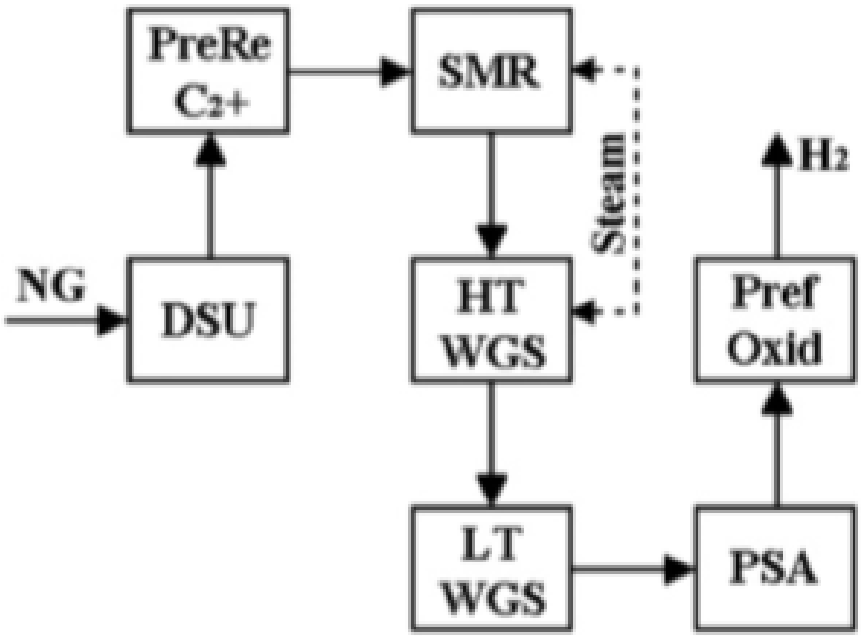

FIGURE 1.3: Simplified process flow sheet of H_2 production from NG [6].

The main reactions of the MSR scheme are the following comprising an overall endothermic set [8]:

$$CH_4 + H_2O \rightleftharpoons CO + 3\,H_2 \qquad \Delta H^0_{298K} = 206.63\,\text{kJ mol}^{-1} \tag{1.2}$$

$$CO + H_2O \rightleftharpoons CO_2 + H_2 \qquad \Delta H^0_{298K} = -41.16\,\text{kJ mol}^{-1} \tag{1.3}$$

$$CH_4 + 2\,H_2O \rightleftharpoons CO_2 + 4\,H_2 \qquad \Delta H^0_{298K} = 165.47\,\text{kJ mol}^{-1} \tag{1.4}$$

For reactions 2.1-2.3 a Langmuir–Hinshelwood mechanism can be established using $Ni/MgAl_2O_4$ as a catalyst [8]. It could also be proven that only two reactions are independent with the third being a linear combination of the others.

1.2.1 A Brief History of the Steam Reforming Process

1.2.1.1 Early work

The catalytic interaction between hydrocarbons and metals was already observed in 1817 by H. Davy during his experiment with the wire-gauze safety-lamp. Davy also recognised the disturbing actions of carbon and sulphur (causing severe problem in steam reforming) before the introduction, made by Berzelius in 1863, of the concept of catalysis.

A process for conversion of hydrocarbons into hydrogen in presence of steam was described by Tessie du Motay and Maréchal in 1868. The hydrocarbons and steam were passed over calcium oxide resulting in the formation of calcium carbonate and hydrogen. The application of nickel for this process was claimed in 1889 by Mond.

At the same time, Lang studied the homogeneous reaction between steam and methane. The experiments, which were performed at molar ratio H_2O/CH_4 of unity, resulted in very small conversion even at 1220–1320 K. Moreover, the reaction was accompanied by the formation of coke.

Although some industrial interest was reflected by patents of Dieffenbach and Moldenhauer in 1909, and by BASF (Mittasch and Schneider) in 1912, Sabatier did not mention steam reforming in his book published in 1920 which, among other topics, summarised his comprehensive studies of nickel-catalysed reactions.

The first detailed study of the catalytic reaction between steam and methane to be published is apparently that of Neumann and Jacob from 1924. The experiments resulted in gas mixtures close to the equilibria of reactions 2.1 and 2.2. Shortly after, an increasing interest developed in utilizing the reforming reactions for industrial conversion of natural gas or methane-rich gas into synthesis gas or hydrogen. This resulted in numerous patents issued around 1930 among which, one described a process where the catalyst was placed in externally heated tubes of alloy steel. A broad range of catalyst compositions was claimed as for example "catalyst consisting of iron, nickel or cobalt activated by the addition of other metals or metallic compounds. As activating agents, metals whose oxides are reducible with difficulty, or compounds thereof, are especially useful, e.g. chromium, vanadium, and compounds of alkali, alkaline earth, and earth metals, such as potassium, magnesium, and aluminium" [9] or more simply "a substance comprising a metals of the iron group with an activating addition of non-reducible oxide of metals from group II to VI of the periodic system" [10].

1.2.1.2 Industrial development

The first industrial reformer was installed at Baton Rouge by Standard Oil of New Jersey and commissioned in 1930. Six years later a steam reformer was commissioned at ICI, Billigham. The reforming process was adopted in the US where natural gas was abundantly available as feedstock.

During the fifties light distillate naphthas became an economical feedstock for steam reforming in Europe. At the same time, metallurgical development made it possible to design reformers for operation at elevated pressures. This improved the energy efficiency of the overall process because higher pressures facilitate heat recovery and partly results in savings in compression energy in methanol and ammonia plants. In 1962, two tubular reformers operating at around 1.5 MPa (15 bar) and using high

molecular weight hydrocarbons as feed were commissioned by ICI. Less than five years later, a Topsøe reformer was operating at 4 MPa (40 bar).

Another route for naphtha reforming was followed by the British Gas Council patent where Dent *et al.* [11] described a process for adiabatic gasification of naphtha. The first plant based on these principles (the CRG process) was commissioned in 1964. Similar processes were developed by Lurgi and JGC.

1.2.1.3 Present trends and future aspects

Today steam reforming is a principal process for hydrogen and synthesis gas production. The most important alternatives are partial oxidation of fuel oil and gasification of coal. However, the capital costs of a fuel oil based ammonia plant are approximately 1.5 times and for a coal based plant approximately twice that of an ammonia plant using steam reforming of natural gas. Moreover, the energy consumption for the two alternatives is larger (approximately 20% and 50% respectively) than for steam reforming. Therefore, the use of alternatives to steam reforming can be justified only in the case of an attractive price difference between heavy oil fraction or coal and the hydrocarbons feedstock for steam reforming.

Today, more than 80% of the world ammonia production is based on steam reforming of hydrocarbons. Natural gas, which alone accounts for 70%, is the preferred feedstock in almost all new plants. This is not surprising in view of the high thermal efficiency (Table 1.1 [12]). Forecasts of the future use of fertilizers mainly in developing countries indicate a substantial growth in steam reforming.

TABLE 1.1: Energy consumptions for various applications of steam reforming of NG [12].

Product	**Energy consumption** [GJ t^{-1}]		**Thermal efficiency** [%]
	practical	theoretical	
Ammonia[A]	27-31	20.9	72 (66)[A]
Hydrogen	178	100	63
Methanol	27-31	17.5	60
Gasoline	≈ 74	≈ 40	≈ 54
Sponge iron *via* direct reduction	10-125	7.1	60-70

[A] N_2 added with air, product as liquid ammonia.

Oil refineries are using more and more hydrogen mainly because of increased demands for desulphurisation and hydrocracking. The available amounts of by-product hydrogen (from catalytic reforming etc.) have not been sufficient to cover the needs, and in particular, in Japan and the U.S. (also in Italy) the gap is being filled by steam reforming or by partial oxidation of heavy feedstock. The requirements for hydrogen will further increase with the processing of more heavy hydro deficient feedstock such as tar sands.

The choice of feedstock for steam reforming is influenced by regional availabilities of hydrocarbons. In Japan and India naphtha is still an important feedstock for steam reformers, but elsewhere natural gas is dominating. After the discovery of natural gas in Western Europe, many European town gas units, which were previously based on naphtha, were closed or converted into using natural gas as feedstock. In the U.S.,

natural gas is still easily available, although some industrial plants based on natural gas have been forced to look for alternative feedstock.

The huge amounts of natural gas being flared jointly with oil production at many locations represent a challenge to chemical technology. It has been considered to convert the gas into transportable energy carrier, when pipelines to consumers cannot be established. Large-scale conversion of natural gas via steam reforming into full methanol as suggested after the oil crisis in 1973. This would soon dwarf the present methanol production for petrochemical use. However, so far this solution has not been feasible compared to transport of liquefied natural gas (LNG).

Many natural gas resources are located offshore or at coastal areas with difficult access. Several of these resources are of minor size which cannot justify the construction of a pipeline to a LNG plant. In this situation it ca be attractive to operate barge mounted ammonia o methanol plants, which can be transferred to a new location when the field is exhausted.

Sufficiently high energy prices may justify the use of fuel methanol. If so, this would probably also lead to the introduction of natural gas based gasoline, manufactured by the further conversion of methanol into gasoline via the Mobil MTG process.

The steam reforming process is an important element in compact fuel cell system based on natural gas or liquid hydrocarbons. The reforming step produces the hydrogen for the fuel cell and excess gas is used as fuel for the reforming process. Units with a capacity up to 24 MW are under construction.

A special application of the steam reforming process is the German ADAM/EVA system in which it is foreseen to use hot helium from a high temperature gas cooled nuclear reactor as heat source for the reforming reaction. The produced carbon monoxide and hydrogen is transported over long distances to cities where the reaction heat is recovered by the methanation reaction (the opposite of reaction 2.1) and utilised for the production of electricity and hot water for district heating. The produced methane is therefore recycled to the reformer. The helium heated reforming system may also be used for col liquefaction. A similar reactor system has been studied in Japan for steel production.

The endothermicity of the steam reforming reactions is also utilised in explorative studies on the conversion of solar into chemical energy. The solar energy might be transferred via a sodium heat pipe. Another future application may be steam reforming of gasoline or methanol for combustion engines using the hot exhaust gas as heating medium.

1.2.2 The Steam Reforming Reactor

Even if different kind of steam reforming reactor has been developed during the years, in industrial practice, the multi-tubular reactor is widespread. Steam reforming is realised in ovens, which are equipped with burners whose radiant zone is filled with steel cast tubes full of catalyst.

The burners provide the heat reaction directly and indirectly: the flame radiate the tubes and the flue gas pre-heat the feedstock. The remaining heat is then recovered by a series of heat exchangers so it is fundamental to design the reactor and the plant to allow optimal heat recovery in order to achieve the highest energy efficiency.

Other arrangements of steam reformer reactor include:

- heat exchanger reformers
- plate steam reformers
- membrane reactors.

The first type of reactor consists in a heat exchanger where the reaction heat is provided by a process gas flow, which warms up the reacting mixture in catalyst-filled tubes. This configuration is usually associated with a fuel cell plant to pre-treat the feedstock. In this case, the advantage is related to the lower capital cost due to the smaller dimension of the reactor.

Even plate steam reformers are used in fuel cell plants: the reactors are fed, at one side, with the waste gas from the anode that, while it is burning, provides the heat for the steam reforming reaction taking place on the other side of the reactor.

Membrane reactors represent the new frontier for steam reforming. They allow the simultaneous management of MSR, WGS and, thanks to a highly hydrogen selective palladium membrane, to H_2 purification. All these aspects lead to a simplification of the flow sheet and a reduction of capital costs. The increasing interest in this kind of reactors is not only devoted to industrial plants but also for fuel cells systems.

However, considering the tubular reactors, which are the most used type, they could show different constructive arrangements that could be summed up in:

- furnace design (tube and burner layout)
- tube design
- burner design.

1.2.2.1 Furnace design

The reformer consists essentially of two main sections: the furnace, containing the tubes loaded with catalyst, and the convection section, where heat is recovered from the flue gas by duties as preheating feedstock, process air and/or combustion air, boiler feedwater heating and steam raising and superheating. The steam reforming reactions are usually carried out at pressures up to 35 bar at temperatures of 800 °C or higher, while the flue gas may reach temperatures over 1000 °C. Consequently, the design of the reformer is complex and depends on the duty and on the philosophy of the contractor engineering the plant. The furnace can be top-fired, terrace wall-fired, side-fired or, in the case of small hydrogen plant, bottom-fired. Typical throughput, which is usually expressed as the amount of steam plus feedstock per hour per litre of catalyst, is in the range 2–7 $kg\,l^{-1}\,h^{-1}$ with a heat flux of 170–430 $MJ\,m^{-2}$. The overall length of reformer tubes is usually in the range 7.5–12 m although the heated charged length may be up 9 m; tube diameter usually lies between 7 and 13 cm. The number of tubes depends on output, and for a large reformer there may be as many as 650 tubes.

Figure 1.4 [13] shows schematic arrangements of a top-fired and a terrace wall-fired furnace, with associated heat recovery sections and transfer ducts.

Apart from a few examples, the reformer catalyst tubes are heated up in a fired furnace. Four representative furnace types characterised by the displacement of burners are shown in Figure 1.5. In the side-fired furnace radiant type burners are placed in several rows on the two-side walls of the furnace chamber. The tubes are placed in single rows in the furnace chamber. In another type, the burners are placed in terraces at the side walls. A common type uses burner placed at the top of the furnace. This arrangement has several rows of tubes in the same furnace box separated by burner

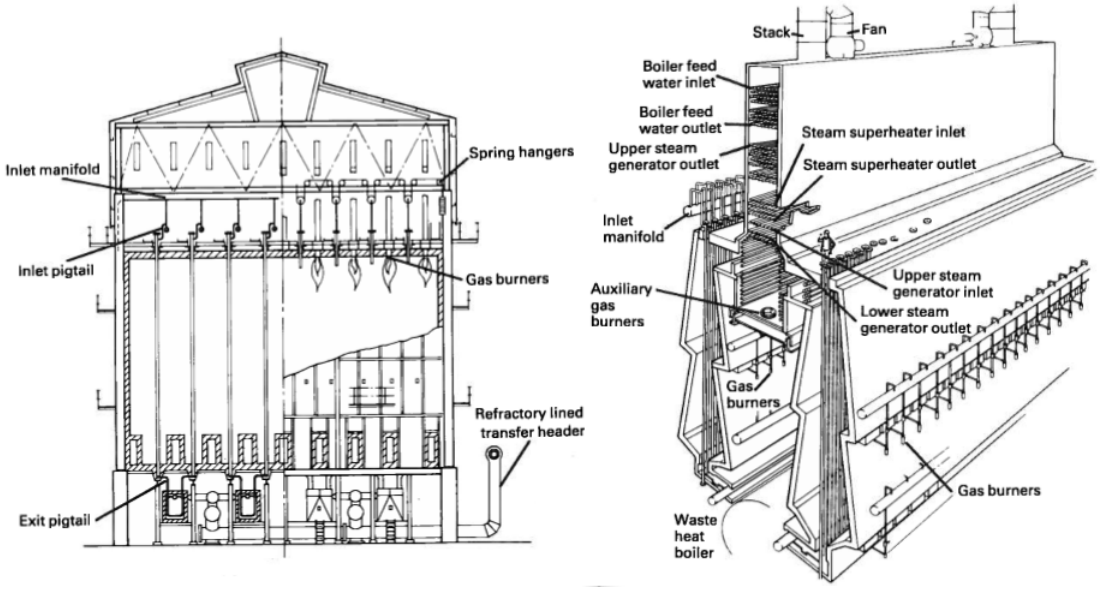

FIGURE 1.4: Schematic arrangement of a top-fired (left) and terrace wall-fired (right) furnace based on the ICI reformers at Billingham [13].

rows in the furnace ceiling. Burner may also be placed in the bottom of the furnace. Top and bottom furnaces use long flame burners. While the side-wall radiant type furnace is very flexible in adjusting firing profiles, the top-fired may provide a more compact design with a smaller number of burners.

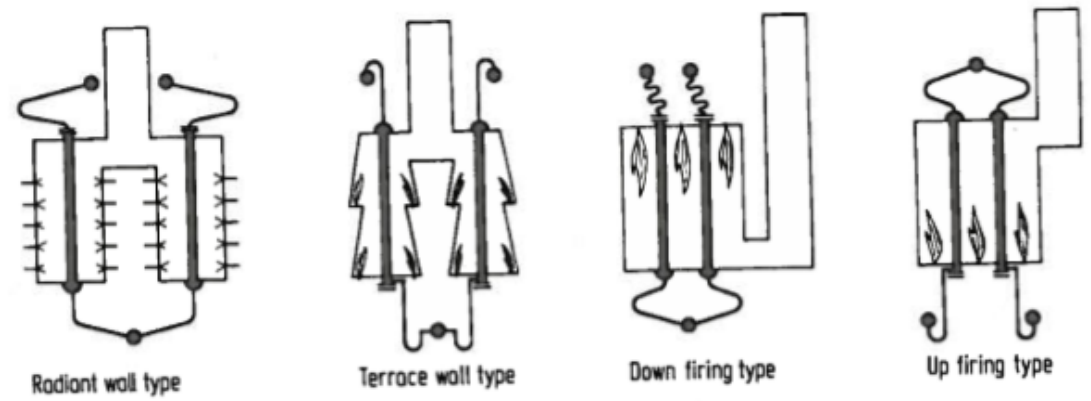

FIGURE 1.5: Typical configuration of reformer furnace [12].

1.2.2.2 Tube design

It is necessary to contain the steam reforming catalyst at high pressure and high temperature in a way that permits the transfer of sufficient heat to satisfy the endothermic reaction taking place on the catalyst.

Conventional steel tubes do not possess the material characteristics to withstand the pressure and temperature at which a modern reformer operates. A suitable cost-effective material is chromium/nickel alloy (ASTM A297HK) with the following composition (%w/w):

- chromium 24–28%
- nickel 18–22%

- carbon 0.35–0.45%
- manganese, silicon 2% (each)
- phosphorus, sulphur 0.05% (each)

The melting point of the alloy is close to 1370 °C and it is suitable for use at temperatures up to 1150 °C. Other materials such as Pyrotherm G24/24Nb and Manaurite 36X can also be used, since they allow operation of the reformer at higher temperatures and pressures. However, they are more expensive but they are now used by a growing number of operators.

The tubes are manufactured by centrifugal casting (spun-cast) in approximately 3 to 6 metres section and these are welded together to produce a tube of the required length. Spun-cast tubes, even at normal and particularly at occasional abnormal transient operating temperatures, generate very high stresses and these are minimised by using as thin a tube wall as possible. All weld protrusions should be machined of to minimise tube stresses at welds and prevent catalyst hold-up. If the diameter of the reformer tubes is too great, heat transfer to the catalyst in the centre of the tube will be restricted and the reaction rate limited; on the other hand, if tube diameter is too small, the pressure drop will be high. Moreover, with small-diameter tubes, a smaller catalyst will also be required and this will increase further the pressure drop. Most designers consider the optimum tube size between 7 and 13 cm internal diameter, depending on the feedstock, the catalyst and the required composition of the reformed gas.

During operation, there is a gradation of temperature longitudinally from the inlet to the outlet of the tube, as well as radially across the wall of the tube. Creep occurs with time at normal operating pressures and temperatures. The temperature experienced by the tube wall depends on the distribution of heat input and the heat absorbed by the reaction taking place on the catalyst in the tubes. Uneven heat input and catalyst activity caused by uneven packing or poisoning will cause local overheating, resulting in excessive creep in that locality, which will hasten tube rupture. Normally reformers are designated with a tube life of about 100 000 h (10 years) using creep strength data based on creep-rupture tests on varying duration from number of sources.

A correlation derived by ICI are reported in the form of a Larson–Miller diagram (Figure 1.6), which summarises the results of 170 rupture test on 25/20 chrome-nickel alloy at different temperatures and pressures. The higher the temperature and pressure are, the greater the creep and the shorter the tube life. This applies to all parts of each tube, and if part of any tube is subjected consistently to higher-than-average temperatures it will fail prematurely.

1.2.2.3 Burner design

Reformers' burners are manufactured by a small group of industries. Some years ago, their development was only oriented to regulate the flame radiation through flame shape and combustion extent. However, nowadays, with the increasing attention to environmental problems (such as NO_x and SO_x control), more and more attention is placed on the combustion taking place in the burners.

Furnace-side modeling, thanks to Computational Fluid Dynamics (CFD), allows a better comprehension of the phenomena involved so it is possible to deeper understand how to design properly the burners and enhance the reformer performances.

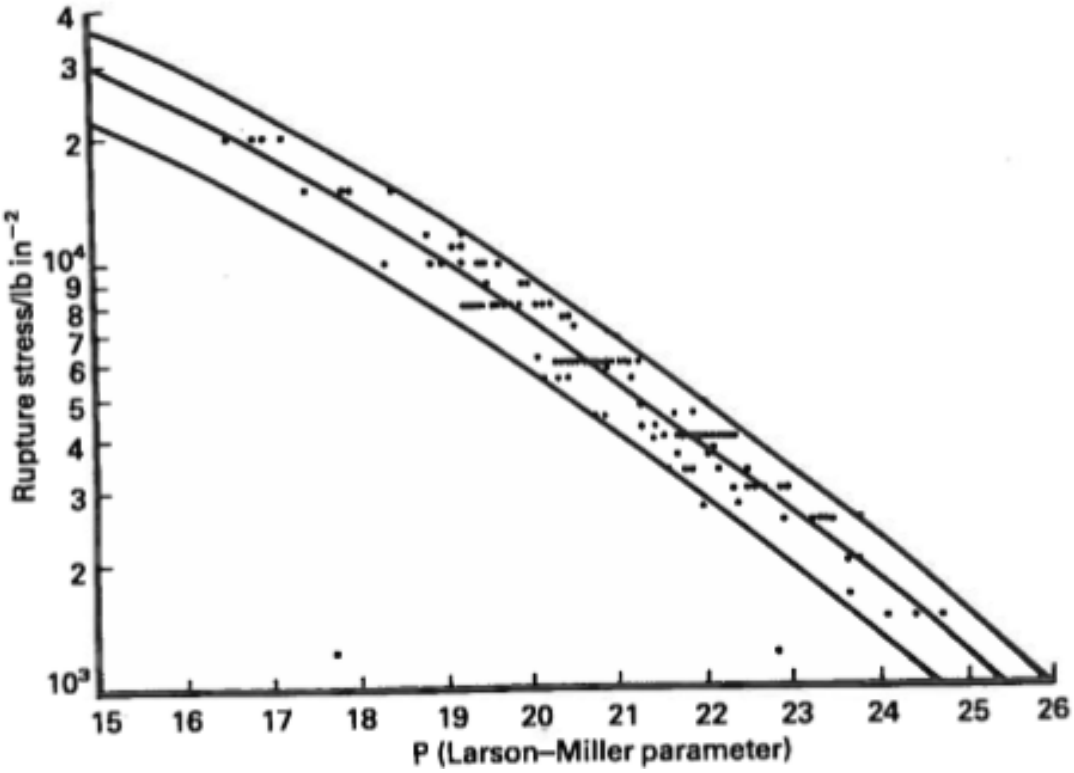

FIGURE 1.6: Larson–Miller diagram. P is given by the formula $P = 10^{-3} \cdot T \cdot (C + \log t)$ where T is the temperature (K), C is a constant (in this case 15) and t is the time (h) [13].

1.2.3 Catalysis of the Steam Reforming

To promote reaction 2.1 to hydrogen and carbon monoxide, and avoid methanation (the reaction which produces methane from H_2 and CO or CO_2) it is necessary the use of a catalyst and appropriate operative conditions. The majority of steam reforming catalyst are made of nickel, as active phase, supported on magnesium aluminate ($MgO–Al_2O_3$ or $MgAl_2O_4$). Other elements, which can substitute the nickel as catalyst, are cobalt and noble metals but the disadvantage is their high cost that hinders large-scale production. Despite the cost, ruthenium and rhodium guarantee a higher activity for surface area than nickel.

From a physical point of view, the catalyst is made of a refractory alkaline alumina support on which particles of nickel are deposited. The role of the support is to limit deactivation by means of carbonaceous residue.

Each catalyst should be optimised to the specific role it has to cover: for example, catalyst for pre-reformer are different from the one for the actual reformer. The design of this process set the necessity that the catalyst bed favour at its best heat transmission and low pressure drop.

Generally, the widespread catalyst is $Ni/MgAl_2O_4$ containing 20–30% wt/wt of active metals (referred to nickel). Sometimes they are doped with potassium, which over time will be dispersed in the gaseous phase [12].

In the industrial practice, catalysts are extruded into pellets with different shapes to reduce pressure drops. Every producer shapes the catalyst in different forms, which

are supposed the adequate to achieve the expected outcomes. For example, Figure 1.7 displays representative Johnson Matthey NGSR catalyst pellets.

FIGURE 1.7: Representative image of the Johnson Matthey catalyst [14].

Apart the chemical role between the catalysts and the reaction environment, the most important subject is their deactivation, in other words the loss of efficiency during their operative life. This phenomenon, in steam reforming processes, can be caused by:

- sintering
- poisoning
- carbon deposition.

1.2.3.1 Carbon deposition

Steam reforming of hydrocarbons involves the risk of carbon formation, which may cause serious operational problems. All hydrocarbons will spontaneously decompose into carbon and hydrogen via the general reaction:

$$C_nH_{2n+2} \rightleftharpoons nC + (n+1)\,H_2 \tag{1.5}$$

which in case of methane is:

$$CH_4 \rightleftharpoons C + 2\,H_2 \tag{1.6}$$

For naphtha, the decomposition is more complex because carbon is formed not only by direct thermal cracking (React. 1.5) but also from various intermediates, in particular unsaturated species. In the presence of steam, and in particular with steam amounts lower than the stoichiometric quantity, other carbon forming reactions become possible. These are the disproportionation and reduction of carbon monoxide (React. 1.7 and 1.8, respectively):

$$2\,CO \rightleftharpoons C + CO_2 \tag{1.7}$$

$$CO + H_2 \rightleftharpoons C + H_2O \tag{1.8}$$

When methane or naphthas are reformed, the formation of carbon within the nickel catalyst can be prevented by ensuring the S/C ratio exceeds a minimum value as it has been demonstrated by various studies (*i.e.* PIP-SOFC, 2004).

Carbon may be formed via different routes, each influencing its morphology. The most common types are:

- whisker-like
- encapsulating
- pyrolytic.

Whisker carbon It is well known that the reaction of hydrocarbons as well as carbon monoxide over transition metals can lead to the formation of filamentous carbon. The carbon grows typically in a whisker-like structure with a nickel particle at the top (Figure 1.8) and the strong whiskers may result in breakdown of the catalyst particle.

Studies with electron microscopes show the presence of tubular filaments with a coaxial channel. The whisker diameter is very close to that of the nickel crystal, which is often pear shaped (Figure 1.8), indicating a reconstruction during carbon formation of the nearly ideally shaped nickel crystals. The carbon structure is graphitic with the basal planes parallel to the long axis of the whisker. Simultaneously formation of flake-like carbon could occur. The growth rate of the whiskers is independent of time meaning that large amount of carbon can accumulate. This is in contrast to carbon formation in catalytic cracking where carbon deactivates the active site forming the carbon. In some situations, the whisker growth may cease because the nickel crystal becomes encapsulated in carbonaceous deposits. The whisker growth rate in the absence of steam is not significantly influenced by the support nor the presence of alkali.

FIGURE 1.8: Whiskers growth by diffusion through nickel particles (left) and electron micrograph of whisker-like carbon formed by decomposition of methane on nickel catalyst at 500 °C (right) [12].

Encapsulating polymer The adsorbed hydrocarbon may react into a film of non-reactive deposits, which might encapsulate and deactivate the nickel surface. The phenomenon was observed while studying the decomposition of pure hydrocarbons to form graphitic encapsulating carbon, and at steam reforming conditions at low temperature to form gum-like material.

In adiabatic reformers the resulting deactivation causes a continuous movement of the temperature profile in the flow direction as illustrated in Figure 1.9.

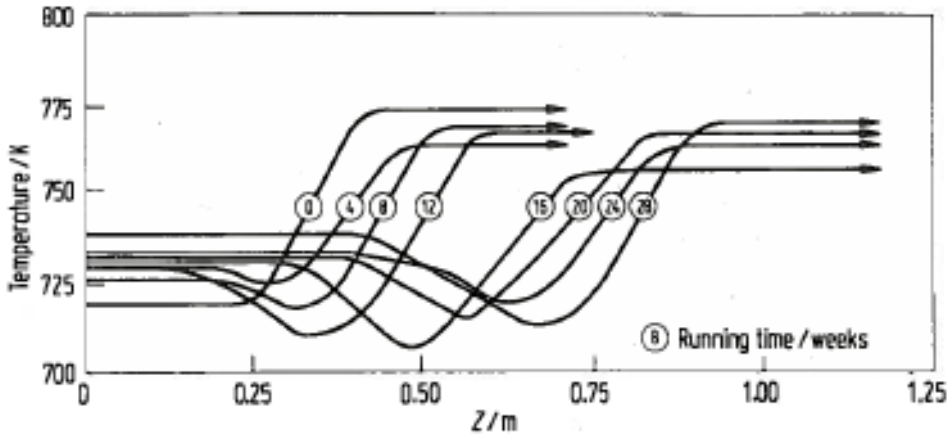

FIGURE 1.9: Progression of temperature profile in adiabatic steam reforming. Data from industrial operation with CRG–process. Feed: light naphtha, S/C=1.6, p = 1.7 MPa [12].

FIGURE 1.10: Coke deposit formed by pyrolysis of light paraffins. The coke was deposited in tubular reformer operating with nearly inactive catalyst at the inlet [12].

Pyrolytic carbon The steam reforming reactions on the nickel surface may be accompanied by thermal cracking reactions (steam cracking), which may start at temperatures above 920 K. In fact, a steam/naphtha reformer with a completely deactivated nickel catalyst, will work as a steam cracker producing olefins. Therefore, the risk of carbon formation is to be analysed in the same way as for a steam cracker.

It is generally agreed that the gas film at tube wall is overheated and acts as a source of radicals and coke precursors. In steam crackers the tube skin temperature is the most important parameter determining the rate of coke formation. Moreover, the coking reactions are related to the so-called kinetic severity function (KSF):

$$KSF = \int k(T)dt \tag{1.9}$$

which describes the residence time-temperature history of the reactants in a way that is consistent with kinetics. This means that for a given temperature profile the risk of carbon formation is increased with higher residence time. The catalyst filling has an influence on these parameters, first by changing the film volume and secondly by influencing the residence time distribution via the void fraction. Moreover, the nickel and the surface acidity of the catalyst will promote the formation of coke deposits

from the tar-like intermediates.

The pyrolytic coke is normally found as dense shales on the tube wall as shown in Figure 1.10, or as deposits encapsulating the catalyst particles and eventually filling out the void between the particles.

1.3 Aim of This Work

This work of thesis focuses on Natural Gas Steam Reforming (NGSR) chemical reactors and their simulation. Normally, NGSR reactors are fed with commercial natural gas from the national network (with a methane content around 85-95% vol.), and transform it into hydrogen through the reaction with water vapour. Despite these reactors implement a well–established technology, they still present some issues; in particular, the formation and consequent deposition of carbon, which can coat the active sites of the catalyst, inhibiting its activity and limiting the diffusion of reactant gas into the catalytic bed. This deposition starts at some critical points and then expands over time, generating an increase of pressure losses and causing a reduction of conversion due to catalyst deactivation. At present, the strategic importance of steam reforming reactors is increasing, also due to their application in fuel cell plants.

This work could be enclosed in a major project, which proposes a multidisciplinary approach to the development of a system for early detection and prediction of coke deposition. The prognostic function (prediction of the eventual coke formation) aims at increasing significantly the lifetime of the catalyst inside the reactor, by sending alert messages that suggest modifying the operating condition of the NGSR reactor when the risk of coke deposition occurs. If, nevertheless, coke deposition takes place, the diagnostic function enables an early detection and accurate localization. This has a twofold purpose: restoring the catalyst by means of cost-effective targeted actions (regeneration, partial substitution, etc.), and reducing the likelihood of damage to the unit-operations downstream the reactor itself. The latter scenario is particularly relevant in the case of fuel cell systems, which can suffer irreversible damage if fed with hydrogen containing a significant amount of methane, which is the case when a coke deposition fault takes place in the NGSR reactor.

1.3.1 Methodology

The in-depth knowledge of physical and chemical laws that govern the NGSR reactor are the basis for the development of a quantitative mathematical model, embedding a kinetics model for coke deposition. The model is thus based on

1. microscopic balances of mass, energy and momentum, written in transient form;
2. appropriate boundary conditions;
3. appropriate expressions for constitutive laws, in particular chemical kinetics.

Concerning chemical kinetics, this is the core of the simulation model, whose reliability depends on its detailed knowledge. Therefore, in this work a deep research will been done to find the best rate laws for NGSR.

The model equations form a PDAE (Partial Differential and Algebraic Equation) system, which will be integrated numerically by a finite element method, will be implemented through the software COMSOL Multiphysics. The result will be 3D time-dependent distribution of all the chemical-physical parameters inside the NGSR reactor, in particular composition, temperature and pressure of the reactant gas. In the

validation phase, the results of the model will be compared to experimental data provided by IPLOM. On the one hand, this comparison will allow to identify and include in the model possible significant phenomena, which might have been neglected during the early development phases. On the other hand, this will ensure the reliability of the final simulation tool, necessary to provide a basis for designing a robust diagnostic and prognostic system.

The simulation model of the NGSR reactor offers the possibility of addressing the system diagnostics through the classic model-based philosophy, relying on the comparison between the values of the physical-chemical variables measured in the reactor, and calculated by the model under the hypothesis that the reactor works perfectly. In addition, the localization of the fault will be based on pattern recognition techniques, suitably trained. The use of pattern recognition techniques, coupled to the use of an extended training-set, is typical of data-driven diagnostics methods. Therefore, in line with a trend currently at the cutting edge of research, the project will develop a hybrid (or combined) diagnostic approach, where typical elements of the datadriven methodology are incorporated into a classical model-based context.

The availability of a quantitative model of the NGSR chemical reactor will be valuable also for the development of the prognostic function, since predictive techniques can be based on model-based approaches, increasingly hybridized by incorporating elements typical of the datadrive approach. Therefore, both the diagnostic and prognostic functions will be developed within the same framework. The quantitative model will be used (i) off-line, to create the dataset necessary for the statistical modelling and the training of the statistical prediction and regression tools; and (ii) on-line, to enable the real-time computation of the residual vector which is an input for the prognostic and diagnostic tools.

Chapter 2

Local Kinetics of SMR and WGS Reactions over Homemade and Commercial Catalyst

Three Ni-based natural gas steam reforming catalysts, *i.e.* commercial JM25-4Q and JM57-4Q, and a laboratory made catalyst (26% Ni on a 5% SiO_2–95% Al_2O_3), are tested in a laboratory reactor, under carbon dioxide methanation and methane steam reforming operating conditions. The laboratory catalyst is more active in both CO_2 methanation (equilibrium is reached at 623 K with 100% selectivity) and methane steam reforming (92% hydrogen yield at 890 K) than the two commercial catalysts, likely due to its higher nickel loading. In any case, commercial steam reforming catalysts also show interesting activity in CO_2 methanation, reduced by K-doping.

To support the interpretation of the experimental results, a pseudo-homogeneous packed-bed reactor model is developed, embedding the Xu and Froment local kinetics, with appropriate kinetic parameters for each catalyst. In particular, the H_2O adsorption coefficient adopted for the commercial catalysts is about two orders of magnitude higher than for the laboratory made catalyst, and this is in line with the expectations, considering that the commercial catalysts are added with Ca and K which may promote water adsorption. The simulation model allows to identify and account for thermal effects occurring inside the catalytic zone of the reactor and along the exit line.

2.1 Introduction

Hydrogen is mostly produced today through steam reforming of natural gas [15, 16]. The main reaction is assumed to be represented by steam methane reforming (SMR), an endothermic equilibrium reaction:

$$CH_4 + H_2O \rightleftharpoons CO + 3\,H_2 \qquad \Delta H^0_{298K} = 206.63\,\mathrm{kJ\,mol^{-1}} \tag{2.1}$$

establishing together with the water gas shift (WGS) equilibrium:

$$CO + H_2O \rightleftharpoons CO_2 + H_2 \qquad \Delta H^0_{298K} = -41.16\,\mathrm{kJ\,mol^{-1}} \tag{2.2}$$

resulting, at least formally, in a formal "global reforming reaction" (GRR):

$$CH_4 + 2\,H_2O \rightleftharpoons CO_2 + 4\,H_2 \qquad \Delta H^0_{298K} = 165.47\,\mathrm{kJ\,mol^{-1}} \tag{2.3}$$

thus producing a "syngas" containing H_2, CO, CO_2 and unreacted CH_4. Although most authors suppose that the reaction path implies SMR being the first step followed by WGS to give the "formal" GRR reaction, is also possible that GRR is the first real step followed by the reverse of WGS (revWGS) to give the "formal" SMR reaction. The reaction is usually realized at 1000÷1200 K, 30÷50 bar.

Typical methane steam reforming catalysts [17] contain 10-25 wt% Ni supported over a low-surface-area refractory oxide such as alpha-alumina, Mg aluminate spinel $MgAl_2O_4$, calcium aluminates and calcium-potassium aluminate $CaK_2Al_{22}O_{34}$. A typical effect of this reaction consists in the production of carbon residue, in particular "carbon whiskers" or nanotubes, which accumulate in the catalyst bed, clogging it and causing pressure drop and deactivation. The presence of additives in some commercial catalysts allows the reduction of the formation of carbon residues. In particular, potassium has a very positive effect in reducing the formation rate of carbon species, with the drawback of reducing slightly the catalytic activity of the catalyst [18].

Hydrogenation of CO_2 (MCO2) can produce several different products, among which methane and CO. Methanation reaction consists in the synthesis of methane from hydrogenation of COx. Formally, methanation of carbon monoxide (MCO) is the reverse of SMR (MCO = revSMR):

$$CO + 3\,H_2 \rightleftharpoons CH_4 + H_2O \qquad \Delta H^0_{298K} = -206.63\,\mathrm{kJ\,mol^{-1}} \tag{2.4}$$

while methanation of CO_2 (MCO2) is formally the reverse of GRR (*i.e.* MCO2 = revGRR):

$$CO_2 + 4\,H_2 \rightleftharpoons CH_4 + 2\,H_2O \qquad \Delta H^0_{298K} = -165.47\,\mathrm{kJ\,mol^{-1}} \tag{2.5}$$

The MCO2 reaction could result from the previous conversion of CO_2 into CO with the reverse water gas shift (revWGS):

$$CO_2 + H_2 \rightleftharpoons CO + H_2O \qquad \Delta H^0_{298K} = 41.16\,\mathrm{kJ\,mol^{-1}} \tag{2.6}$$

followed by MCO. Also for methanation the real reaction path is still not fully established. It is still not clear whether gas-phase CO is an intermediate in MCO2 (thus the reaction sequence is revWGS+MCO) or a final product (thus the MCO2 reaction would be parallel to the revWGS+MCO sequence).

Today, methanation of COx-containing mixtures is performed industrially to eliminate carbon oxides impurities in hydrogen (low temperature methanation [19]) or to produce Substitute or Synthetic Natural Gas (SNG) [20, 21] using syngases rich in carbon oxides, like those arising from coal gasification. Ni–based catalysts supported on high-surface-area Al_2O_3 [21–23] are largely used for these applications. These catalysts have also been reported to be active for methanation of CO_2-rich carbon oxides mixtures as well as for pure CO_2 methanation [24]. In fact, Ni metal catalysts are active for both steam reforming and methanation, according to the "micro-reversibility principle" [25]. The difference in catalyst formulations is essentially associated with the different stability requirements, related to the very dissimilar reaction conditions. In fact, while endothermic steam reforming must be realized at very high temperature (1000÷1200 K) with large excess of steam, exothermic COx-methanation is performed at much lower temperature (450÷750 K) with hydrogen excess or nearly stoichiometric feeds.

The methanation of CO_2-rich gases or of pure CO_2 in the presence of hydrogen is still not realized industrially [26]. It can be of interest in the future, for the production of methane or methane-hydrogen blends from captured CO_2 as an element of "CO_2 Capture and Utilisation Technologies" (CCU) to reduce the emissions of greenhouse gases, with producing useful compounds.

In the context of our studies on hydrogen production and CO_2 methanation [27–29], the present work aims at testing industrial steam reforming catalysts, both without and with potassium, as well as a home-made methanation catalyst (HMMC), in both SMR and MCO2. The experimental results are interpreted through the support of a simulation model developed for the laboratory reactors employed. The model is 1D and pseudo-homogeneous and includes mass and energy local balances. For the local kinetics, the model proposed by Xu and Froment [8] is implemented, based on the assumption that the SMR, WGS and GRR reactions are reversible and can proceed simultaneously, thus implicitly including both the series and parallel kinetic network.

The purpose for developing a laboratory reactor model is to analyze in detail the behavior of the laboratory reactors. Indeed, from a review of the models developed in the literature for methanation reactors [30] and for SMR reactors [31–33], it emerges that pseudo-homogeneous models with isothermal temperature profiles are often employed for the simulation of laboratory reactors, with the purpose of identifying the correct kinetic model and/or the kinetic parameters of the selected kinetic model. On the other hand, more detailed heterogeneous models with thorough evaluation of 1D or 2D concentration and temperature profiles inside the individual catalyst particles, and in the solid and gas phase along the full-size reactor, are employed for industrial reactor design and deployment [30, 34–40]. In the present work, a model is proposed for a laboratory scale reactor, where the hypothesis of pseudo-homogeneous behavior is retained (due to the small size of the catalyst particles), but thermal effects along the reactor are analyzed in more detail by including the local energy balance. In this way, 1D temperatures profiles along the laboratory reactor are evaluated, and it is found that, under relevant experimental conditions, temperature profiles can easily deviate from uniformity, due to the high enthalpy change of the reaction. This is pointed out as a significant aspect to take into account when employing laboratory reactor models with the purpose of identifying kinetic models and/or parameters for MCO2 and/or SMR reactions. Another aspect which is discussed on the basis of the model, is related to the usefulness of experimental data obtained at thermodynamic equilibrium from laboratory reactors operating in MCO2 and SMR operating mode. These data are usually disregarded as not useful for setting up kinetic models. However, in the present work it is discussed that comparison between the calculated $\left(\prod_i p_i^{\nu_i}\right)_{WGS}$ at the reactor outlet and the thermodynamic equilibrium constant is a useful parameter in order to check whether the WGS reaction proceeds in the exit line from the reactor, which often takes place [41–43] and could affect also the experimental data collected under kinetic regime. In the present contribution, instead of attempting at minimizing the experimental level all the temperature-related effects described above, it is proposed to include all the temperature-related effects into the simulation model.

The present work must not be intended as primarily devoted to a kinetic study; nevertheless comparison between simulation results and catalytic experimental data is reported and discussed, and the model is used to identify three sets of kinetic parameters for the Xu and Froment kinetics, each of which matches well the experimental data obtained from the respective catalyst.

2.2 Experimental

2.2.1 Catalytic Materials

Commercial Katalco JM57-4Q and JM25-4Q quadrilobe SMR catalysts, both from Johnson Matthey, are used, after gentle grinding. According to the literature [17, 18, 44], the 57-4Q catalyst contains ∼13 wt% Ni over a calcium aluminate cement, probably with a Ca:Al ratio of about 1:5 [45]. The surface area is $29\,m^2\,g^{-1}$. The 25-4Q catalyst is a slightly alkalized version, doped with small amounts (1.8 wt%) of K_2O [17]. A "home-made methanation catalyst" (HMMC) is prepared and used as a reference, where Siralox 5/170 (5% SiO_2 and 95% Al_2O_3) is used as the support after calcination at 1073 K for 5 h. Nickel is then deposited through wet impregnation of an aqueous solution of $Ni(NO_3)_2 \cdot 6\,H_2O$ by achieving the desired Ni loading (26 wt% as $wt_{Ni} \cdot 100\ wt_{catalyst}$). The resulting powder is dried at 363 K for 5 h and calcined at 1073 K for 5 h. The composition of this catalyst is comparable both with those of pre-reforming catalysts [17, 46] and of commercial COx methanation catalyst. The resulting catalyst has a surface area of $80\,m^2\,g^{-1}$, and the XRD analysis shows the feature of a nearly cubic spinel of NiO. Extensive characterization data on this catalytic material have been reported previously [47].

2.2.2 Laboratory Reactors

The MCO2 and the SMR experiments are performed in two different laboratory scale fixed-bed catalytic tubular reactors [48], respectively. The geometry is the same in both cases (Figure 2.1), while the dimensions of the two reactors are different (main data in Table 2.1).

TABLE 2.1: Dimensions of the components of the tubular laboratory reactors used in MCO2 and SMR experiments.

Dimensions $[10^{-3}m]$	**MCO2 reactor**	**SMR reactor**
H length	5	5
PBR length	26	12
P-R1 length	150	50
P-R2 length	300	40
d	6	6
s	1	1

In the MCO2 experimental reactor, the reactor tube is in silica glass. The catalytic packed bed (indicated as PBR, packed bed reactor, in Figure 2.1) is 26 mm long, and is formed by 88.2 mg of Ni-based catalyst, crunched in particles of about 0.2 mm size, and dispersed with 700 mg of silica glass particles of 0.21–0.25 mm size (corresponding to 60÷70 mesh sieved). The catalytic bed is kept in position by two holders made of quartz wool (H), about 5 mm long. Downstream, the gaseous reactants flow through the empty silica glass tube. This section is denominated post-reactor 1 (P-R1), and it is about 150 mm long. The silica glass tube, containing the PBR, is placed inside a tubular electric furnace with controlled temperature. At the exit of P-R1, the silica glass tube is connected to an empty stainless steel pipe (AISI 316L, typical composition code 18/8/3, indicating 18 wt% Cr, 8 wt% Ni and 3 wt% Mo), denominated post-reactor 2 (P-R2). The P-R2, 300 mm long, is directly exposed to the ambient temperature. At the exit of P-R2 the gaseous mixture is sampled for analysis.

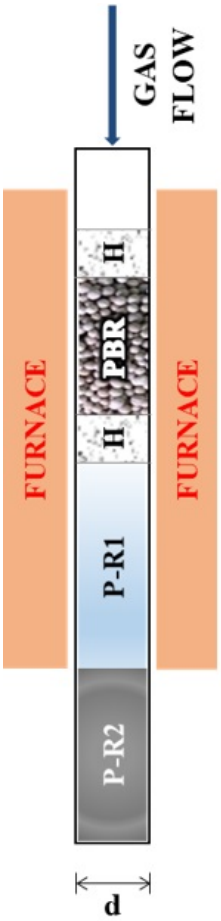

FIGURE 2.1: Schematic representation of the tubular laboratory reactor. PBR stands for packed bed reactor, P-R1 and P-R2 indicate the post reactor sections, H are the holders of the catalytic section, and d is the tube diameter. The same reactor geometry is employed for the MCO2 and SMR experiments, with different component dimensions (in Table 2.1).

The SMR experimental reactor has similar configuration, and is based on a silica glass tube containing a catalytic bed (PBR) consisting of 88.2 mg of Ni-based catalyst, crushed in particles of about 0.2 mm size, and dispersed with 440 mg of silica glass particles of 0.21÷0.25 mm size. Here, the PBR is 12 mm long and, again, it is kept in position by two holders made of quartz wool (H), about 5 mm long. Downstream, the empty silica glass tube (P-R1) is 50 mm long. The silica glass tube, containing the PBR, is placed inside a tubular furnace with controlled temperature. P-R2 is present again (AISI 316L), 40 mm long, where temperature is maintained at approximately 523 K using a heating ribbon. At the exit of P-R2, the gaseous mixture is sampled for analysis.

For all the tubes employed and described above, the internal diameter d is 6 mm and the tube wall thickness s is 1 mm.

2.2.3 Catalytic Experiments

All catalytic experiments are performed in steady state conditions. The MCO2 experiments are performed with feed gas composition: 6.1% CO_2, 29.8% H_2, N_2 balance, with 81.6 mL min^{-1} total flow rate (at RTP, reference temperature and pressure

of 273.15 K and 101.325 kPa respectively), corresponding to 6.7×10^3 h^{-1} GHSV calculated (at RTP) on the basis of the volume of the catalytic section (PBR) of the reactor. In order to follow any hysteresis, activation or deactivation effects, CO_2 hydrogenation experiments are performed both in ascending and descending reaction temperature steps (523 K, 573 K, 623 K, 673 K, 723 K, 773 K and reverse). Online products analysis is performed using a Nicolet 6700 FT-IR instrument. Frequencies where CO_2, CH_4 and CO molecules absorb weakly are used (2293 cm^{-1} for CO_2, 2170 cm^{-1} for CO, 1333 cm^{-1} for CH_4, after subtraction of baseline water absorption) with previous calibration using gas mixtures with known concentrations, in order to have quantitative results. Produced water is condensed before the IR cell. CO_2 conversion X_{CO_2}, selectivities S_i and yields to products Y_i, are calculated for CO and CH_4 on the basis of the measured inlet and outlet total flows (which allow to take into account the mole number variation during the reaction) and concentrations (calculated from the absorbances of CO, CO_2, CH_4). Definitions are [49]:

$$X_{CO_2} = \frac{F_{CO_2,in} - F_{CO_2,out}}{F_{CO_2,in}} \tag{2.7}$$

$$S_i = \frac{F_i}{F_{CO_2,in} - F_{CO_2,out}} \tag{2.8}$$

$$Y_i = \frac{F_i}{F_{CO_2,in}} \tag{2.9}$$

For the SMR experiments, the feed gas composition is: 5% CH_4, 20% H_2O, He balance. Two total flow rates are experimented: 120 mL min^{-1} (at RTP), corresponding to GHSV = 2.1×10^4 h^{-1} (at RTP) calculated on the basis of the volume of the catalytic section (PBR) of the reactor, and 80 mL min^{-1} (at RTP) corresponding to GHSV = 1.4×10^4 h^{-1} (at RTP). Product analysis is performed with a gas-chromatograph Agilent 4890 equipped with a Varian capillary column "Molsieve 5A/Porabond Q Tandem" and TCD and FID detectors in series. Between them, a nickel catalyst tube is employed to reduce COx to CH_4. Products analysis is also performed on GC/MS (FOCUS and ISQ from Thermo-Fisher), in order to have a precise identification of the compounds. Methane conversion is defined as follows [49]:

$$X_{CH_4} = \frac{F_{CH_4,in} - F_{CH_4,out}}{F_{CH_4,in}} \tag{2.10}$$

where F_i denotes molar flow rate. Selectivity to product i is defined as:

$$S_i = \frac{F_i}{\nu_i \left(F_{CH_4,in} - F_{CH_4,out}\right)} \tag{2.11}$$

where ν_i is the stoichiometric reaction coefficient of product i in reaction 2.3. The hydrogen yield, calculated on the basis of the GRR stoichiometry, is defined as:

$$Y_{H_2} = \frac{F_{H_2,out}}{4F_{CH_4,in}} \tag{2.12}$$

2.3 Modeling

Each laboratory reactor is simulated as a sequence of three tubular reactors: the PBR, P-R1 and P-R2. The holders (H) are not simulated. The models developed for

the three tubular sections are reported and discussed below.

2.3.1 PBR Model

A PBR is an extremely complex random geometrical arrangement. PBR models have been developed with different degrees of detail, depending on the desired accuracy, the available information on the packed bed and the required computational efforts. Systematic reviews are given by Lemcoff *et al.* [50], and by Koning [51]. Among models, the pseudo-homogeneous ones have obtained widespread acceptance, due to their convenient mathematical form. In particular, when dealing with the simulation of steady-state reactor at conditions not too close to run-away, the one-dimensional pseudo-homogeneous plug-flow model is generally considered adequate [52], and it is adopted in the present work. The fixed-bed catalytic reactor is simulated as one-dimensional along the reactor axis, and as a pseudo-continuum, where both fluid and solid phases are modeled as inter-penetrating continua, *i.e.*, as if they coexist at every point in the tube. The essential feature differentiating pseudo-homogeneous from heterogeneous models [53] is that the previous models do not include a detailed simulation of mass and energy transport inside the catalytic particle (internal transport limitations) and in the boundary layer around the catalytic particles (external transport limitations). In other words, temperature and concentration profiles in the catalytic particles are assumed to be uniform, with values identical to those in the bulk of the reacting fluid, which is consistent with the assumption of an effectiveness factor η equal to 1. Conversely, internal and/or external transport limitations are accounted for in heterogeneous models.

Per se, the use of small size laboratory reactors does not guarantee that the effectiveness factors are unity [54]. Instead, intraparticle transport limitations are primarily influenced by the catalyst particle size, while external transport limitations are primarily influenced by the fluid flow velocity. In the present work, due to the small size of the catalyst particles employed in the experiments, the generalized Thiele modulus [52] is < 1, and thus intraporous mass and energy transport resistances are neglected [52], *i.e.* the effectiveness factor η is assumed equal to 1 for all the reactions involved, as already reported for similar catalysts and reacting systems [8, 55–57]. External transport limitations are neglected as well [57].

The model is based on local steady-state mass and energy balances coupled to a local kinetics model.

2.3.1.1 Local balance equations

Based on the evaluation of the axial mass and heat *Pe* numbers (Section 2.3.1.3 – Evaluation of *Pe*), axial dispersion is neglected. The mass balance reads as follows [48]:

$$\frac{dF_i}{dV} = r_i = \sum_j \nu_{ij} r_j \tag{2.13}$$

where V is the reactor volume, and r_j is the kinetics of the j-th reaction. In the energy balance, the temperatures of gas and solid are assumed to be the same, and effective heat transport properties lump all the many heat-transfer processes occurring in

the individual phases. The energy balance includes the convective term of gas temperature variation along the reactor axial coordinate, the enthalpy variation of the reactions, and the heat transfer between the furnace and the PBR [48]:

$$\sum_j F_i \, c_{Pi} \, \frac{dT}{dV} = \sum_j \left(-\Delta H_j\right) \, r_j + U \, a \, \left(T_{furnace} - T\right) \tag{2.14}$$

where c_{Pi} is the specific heat of the i-th component, T is temperature, $T_{furnace}$ is the furnace temperature, ΔH_j is the enthalpy variation of reaction j, U is the global heat transfer coefficient, and a is the ratio between tube external surface S and volume:

$$a = \frac{S}{V} = \frac{\pi \, d \, L}{\pi \, \frac{d^2}{4} \, L} = \frac{4}{d} \tag{2.15}$$

The mass and energy balances form a system of coupled ordinary differential equations (ODEs). Boundary conditions are composition, temperature and flow rate of the gaseous mixture at the PBR inlet. The temperature of the gaseous mixture at the reactor inlet is assumed to be equal to the furnace temperature.

2.3.1.2 Heat transport properties

The local energy balance (Eq. 2.14) is a one-dimensional model of axial temperature profile including radial heat transfer, calculated on the basis of a single overall heat transfer coefficient U. Previous works [58, 59] adopting a similar approach, have pointed out that U must be calculated considering all the radial heat transfer phenomena, which, in our case, consist of three mechanisms in series: (i) convection inside the tube, (ii) conduction in the reactor wall, and (iii) radiation between the furnace and the reactor tube. Radiation is considered as ideal, *i.e.* the external tube wall temperature is assumed identical to the furnace temperature. Thus, only the heat transfer phenomena (i) and (ii) are considered, and their resistances are lumped in one single parameter, *i.e.* the overall heat transfer coefficient U, which is defined as [60]:

$$U = \left(\frac{1}{h} + \frac{s}{k_w}\right)^{-1} \tag{2.16}$$

where h is the convective heat exchange coefficient inside the tube, k_w is the thermal conductivity of the tube wall, and s is its thickness. In turn, the convective heat exchange coefficient h depends on the fluid (gas) chemical-physical and transport properties, and also on the flow pattern (*i.e.* laminar or turbulent). The Nusselt (Nu), Reynolds (Re), and Prandtl (Pr) dimensionless numbers are defined as follows [61, 62]:

$$Re = \frac{\rho_f \, u_S \, L}{\mu_f} \tag{2.17}$$

$$Pr = \frac{c_{Pf} \, \mu_f}{k_r} \tag{2.18}$$

$$Nu = \frac{h \, L}{k_r} \tag{2.19}$$

where ρ_f is the gas density, u_S is the superficial velocity, μ_f is the dynamic viscosity, c_{Pf} is the gas specific heat, k_r is the effective radial thermal conductivity of the packed bed, and h is the convective heat exchange coefficient. L is a characteristic dimension, which, in PBRs, is the catalyst particles diameter. The effective radial thermal conductivity k_r is evaluated considering heat conduction within the fluid, between the fluid and the solid catalyst particles, and among the solid particles. The literature correlation proposed by Zehner and Schlünder [63, 64] is adopted:

$$k_r = k_f \left\{ \left(1 - \sqrt{1-\varepsilon}\right) + \frac{2\sqrt{1-\varepsilon}}{1 - B\,\kappa^{-1}} \left[\frac{B\left(1-\kappa^{-1}\right)}{\left(1 - B\,\kappa^{-1}\right)^2} \ln\frac{\kappa}{B} - \frac{B-1}{1-B\,\kappa^{-1}} - \frac{B-1}{2} \right] \right\} \tag{2.20}$$

where k_f is the fluid (gas) thermal conductivity, ε is the bed void degree (assumed as 0.4 [65]), κ is the ratio between solid and gas thermal conductivities (k_s/k_f), and B is a parameter defined, for a bed of spheres, as follows:

$$B = 1.25 \left(\frac{1-\varepsilon}{\varepsilon}\right)^{1.11} \tag{2.21}$$

The thermal conductivity of the gaseous mixture k_f is calculated as the molar weighted average of the single components thermal conductivities [63]. Since the packed bed is formed by crunched catalyst highly dispersed in silica glass (Section 2.2.2 – Laboratory reactors), the solid thermal conductivity k_s is approximated to the value of the silica glass thermal conductivity. Also the tube wall is in silica glass, and thus $k_w = k_s$ = 1.6 W m^{-1} K^{-1} (from [66]).

Several correlations are proposed in the literature to evaluate Nu as a function of Re and Pr [67–74]. In the present work, the correlation proposed by Singhal *et al.* [74] is adopted:

$$Nu = 2.67 + 0.53\, Re^{0.77}\, Pr^{0.53} \tag{2.22}$$

Singhal *et al.* [74] developed Eq. 2.22 fitting the results of numerical simulations of heat transfer in packed beds of spherical particles. Eq. 2.22 does not include any void fraction dependency since there is a little variability in the void fraction of realistic packings of monodisperse spheres [75]. Furthermore, the limiting behavior for $Re \to 0$ is demonstrated to be physically sound [75].

2.3.1.3 Evaluation of *Pe*

The calculation of the axial massic Péclet number $Pe_{m,ax}$ is based on the evaluation of the expression [49]:

$$Pe_{m,ax} = \frac{u_S\, l}{\varepsilon\, \mathcal{D}_{ax}} \tag{2.23}$$

where l is the PBR length, and $\mathcal{D}_{ax}$ is the axial mass diffusivity. Since the evaluation of $\mathcal{D}_{ax}$ is not straightforwardly related to molecular diffusivity, and only a limited number of experimental investigations are reported in the literature [75], Gunn [76] developed a simple correlation between $Pe_{m,ax}$ and Pe_{mol}, where Pe_{mol} is the Pe number evaluated from Eq. 2.23 in which $\mathcal{D}_{ax}$ is substituted with the molecular diffusivity

$\mathcal{D}_{mol}$. The axial massic Péclet number is obtained from [77]:

$$Pe_{m,ax} = \left(\frac{1}{\tau}\frac{1}{Pe_{mol}} + \frac{1}{2}\right)^{-1} \tag{2.24}$$

where the tortuosity τ is determined using the theoretical model of Lanfrey *et al.* [77]:

$$\tau = \frac{\varepsilon}{(1-\varepsilon)^{\frac{4}{3}}} \tag{2.25}$$

The evaluation of $Pe_{m,ax}$ for the reactors under consideration in the present work gives $Pe_{m,ax} \approx 2$. According to [52, 78, 79], this value indicates that a regime where convective mass transport is dominating over axial dispersion is established, which justifies the assumption of neglecting the axial dispersion term in the mass balances (Eq. 2.13).

The calculation of the axial thermal Péclet number $Pe_{th,ax}$ is based on the evaluation of [63]:

$$Pe_{th,ax} = Re_{ax} \cdot Pr_{ax} \tag{2.26}$$

where Re_{ax} and Pr_{ax} are the Reynolds and Prandtl numbers evaluated in the axial direction (Eq. 2.17 and Eq. 2.18, where the characteristic length L is the tube diameter d, and the thermal conductivity is the axial one k_{ax}). Several studies are proposed in the scientific literature for the evaluation of k_{ax} [80–83]. In the present work, the literature correlation proposed by Votruba *et al.* [83] is adopted:

$$k_{ax} = k_f \, \kappa^{[0.28 - 0.757 \log\varepsilon - 0.057 \log\kappa]} \tag{2.27}$$

For the reactors under consideration in the present work, $Pe_{th,ax}$ ranges between 2 and 40 depending on the operating conditions. According to [51], this value indicates that a regime where convective energy transport is dominating over axial dispersion is established, and justifies the assumption of neglecting the axial dispersion term in the energy balance (Eq. 2.14).

2.3.1.4 Ni-based catalyst kinetics

The reaction scheme proposed by Xu and Froment [8] is adopted, based on the reaction rates of the SMR, WGS and GRR reactions. Reaction rates are reversible and of Langmuir-Hinshelwood type:

$$r_{SMR} = \frac{k_{SMR}}{p_{H_2}^{2.5}} \frac{p_{CH_4}\, p_{H_2O} - \frac{p_{CO}\, p_{H_2}^3}{K_{p,SMR}}}{DEN^2} \tag{2.28}$$

$$r_{WGS} = \frac{k_{WGS}}{p_{H_2}} \frac{p_{CO}\, p_{H_2O} - \frac{p_{CO_2}\, p_{H_2}}{K_{p,WGS}}}{DEN^2} \tag{2.29}$$

$$r_{GRR} = \frac{k_{GRR}}{p_{H_2}^{3.5}} \frac{p_{CH_4}\, p_{H_2O}^2 - \frac{p_{CO_2}\, p_{H_2}^4}{K_{p,GRR}}}{DEN^2} \tag{2.30}$$

$$DEN = 1 + K_{CO}\, p_{CO} + K_{H_2}\, p_{H_2} + K_{CH_4}\, p_{CH_4} + K_{H_2O}\, \frac{p_{H_2O}}{p_{H_2}} \tag{2.31}$$

with the kinetic parameters k_j and adsorption parameters K_i are expressed as reported below:

$$k_j = k_{j,T_r} \exp\left[-\frac{E_j}{R}\left(\frac{1}{T} - \frac{1}{T_r}\right)\right] \qquad j = SMR, WGS, GRR \tag{2.32}$$

$$K_i = K_{i,T_r} \exp\left[-\frac{\Delta H_i}{R}\left(\frac{1}{T} - \frac{1}{T_r}\right)\right] \qquad i = CO, H_2, CH_4, H_2O \tag{2.33}$$

where T_r is a reference temperature whose value is reported in Table 2.2, together with the values of the other parameters appearing in Eq. 2.32 and Eq. 2.33.

TABLE 2.2: Kinetic parameters, from Xu and Froment [8].

Parameter	Value	Units	Notes
k_{SMR,T_r}	1.842×10^{-4}	$\mathrm{kmol\,bar^{0.5}\,kg_{cat}^{-1}\,h^{-1}}$	$T_r = 648\,\mathrm{K}$
k_{WGS,T_r}	7.558	$\mathrm{kmol\,bar^{-1}\,kg_{cat}^{-1}\,h^{-1}}$	$T_r = 648\,\mathrm{K}$
k_{GRR,T_r}	2.193×10^{-5}	$\mathrm{kmol\,bar^{0.5}\,kg_{cat}^{-1}\,h^{-1}}$	$T_r = 648\,\mathrm{K}$
E_{SMR}	240.1	$\mathrm{kJ\,mol^{-1}}$	
E_{WGS}	67.13	$\mathrm{kJ\,mol^{-1}}$	
E_{GRR}	243.9	$\mathrm{kJ\,mol^{-1}}$	
K_{CH_4,T_r}	0.1791	$\mathrm{bar^{-1}}$	$T_r = 823\,\mathrm{K}$
K_{CO,T_r}	40.91	$\mathrm{bar^{-1}}$	$T_r = 648\,\mathrm{K}$
K_{H_2,T_r}	0.029 60	$\mathrm{bar^{-1}}$	$T_r = 648\,\mathrm{K}$
K_{H_2O,T_r}	0.4152	–	$T_r = 823\,\mathrm{K}$
ΔH_{CH_4}	−38.28	$\mathrm{kJ\,mol^{-1}}$	
ΔH_{CO}	−70.65	$\mathrm{kJ\,mol^{-1}}$	
ΔH_{H_2}	−82.90	$\mathrm{kJ\,mol^{-1}}$	
ΔH_{H_2O}	88.68	$\mathrm{kJ\,mol^{-1}}$	

2.3.2 P-R1 and P-R2 Model

The exit line from the reactor is simulated as well. In this case, the empty pipes P-R1 and P-R2 are simulated by applying a steady-state, non-isothermal plug flow reactor (PFR) approach, consisting in practice of the same local mass (Eq. 2.13) and energy (Eq. 2.14) balances employed for the PBR simulation. The global heat transfer coefficient U is evaluated also in P-R1 and P-R2, using the same definition employed for the PBR reactor (Eq. 2.16). For Re, Pr, and Nu, the definitions given in Eq. 2.17 ÷ Eq. 2.19 apply, with L being the tube hydraulic diameter. The evaluation of h is based on the evaluation of Nu. For an empty tube, with constant wall temperature and with laminar fluid flow regime as in the present case, Nu is constant, equal to 3.66 [60]. The effective thermal conductivity coincides with the thermal conductivity of the gaseous mixture k_f [62].

The mass and energy balances of P-R1 and P-R2 form a system of coupled differential equations (ODEs). Boundary conditions are the inlet composition, temperature and flowrate of the gaseous mixture, which coincide with those at the exit of the previous reactor section.

2.3.2.1 Gas phase WGS kinetics

Downstream the catalytic bed, the reacting mixture flows through the post-reactor P-R1. Here, according to the literature [42, 43], the quartz wool and the silica glass tube are not expected to catalyze the reactions. However, WGS is expected to occur in gas phase, and the following kinetics is adopted [41, 43]:

$$r_{WGS} = k'_{WGS} \sqrt{C_{CO}}\, C_{H_2O} \left(1 - \frac{p_{H_2}\, p_{CO_2}}{p_{CO}\, p_{H_2O}\, K_{p,WGS}}\right) \tag{2.34}$$

where:

$$k'_{WGS} = k'_{WGS,0} \exp\left(-\frac{E'_{WGS}}{R\,T}\right) \tag{2.35}$$

with $k'_{WGS,0} = 7.4 \times 10^{11}$ $\mathrm{cm^{1.5}\,mol^{0.5}\,s^{-1}}$ and $E'_{WGS} = 288.3\,\mathrm{kJ\,mol^{-1}}$ [41, 43].

2.3.2.2 Metal tube WGS kinetics

Downstream P-R1, the gaseous mixture flows through the metallic post-reactor P-R2. It is widely reported in the literature that the WGS reaction is catalyzed by metallic piping [41]. For the WGS kinetic expressions, it is proposed here to apply the WGS kinetic equation proposed by Xu and Froment (Eq. 2.29), with $k_{WGS,T_r} = 4.7\,\mathrm{kmol\,bar^{-1}\,m^{-2}\,h^{-1}}$, referred to the unit area of inner surface of the tube.

An alternative option follows the approach proposed by Bustamante *et al.* [42, 43] who have reported a very fast reaction rate measured with Inconel® 600 piping (typical composition 14-17 wt% Cr, 72 wt% Ni, 6-10 wt% Fe, 1 wt% Mn, 0.5 wt% Cu, 0.5 wt% Si, 0.15 wt% C and 0.015 wt% S), for which they have assumed the following kinetic expression [84]:

$$r_{WGS} = k''_{WGS}\, C_{CO} \left(1 - \frac{p_{H_2}\, p_{CO_2}}{p_{CO}\, p_{H_2O}\, K_{p,WGS}}\right) \tag{2.36}$$

where:

$$k''_{WGS} = k''_{WGS,0} \exp\left(-\frac{E''_{WGS}}{R\,T}\right) \tag{2.37}$$

with $k'_{WGS,0} = 4.26 \times 10^{6}\ \mathrm{cm^2\,s^{-1}}$ and $E''_{WGS} = 102.4\,\mathrm{kJ\,mol^{-1}}$ [41, 43].

2.3.3 Thermodynamic Equilibrium

For both the WGS and the SMR reactions, $K_{p,WGS}$ and $K_{p,SMR}$ are obtained through the equation below [85]:

$$K_p = A \exp\left(-\frac{E_K}{R\,T}\right) \tag{2.38}$$

The values of parameters A and E_K are reported in Table 2.3. Eq. 2.38 provides a fit of the data of K_p given in [12].

For GRR:

$$K_{p,GRR} = K_{p,SMR} \cdot K_{p,WGS} \tag{2.39}$$

TABLE 2.3: Parameters for the calculation of Kp through Eq. 2.38 [85].

Parameter	WGS	SMR
A	1.412×10^{-2}	7.846×10^{12}
E_K	220.2	-37.72

2.3.4 Numerical Integration

The model equations form an ordinary differential and algebraic equation (DAE) system, which is integrated through MATLAB® R2018a. The system of coupled ODEs (local mass and energy balances) is solved through the `ode45` solver. Input data of the numerical tool are the reactor geometrical data, flow rate and composition of the reacting gas mixture, and the furnace temperature. The reactor simulation, for one single operating condition, typically runs in less than 1 second on a workstation Dell Precision Tower 3420, with Intel Xeon CPU running at 3.60 GHz with 64 GB of RAM. The parameters of the local kinetics model are evaluated taking as a reference the values proposed by Xu and Froment [8] and reported in Table 2.2. Here, they are adjusted through the multiplicative coefficients ζ_1 to ζ_6 until a satisfactory agreement with the experimental data is found. The procedure adopted to perform the adjustment is a trial-and-error procedure. Table 2.4 reports the values of all the adjusting coefficients for the kinetic parameters employed in the simulations. Regarding the activation energies of the SMR and WGS reactions, the adjusting coefficients ζ_4 and ζ_5 proposed in the present work are similar to those published in [56], where values corresponding to $\zeta_4 = 1.07$ and $\zeta_5 = 1.33$ are reported. In the same work, the activation energy of the GRR reaction is multiplied by a factor 0.97, while in our case the multiplying coefficient is 1. The catalyst employed in [56] is a 18 wt% NiO supported on $\alpha - Al_2O_3$ provided by Johnson Matthey Plc, tested for SMR and GRR at temperatures around 600 °C, for WGS around 300 °C.

Table 2.5 reports the values of the main chemical-physical parameters and dimensionless numbers in the operating conditions adopted in the present study. The relative error between simulation results and experimental data is reported in Section 2.4 – Modeling results and comparison with experimental data.

TABLE 2.4: Values of the adjusting coefficients $\zeta_1 \div \zeta_6$ adopted to adapt the Xu and Froment kinetic model (Table 2.2) to the catalysts investigated in the present work.

		HMMC	JM57-4Q	JM25-4Q
$\zeta_1 \cdot k_{SMR}$	ζ_1	15	25	8
$\zeta_2 \cdot k_{WGS}$	ζ_2	15	100	130
$\zeta_3 \cdot k_{GRR}$	ζ_3	15	10	10
$\zeta_4 \cdot E_{SMR}$	ζ_4	1	1.17	1.22
$\zeta_5 \cdot E_{WGS}$	ζ_5	1	1.5	1.7
$\zeta_6 \cdot E_{GRR}$	ζ_6	1	90	96

TABLE 2.5: Values of the main chemical-physical parameters and dimensionless numbers in the operating conditions adopted in the present study. The values reported are evaluated at the reactor inlet, at temperature equal to the oven temperature.

Variable	MCO2		SMR		Units
	$T = 473\,\mathrm{K}$	$T = 773\,\mathrm{K}$	$T = 773\,\mathrm{K}$	$T = 1173\,\mathrm{K}$	
$GHSV@RTP$	6.7×10^3		2.4×10^4		h^{-1}
u_S	0.0822	0.133	0.200	0.459	$\mathrm{m\,s}^{-1}$
μ	2.03×10^{-5}	2.85×10^{-5}	3.56×10^{-5}	6.49×10^{-5}	$\mathrm{kg\,m}^{-1}\,\mathrm{s}^{-1}$
c_P	5.06	5.16	4.52	4.71	$\mathrm{kJ\,kg}^{-1}\,\mathrm{K}^{-1}$
ρ	0.305	0.187	4.74×10^{-2}	2.06×10^{-2}	$\mathrm{kg\,m}^{-3}$
k_f	9.89×10^{-2}	1.42×10^{-1}	2.42×10^{-1}	0.464	$\mathrm{W\,m}^{-1}\,\mathrm{K}^{-1}$
k_s	1.57	1.99	1.99	3.39	$\mathrm{W\,m}^{-1}\,\mathrm{K}^{-1}$
k_{ax}	0.945	1.25	1.46	2.57	$\mathrm{W\,m}^{-1}\,\mathrm{K}^{-1}$
$Re = \frac{\rho\, u_S\, d}{\mu}$	7.36	5.243	1.600	0.878	–
$Pr = \frac{\mu c_p}{k_f}$	1.04	1.03	0.665	0.659	–
Nu	3.43	2.28	2.91	2.83	–
U	380	503	584	1019	$\mathrm{W\,m}^{-3}\,\mathrm{K}^{-1}$

2.4 Modeling Results and Comparison with Experimental Data

2.4.1 HMMC Catalyst

Figure 2.2 reports the results obtained from the HMMC catalyst. Model results are displayed together with experimental data, both evaluated at the sampling point (exit of P-R2). The simulations are carried out using the same set of kinetic parameters originally proposed by Xu and Froment [8] for a Ni catalyst supported on Mg spinel ($Ni/MgAl_2O_4$); the only difference is that all the pre-exponential factors (k_{SMR}, k_{WGS} and k_{GRR}) here are multiplied for the same coefficient equal to 15 (Table 2.4). This is justified by considering the higher Ni loading of the HMMC catalyst compared to the Xu and Froment catalyst (26 wt% vs. 15.2 wt% respectively), and the higher BET-surface area ($80\,\mathrm{m^2\,g^{-1}}$ vs. $58\,\mathrm{m^2\,g^{-1}}$). Finally, Xu and Froment [8] have developed their kinetic model based on experimental data obtained from a partially deactivated catalyst, and recommend to multiply the kinetic parameters for a factor 2.246 when a fresh catalyst is used, such as in the present case.

In Figure 2.2, panels a-f display the results obtained in MCO2 mode, with the furnace temperature varying in the range $523 \div 773\,\mathrm{K}$. In particular, panel f (red line) displays the maximum temperature in the catalytic section (PBR) of the reactor, evaluated through the simulation model. Indeed, in the catalytic section of the reactor (PBR), the exothermal revSMR reaction causes an increase of reactor temperature above that of the furnace, resulting in a mild maximum in the temperature profile, which is noticeable for a furnace temperature above 610 K. This difference of reacting gas temperature from the furnace temperature does not exceed 40 K for all the operating conditions considered here, and, in all cases, the simulated reactor temperature is equal to the furnace temperature at the exit of the PBR and in the subsequent PR1, while a rapid quench occurs in P-R2. Temperature and composition profiles along the reactor will be discussed further in the subsequent 2.4.4 – MCO2 laboratory reactor, but it is anticipated here that the gas composition does not change along P-R1 nor along P-R2.

Corresponding to panel f, panels d and e report the thermodynamic equilibrium constant K_p calculated at the furnace temperature, together with the $\left(\prod_i p_i^{\nu_i}\right)$ calculated on the basis of the model results at the sampling point, respectively for the revWGS and revSMR reactions. As already mentioned, gas compositions do not change in P-R1 and P-R2, and thus panels d and e demonstrate that both the revWGS and revSMR reactions are at thermodynamic equilibrium at the exit of PBR for furnace temperatures equal to or larger than $T = 673\,\text{K}$. Conversely, kinetic regime holds for $T < 673\,\text{K}$. The corresponding gas compositions, measured and simulated at the sampling point, are reported in panels a-c. In particular, panels a,b display that, by increasing temperature, reactant (CO_2, H_2) consumption and product (CH_4, H_2O) generation increase as long as temperature remains in the kinetic regime window. The maximum value of CH_4 and H_2O molar fractions (5.9% and 11.8% respectively), and the corresponding minimum of CO_2 and H_2 (0.85% and 9.8%) are obtained around 673 K. Increasing temperature further, the thermodynamic regime holds. Here, by increasing temperature, the main effect is the marked decrease of the K_p of the exothermal revSMR reaction, as displayed by Figure 2.2 e); the simultaneous increase of the mildly endothermal revWGS (Figure 2.2 d) is less marked. Considering the overall revGRR reaction, its K_p is obtained through Eq. 2.39 and thus follows practically the same behavior of the K_p of revSMR reaction, *i.e.* it decreases strongly by increasing temperature. Thus, by increasing temperature, the revGRR is more and more shifted towards the reactants, and this explains the observed reduction of CH_4 and H_2O molar fractions and the associated increase of CO_2 and H_2 molar fractions displayed in panels a-b. In addition, panel c reports the behavior of CO, which, being produced by the revWGS and consumed by the revSMR, displays a trade-off behavior with a maximum at about 608 K, demonstrating that revWGS and revSMR kinetics prevail respectively below and above 608 K. Above 673 K, the already discussed dominating decrease of $K_{p,revSMR}$ by increasing temperature results in a continuous increase of CO.

Panels g-r report the results obtained in SMR mode, with two different GHSVs (1.4×10^4 h^{-1} and 2.1×10^4 h^{-1}), with furnace temperatures varying in the range $773 \div 1173$K. The analysis is started again with a discussion of temperature results in the reactor. More detailed results are reported in the subsequent Section 2.4.5 – SMR laboratory reactor, but here it is anticipated that a temperature drop occurs close to the entrance of the packed bed (PBR), due to the endothermal SMR reaction. After the temperature drop, temperature quickly raises and reaches the furnace temperature well before the exit of the PBR. Minimum temperatures are reported in panels l and r. With the HMMC catalyst, due to the high catalyst activity and the consequently fast reaction kinetics, the temperature drops are marked. Since axial heat conduction within the PBR is not considered in the model, this temperature drop may be somehow overestimated, at least for furnace temperatures above 880 K (dotted lines in panels l and r of Figure 2.2). However, the predicted temperature drop is very narrow. For example, for a GHSV = 2.1×10^4 h^{-1} and for a furnace temperature of 900 K, the minimum temperature of 765 K is reached at 0.03 mm after the entrance of the PBR, which is followed by a temperature increase up to 890 K at 1.1 mm after the entrance of the PBR. This temperature drop will be discussed further in Section 2.4.5 – SMR laboratory reactor. Furthermore, it will be discussed that no temperature nor composition changes occur in P-R1. Conversely, a temperature decrease occurs in P-R2, in a slower fashion than in MCO2 operating mode, mainly due to the higher external temperature (523 K in SMR vs. 298 K in MCO2). Simultaneously, the WGS reaction occurs in a slight, yet appreciable, way. This phenomenon of WGS occurring thermally, or catalyzed by the metallic piping, in the exit-line of experimental laboratory reactors, is

reported in the literature [41, 43, 84], and is included in the model presented in this work. More detailed results are reported in the subsequent Section 2.4.5 – SMR laboratory reactor. Nevertheless, here, these preliminary considerations allow to explain the results in panels j and p of Figure 2.2, which, on the one hand, display that the $K_{p,WGS}$ calculated at the furnace temperature coincides with the model calculations of $\left(\prod_i p_i^{\nu_i}\right)_{WGS}$ at the exit of the catalytic section, showing that the model predicts WGS to be at thermodynamic equilibrium at the exit of the PBR. On the other hand, in the same figures, modeling and experimental results of $\left(\prod_i p_i^{\nu_i}\right)_{WGS}$ at the sampling point (exit of P-R2) are slightly higher (but definitely lower than $K_{p,WGS} = 86.7$ calculated at the P-R2 external temperature of 523 K), demonstrating a further slight advancement of the WGS reaction in P-R2.

For the SMR reaction, the experimental and simulated $\left(\prod_i p_i^{\nu_i}\right)_{SMR}$ at the sampling point are reported in panels k and q, together with $K_{p,SMR}$ calculated at the furnace temperature. The three reported quantities coincide, demonstrating that the SMR reaction is at thermodynamic equilibrium at the exit of the reactor for all the operating conditions investigated. In particular, since no SMR reaction occurs in PR-1 and in PR-2, figures k and q demonstrate that SMR is at thermodynamic equilibrium at the exit of the packed bed (PBR), and also provide a confirmation that the experimental temperature at the outlet of PBR is equal to the furnace temperature. In figures k and q, no experimental values of $\left(\prod_i p_i^{\nu_i}\right)_{SMR}$ are reported for temperatures above 933 K and 1013 K respectively, because the amount of methane in the sampled gaseous mixture is below the resolution of the experimental measurement system, and thus it is evaluated as zero. Therefore, the experimental $\left(\prod_i p_i^{\nu_i}\right)_{SMR}$ diverges to infinity in these conditions.

The corresponding compositions measured and simulated at the sampling point, are reported in panels g-i for GHSV = 1.4×10^4 h^{-1}, and in panels m-o for GHSV = 2.1×10^4 h^{-1}. Being SMR endothermal, it is thermodynamically favored by increasing temperature, with a progressive increase in reactant (CH_4, H_2O) consumption and product (CO_2, H_2) generation. For furnace temperatures above 890 K, the SMR reaction is complete, with CH_4 being completely consumed inside the PBR zone of the SMR reactor. Then, the compositions obtained by increasing further the furnace temperature are dictated by WGS. Being WGS mildly exothermal, it gradually shifts towards the reactants by increasing temperature, and this explains the slight decrease of CO_2 and H_2 and the associated slight increase of CO and H_2O. The maximum hydrogen molar fraction obtained experimentally is 16.7% (at a furnace temperature of 893 K for GHSV = 1.4×10^4 h^{-1}, and at a furnace temperature of 933 K for GHSV = 2.1×10^4 h^{-1}).

In SMR conditions, differences between reactor behavior at GHSV = 1.4×10^4 h^{-1} and at GHSV = 2.1×10^4 h^{-1} are of minor entity, and in both cases the SMR reaction reaches thermodynamic equilibrium before the exit of the PBR, for all the operating conditions investigated. In all cases, under both MCO2 and SMR operating mode, the agreement between experimental and simulated results is very good. The average value of the absolute difference between measured and simulated outlet molar fractions is 1.7×10^{-3}, and the mean absolute percentage error is 8.6%. The discrepancy between experimental and simulated results reported in Figure 2.2, panels j, p, is related to the difficulty in simulating in a more accurate manner the advancement of the WGS in the exit line of the reactor.

Overall, the results offer a further confirmation for the validity of the kinetic model set up by Xu and Froment [8]. This kinetic model is typically applied to the simulation

of SMR reactors [6, 86–88]; however, since it is based on reversible reaction kinetics, it is expected to apply also to MCO2 reactors, and the results reported in panels a-e of Figure 2.2 provide a confirmation. It is interesting to notice that 773 K is the highest temperature experimented in MCO2 mode as well as the lowest temperature experimented in SMR mode; at this temperature, with the HMMC catalyst, the SMR reaction is at thermodynamic equilibrium at the exit of the PBR section of the experimental reactor, under both MCO2 and SMR operating conditions.

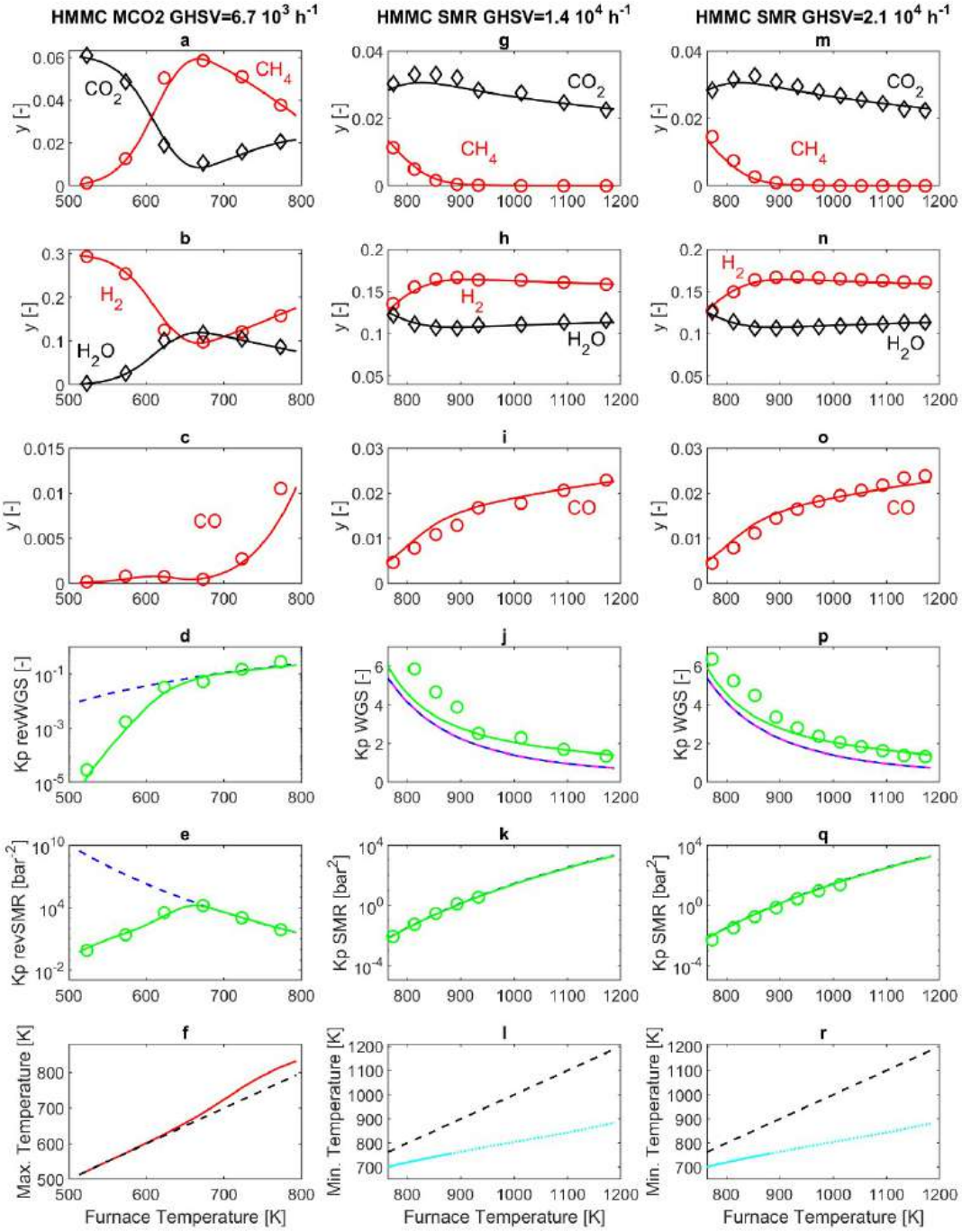

FIGURE 2.2: Results for the HMMC catalyst. Panels **a-f**: MCO2 operating mode (GHSV = 6.7×10^3 h^{-1}). Panels **g-l**: SMR operating mode (GHSV = 1.4×10^4 h^{-1}). Panels **m-r**: SMR operating mode (GHSV = 2.1×10^4 h^{-1}). Symbols: experimental data. Lines: simulations. Panels **a-c**, **g-i**, **m-o**: compositions at the sampling point (exit of P-R2). Panels **d, j, p**: $K_{p,WGS}$ calculated at the furnace temperature (Eq. 2.38); model calculation and experimental data of $\left(\prod_i p_i^{\nu_i}\right)_{WGS}$ at the sampling point (exit of P-R2). Panels **j, p**: model calculation of $\left(\prod_i p_i^{\nu_i}\right)_{WGS}$ at the exit of the PBR. Panels **e, k, q**: $K_{p,SMR}$ calculated at the furnace temperature (Eq. 2.38); model calculation and experimental data of $\left(\prod_i p_i^{\nu_i}\right)_{SMR}$ at the sampling point (exit of P-R2). Panels **f, l, r**: furnace temperature; model results of: maximum temperature in the PBR of the MCO2 reactor and , minimum temperature in the PBR of the SMR reactor.

2.4.2 JM57-4Q Catalyst

Figure 2.3 reports both modeling and experimental results obtained from the commercial JM57-4Q catalyst. The first remark when comparing the experimental results obtained in SMR and MCO2 operating modes, is that at the same temperature of 773 K an interesting difference appears. Indeed, in MCO2 mode, the SMR reaction is at thermodynamic equilibrium at the exit of the PBR (panel e), while this is clearly no more true in SMR operating mode (panels k and q). The possibility that this is related to thermal effects, *i.e.* the internal temperature of the PBR being higher than the furnace temperature in MCO2 operating mode, and lower than the furnace temperature in SMR operating mode, has been considered in the present work by performing the simulation of the reactor temperature profile. However, as already discussed and further deepened in Sections 2.4.4 and 2.4.5, the simulated PBR temperature shows a peak/drop close to the PBR entrance, followed by an almost flat profile, very close to the furnace temperature, in MCO2/SMR operating modes. The entity of the peak can change from one experiment to another, but ultimately it has rather small influence on the overall reaction rate and thus on the gas composition at the PBR exit. A more convincing explanation can be formulated considering that the literature reports that H_2O concentration strongly influences the SMR kinetics [89], and that the composition of the JM57-4Q and JM25-4Q catalysts improves water adsorption properties [18]. More in detail, both JM commercial catalysts are based on a calcium aluminate support, where the addition of calcium oxide component can result in the increase of water adsorption through neutralisation of the acidic sites present on alumina. Keeping in mind that the HMMC catalyst employs a calcium-free support, the different support composition may explain different water adsorption capabilities and ultimately the striking different behavior observed at 773 K.

It has been pointed out by several authors [89] that a change of catalyst composition or operating conditions (temperature and S/C ratio) may alter not only the values of the parameters in the kinetic model, but also the structure of the model itself. Nevertheless, the present work presents an attempt to apply the Xu and Froment [8] kinetic scheme, by adapting the model parameters to the different catalysts, and then keeping them unchanged for all the operating conditions investigated.

Assuming that the different behavior observed at 773 K under MCO2 and SMR operating mode is related to an increased water adsorption, the water adsorption coefficient K_{H_2O,T_r} for JM57-4Q is supposed to be 90 times that originally proposed by Xu and Froment [8] (see Table 2.4). All the other kinetic parameters adopted are reported in Table 2.4; in particular, the pre-exponential coefficients are increased over those originally proposed by Xu and Froment [8], as well as the activation energies. With this choice of the kinetics parameters, the simulation results reported in Figure 2.3 display a satisfactory agreement with the experimental data. The average value of the absolute difference between measured and simulated outlet molar fractions is 2.8×10^{-3}, corresponding to a mean absolute percentage error of 11.8%. The highest relative error is for the calculation of the CO molar fraction at the exit of the laboratory MCO2 reactor, since the experimentally measured molar fraction is very low (Figure 2.3 c). In addition, also the difficulty in capturing in an accurate manner the advancement of the WGS in the exit line of the reactor (Figure 2.3, panels j, p) impacts on the accuracy of the simulation results.

In MCO2 operating mode, focusing on the individual chemical species, slight differences are found in the molar fractions at the outlet of the reactor, compared to the results obtained with the previous HMMC catalyst. This is evidenced by panels a, b

and c of Figure 2.3, that display a slightly reduced H_2 and CO_2 consumption, associated to a slightly reduced CH_4 and H_2O production, compared to panels a, b and c of Figure 2.2. In SMR mode, the expected slowdown of the SMR reaction rate is visible especially in the panels g and m of Figure 2.3, reporting the CH4 molar fraction at the reactor outlet. Here, the CH_4 consumption is completed for a furnace temperature of about 930 K, and below that temperature the CH_4 molar fraction at the reactor outlet is visibly higher than that displayed in Figure 2.2, panels g and m, for the HMMC catalyst. Analogous considerations apply also to H_2O (panels h and n) while, for furnace temperatures below 930 K, H_2 (panels h, n) and CO_2 (panels g, m) are higher than in the in the corresponding panels in Figure 2.2. For a furnace temperature higher than about 930 K SMR thermodynamic equilibrium is established at the PBR outlet, and thus at higher temperatures the compositions follow practically the same trend already discussed for Figure 2.2.

Concerning the WGS reaction, in the Xu and Froment kinetics equations scheme [8] also the WGS kinetics is of Langmuir-Hinshelwood type, and thus it is slowed down for high K_{H_2O,T_r} values. This slowdown of the WGS reaction results in WGS thermodynamic equilibrium being not fully established at the exit of the PBR. This is displayed by the model results reported in panels j and p of Figure 2.3 (pink line non collapsing with the blue dotted line). As already found before, the model calculates a further advancement of the WGS reaction in the P-R2 post-reactor (green line), that is partially confirmed by the experimental data (green circles).

Concerning the simulated maximum and minimum temperatures inside the PBR, the qualitative behavior is similar to that previously discussed for the HMMC reactor. More in detail, in MCO2 mode, no significant differences are observed in panel f of Figure 2.3 and Figure 2.2. In SMR mode, instead, differences are noticeable, since the slow SMR reaction occurring on the JM57-4Q catalyst is accompanied by a small temperature drop at the entrance of the PBR, as displayed by panels l and r of Figure 2.3. For example, for a GHSV = 2.1×10^4 h^{-1} and for a furnace temperature of 900 K, the reactor temperature reaches the minimum value of 870 K at 0.012 mm after the entrance of the PBR (which, according to further simulations, is followed by a temperature increase up to 890 K at 2.7 mm after the entrance of the PBR).

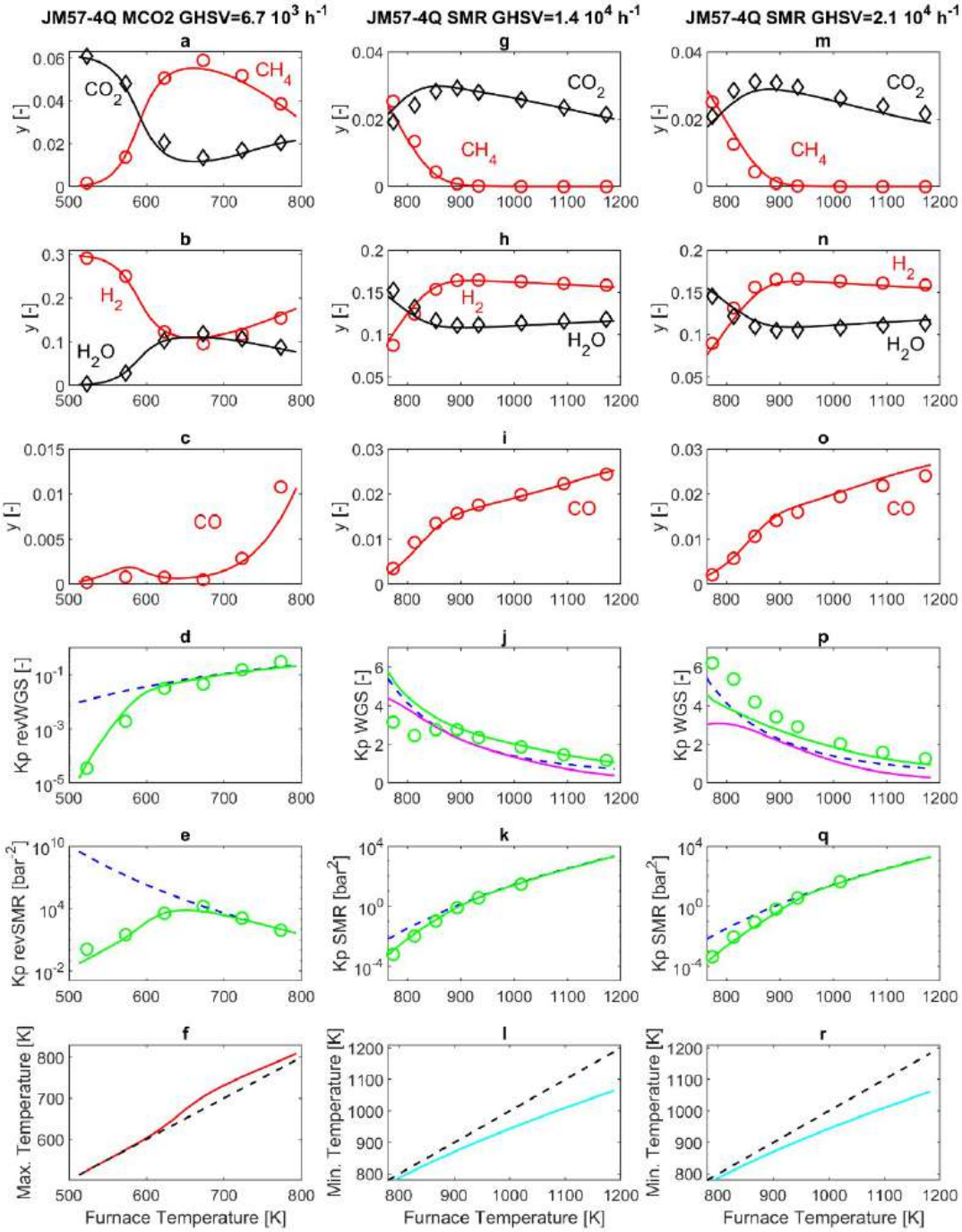

FIGURE 2.3: Results for the JM57-4Q catalyst. Panels **a-f**: MCO2 operating mode (GHSV = 6.7×10^3 h^{-1}). Panels **g-l**: SMR operating mode (GHSV = 1.4×10^4 h^{-1}). Panels **m-r**: SMR operating mode (GHSV = 2.1×10^4 h^{-1}). Symbols: experimental data. Lines: simulations. Panels **a-c**, **g-i**, **m-o**: compositions at the sampling point (exit of P-R2). Panels **d, j, p**: - - - $K_{p,WGS}$ calculated at the furnace temperature (Eq. 2.38); ——— model calculation and ○ experimental data of $\left(\prod_i p_i^{\nu_i}\right)_{WGS}$ at the sampling point (exit of P-R2). Panels **j, p**: ——— model calculation of $\left(\prod_i p_i^{\nu_i}\right)_{WGS}$ at the exit of the PBR. Panels **e, k, q**: - - - $K_{p,SMR}$ calculated at the furnace temperature (Eq. 2.38); ——— model calculation and ○ experimental data of $\left(\prod_i p_i^{\nu_i}\right)_{SMR}$ at the sampling point (exit of P-R2). Panels **f, l, r**: - - - furnace temperature; model results of: ——— maximum temperature in the PBR of the MCO2 reactor and ——— minimum temperature in the PBR of the SMR reactor.

2.4.3 JM25-4Q Catalyst

Figure 2.4 reports the results obtained from the commercial JM25-4Q catalyst, which employs not only a calcium aluminate support, but also a 1.8 wt% K_2O addition, whose role is to increase further the surface basicity and avoid coke deposition [18]. Indeed, it has been reported that, in SMR operating mode, since water adsorbs dissociatively on the catalyst surface, the increased number of sites for water adsorption increases the oxygen available on the surface, leading to an increase of the rate of carbon gasification and of the carbon monoxide production rate [18]. Thus, in modeling the performance of the JM25-4Q catalyst, the water adsorption parameter K_{H_2O,T_r} is further increased. In addition, the pre-exponential factor of the WGS reaction k_{WGS} is increased as well, as reported in Table 2.4. With this choice of the kinetics parameters, the average value of the absolute difference between measured and simulated outlet molar fractions is 2.6×10^{-3}, corresponding to a mean absolute percentage error of 9.7%. With the JM25-4Q catalyst, the increased water adsorption further slows the SMR and revSMR reaction rate, compared to the JM57-4Q catalyst. This is visible by comparing panels e, k, q in Figure 2.4 and in Figure 2.3. Figure 2.4, panel e, shows that, in MCO2 operating mode, thermodynamic equilibrium is now reached at the PBR outlet for a furnace temperature of 773 K. Correspondingly, the maximum of CH_4 molar fraction displayed panel a is now about 5%, visibly reduced compared to that reported in Figure 2.3, panel a. Analogously, panels k and q of Figure 2.4 show that, in SMR operating mode, thermodynamic equilibrium is reached for a furnace temperature of 1013 K, visibly increased compared to that displayed in Figure 2.3, panels k and q.

Conversely, the features of the WGS and revWGS reaction reported in Figure 2.4, panels d, j, p, do not show appreciable variations compared to those reported in Figure 2.3 panels d, j, p, for the JM57-4Q catalyst.

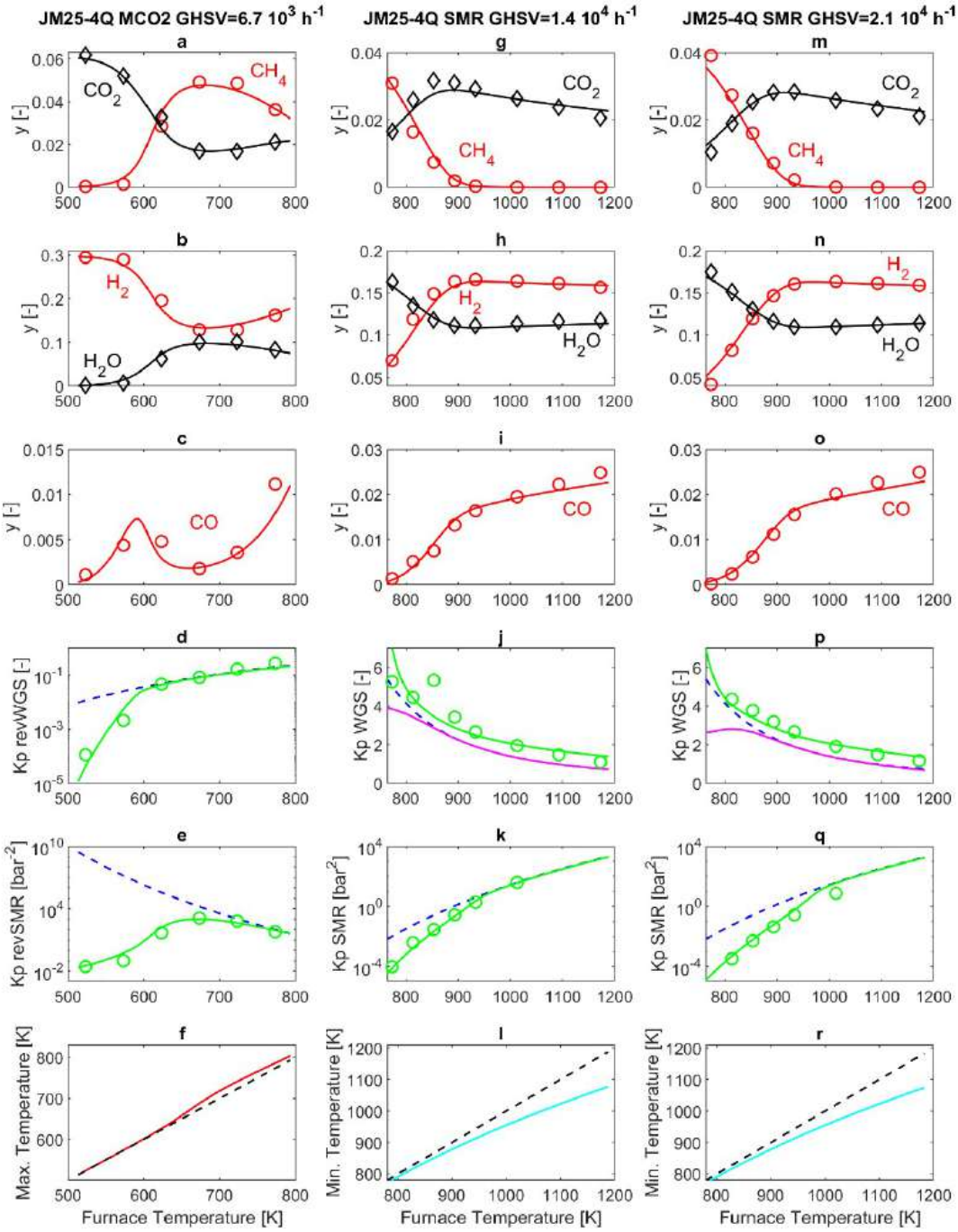

FIGURE 2.4: Results for the JM25-4Q catalyst. Panels **a-f**: MCO2 operating mode (GHSV = 6.7×10^3 h^{-1}). Panels **g-l**: SMR operating mode (GHSV = 1.4×10^4 h^{-1}). Panels **m-r**: SMR operating mode (GHSV = 2.1×10^4 h^{-1}). Symbols: experimental data. Lines: simulations. Panels **a-c**, **g-i**, **m-o**: compositions at the sampling point (exit of P-R2). Panels **d, j, p**: - - - $K_{p,WGS}$ calculated at the furnace temperature (Eq. 2.38); ——— model calculation and ○ experimental data of $\left(\prod_i p_i^{\nu_i}\right)_{WGS}$ at the sampling point (exit of P-R2). Panels **j, p**: ——— model calculation of $\left(\prod_i p_i^{\nu_i}\right)_{WGS}$ at the exit of the PBR. Panels **e, k, q**: - - - $K_{p,SMR}$ calculated at the furnace temperature (Eq. 2.38); ——— model calculation and ○ experimental data of $\left(\prod_i p_i^{\nu_i}\right)_{SMR}$ at the sampling point (exit of P-R2). Panels **f, l, r**: - - - furnace temperature; model results of: ——— maximum temperature in the PBR of the MCO2 reactor and ——— minimum temperature in the PBR of the SMR reactor.

2.4.4 MCO2 Laboratory reactor

Figure 2.5 reports simulation results for the MCO2 laboratory experimental reactor, obtained with a furnace temperature of 623 K. Modeling results are reported for all the three catalysts employed in this work. Experimental data of compositions, measured at the sampling point, are reported as well.

The first remark about the simulation results is that the kinetic parameters employed for the JM catalyst cause a high sensitivity of the SMR and revSMR reaction rates towards the water content in the reactant gas mixture. In MCO2 mode, where no H_2O is present in the reactor feeding gas, the revSMR and revWGS reactions are thus very fast at the reactor inlet, especially with the JM57-4Q catalyst. This is clearly visible Figure 2.5, particularly in the CH4 molar fraction plot (Figure 2.5 a), showing a steep increase at the reactor inlet, higher than with both the HMMC and the JM25-4Q catalysts. Further down in the reactor, water, being a reaction product, is present, as displayed by Figure 2.5 e. Therefore, the rate of formation of CH4 over the JM57-4Q catalyst visibly slows down, so that at the exit of the PBR the CH_4 molar fraction is only slightly higher than that obtained with the HMMC catalyst. This is confirmed by the experimental results of CH_4 molar fraction at the exit of the reactor: 5.1% with the JM57-4Q, 5.0% with the HMMC catalyst and 2.9% with the JM25-4Q catalyst.

Regarding the simulated temperature profiles (Figure 2.5 f), the fast kinetics of the exothermal revSMR at the entrance of the PBR causes a steep temperature increase of about 10 K with the JM57-4Q catalyst. A similar behavior, with a smaller temperature increase, is found also with the other two catalysts. Further down in the reactor, due to the reduced rate of the revSMR, the temperature of the PBR cools down and at the exit of the PBR it is practically equal to the temperature of the furnace for all the three simulated catalysts. Also in the downstream P-R1, where only gas phase WGS is considered to occur, temperature remains equal to the furnace temperature and no appreciable variations in composition is found (results not reported in Figure 2.5 f). In the subsequent post–reactor P-R2, due to the efficient heat exchange with the surrounding environment, temperature quickly drops to the ambient temperature (298 K) in a narrow length of about 7 mm. More in detail, temperature decreases to 523 K in a thin length of 0.3 mm, and then to 366 K in the subsequent 1 mm of length. Here, the simulation model, as discussed in Section 2.3.2.2 – Metal tube WGS kinetics, embeds a simulation of the revWGS reaction, catalyzed by the metallic piping. However, due to the low furnace operating temperature adopted in the MCO2 operating mode, and also to the almost instantaneous temperature drop down to the ambient temperature occurring in the post-reactor P-R2, no variation in composition is calculated by the model in the P-R2. No results are reported in Figure 2.5 for the P-R1 and P-R2 simulation results, and, in Figure 2.5, the experimental compositions measured at the sampling point (exit of P-R2) are plotted at the exit of the PBR section.

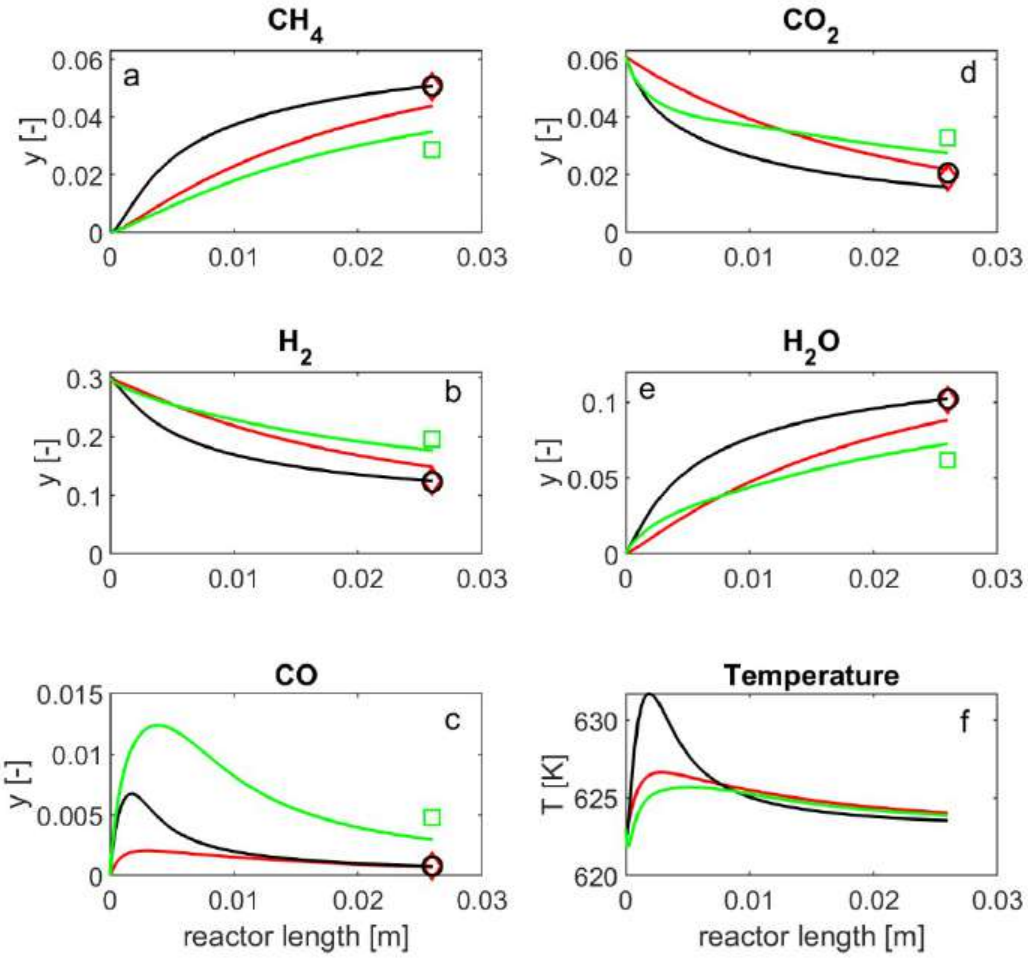

FIGURE 2.5: Results for the MCO2 operating mode (GHSV = 6.7×10^3 h^{-1}), furnace temperature 623 K. Lines: simulations. Simulation results are reported only for the catalytic section (PBR) of the reactor. Symbols: experimental data at the outlet of the laboratory reactor. Catalysts: ——, ◇ HMMC; ——, ○ JM57-4Q; ——, □ JM25-4Q.

2.4.5 SMR Laboratory reactor

Figure 2.6 reports the simulation results obtained for the experimental reactor in SMR operating mode, with furnace temperature 853 K and GHSV = 2.1×10^4 h^{-1}. The left hand sides of the figures show the modeling results obtained in the catalytic section of the reactor (PBR), while the right hand sides display the P-R2 modeling results.

In this case, 5% CH_4 is fed together with 20% steam, and therefore the simulated reaction rate with the JM25-4Q and JM57-4Q catalysts is hindered by the presence of water, and thus is visibly slower than in HMMC operating mode. In particular, with the HMMC catalyst, thermodynamic equilibrium is established after about 2 mm from the entrance of the PBR, corresponding to an almost complete consumption of methane and to the generation of an H_2 molar fraction of about 16%. Conversely, with the commercial catalysts, reaction rates are much lower and thermodynamic equilibrium is not reached within the PBR; H_2 molar fractions at the exit of the PBR are 14.5% and about 12% with JM57-4Q and JM25-4Q respectively.

Regarding the simulated temperature profiles within the PBR section, the fast reaction rate at the entrance of the HMMC PBR is associated to a temperature drop, after which, temperature raises to the furnace temperature. This deep temperature drop may be somehow overestimated due to the absence of the thermal axial dispersion term in the model; nevertheless, this possible inaccuracy does not influence the evaluation of the compositions at the exit of the PBR since thermodynamic equilibrium is reached quickly with the HMMC catalyst in these operating conditions. On the other hand, with the commercial catalysts, as a result of the slower kinetics, the temperature drop is smoother and milder (20 K with the JM57-4Q and 15 K with the JM25-4Q catalysts respectively). For all catalysts, temperature at the exit of the PBR is equal to the furnace temperature. As well as with the MCO2 reactor, also with the SMR reactor, no temperature or composition variations are evaluated by the simulation model in the post-reactor PR-1, which is not represented in Figure 2.6. Instead, in the post reactor PR-2, the model calculates variations not only in temperature but also in composition. This is due to the fact that, in SMR operating mode, on the one hand, the furnace temperature is higher than in MCO2 operating mode; on the other hand, the P-R2 is exposed to an external temperature of 523 K, higher than in the MCO2 case. As a result of the higher temperatures established in the P-R2, the simulation results indicate a non-negligible advancement of the WGS reaction. The WGS kinetics in P-R2, as already mentioned in Section 2.3.2.2 – Metal tube WGS kinetics, is based on the kinetic equation proposed by Xu and Froment (Eq. 2.29), with $k_{WGS,T_r} = 4.7\,\mathrm{kmol\,bar^{-1}\,m^{-2}\,h^{-1}}$, referred to the unit area of inner surface of the tube. Figure 2.6 reports the simulation results only for the first 3 mm of PR-2, where temperature is simulated to drop to the external temperature of 523 K (Figure 2.6 f), and where the model evaluates a slight, yet non negligible, advancement of the WGS reaction. Figure 2.6 demonstrates good agreement between simulated and experimentally measured molar fractions at the sampling point (exit of P-R2). All the modeling results presented in this work are obtained following this approach.

For sake of completeness, other literature WGS kinetic models have also been tested for the simulation of P-R2. The kinetic model proposed by Bustamante *et al.* [42, 43] (Section 2.3.2.1 – Gas phase WGS kinetics) for gas phase WGS reaction has been implemented in the simulation of the P-R2 discharge pipe, without giving any advancement in WGS conversion. A further simulation has been performed employing the kinetic

model proposed by Bustamante *et al.* [42, 43] (Section 2.3.2.2 – Metal tube WGS kinetics) for the WGS reaction occurring in an Inconel® 600 pipe. This kinetic model, when implemented into the P-R2 discharge pipe, results in thermodynamic equilibrium being reached for the WGS reaction inside P-R2 ($K_{p,WGS} = 86.7$ at 523 K), exceeding by far the real WGS conversion measured experimentally at the exit of the P-R2 piping. This indicates that the WGS kinetics in the Inconel® 600 piping is faster than in the AISI 316L tubes, probably due to the higher amount of Ni (72 wt% in Inconel® 600, versus 8 wt% in the AISI 316L).

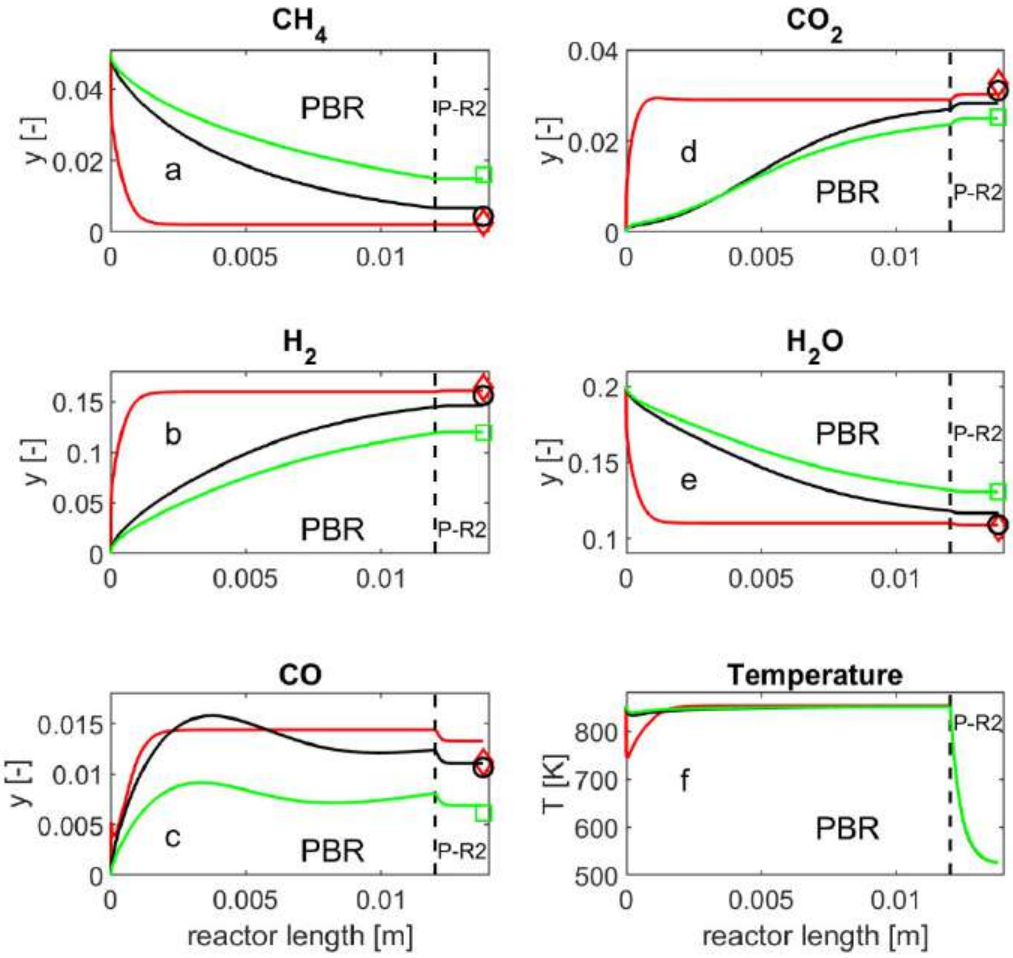

FIGURE 2.6: Results for the SMR operating mode (GHSV = 2.1×10^4 h^{-1}), furnace temperature 853 K. Lines: simulations. Simulation results are reported only for the catalytic section (PBR) of the reactor and for the first 3 mm of the second post-reactor (P-R2). Symbols: experimental data at the outlet of the laboratory reactor. Catalysts: ——, ◇ HMMC; ——, ○ JM57-4Q; ——, □ JM25-4Q.

2.5 Commercial and HMMC Catalysts: Comparative Assessment

The experimental data show that the investigated catalysts are all active in both SMR and in MCO2 reactions. The data show that the HMMC catalyst is more active than both K-free and K-doped industrial SMR catalysts in both reactions. The better activity of the HMMC catalyst is likely associated, for both reactions, to the definitely higher nickel loading, as well as, maybe, to the different support. It is evident that the composition of the industrial SMR catalysts are determined by the need of a very prolonged stability, both in terms of reduced sintering of nickel active phase and the support, and on a limited formation of carbon residues. Calcium aluminates are stable and refractory materials allowing to stabilize nickel particles in the SR reaction conditions, even if they can in some way slightly reduce the activity of nickel with respect to alumina. In any case, we remark that the HMMC catalyst does not show any deactivation in a one-day-long experiment in SMR in our conditions. In any case over both HMMC and JM57-4Q catalysts hydrogen yields above 90% are obtained at ca. 900 K.

Our data confirm, also in our conditions, the slightly lower activity of the K-doped commercial SMR catalyst with respect to the K-free catalyst [18] in the SMR reaction. As said, K-doping is useful to reduce carbon residue formation, in particular when natural gas treated contains significant amounts of higher hydrocarbons, propane and butane. The formation of carbon is in fact much more pronounced when higher hydrocarbons are treated. For this reason, in industrial plants a pre-reforming reactor is frequently used [47], working at lower temperature ($\sim$ 773 K), to steam reform higher hydrocarbons before the tubular reactor. As remarked above, our HMMC catalyst has a composition, which is comparable with that of pre-reforming catalysts. It seems interesting to remark that this catalyst, richer in nickel, is more active with respect to SMR even at 773 K, thus at a temperature where pre-reforming is usually conducted. Indeed, at this low temperature SR of propane and butane can already occur with high conversion and are much faster and favoured than SMR.

At low temperature, when the SMR reaction is under kinetic control, CO_2 is selectively produced over the K-doped catalyst while over the other catalysts CO is already detected among products. This either indicates that K-containing catalysts are more active in water gas shift reaction (supposing CO is the primary product of the steam reforming process) or, in contrast, K-doping also poisons retro-water gas shift reaction (supposing CO_2 is the primary product of the reaction, and CO is the final product). This point will be discussed later.

The trend of catalytic activity in MCO2 is the same as for SMR, *i.e.* HMMC > 57-4Q > 25-4Q, as it might be expected from the "micro-reversibility principle" [25]. In the cases of K-free catalysts, MCO2 reaction is highly selective to methane (approaching 100%) until 673 K, when the maximum conversion is reached, allowing a methane yield near 85%. In these conditions the reaction is still under kinetic control in our experiments, being CO_2 conversion still lower than that allowed by thermodynamics. At higher temperatures, however, when the reaction is, over these catalysts, already under thermodynamic control, CO is produced in significant amounts, as expected indeed by thermodynamics. A different situation is found over the K-doped catalyst, where conversion of CO_2 is significantly lowered with respect to undoped catalyst, and 10% CO yield is achieved upon CO_2 methanation also at low temperature (*i.e.* when thermodynamics allows complete CO hydrogenation). This behavior shows

that the rate of the "methanation" steps (MCO2 and MCO) are both lowered by K-doping. However, the reduced CO_2 conversion implies that either also the rate of the revWGS activity is reduced by potassium doping (supposing MCO2 as the sequence revWGS+MCO) or MCO2 is mainly parallel to revWGS. These data can be taken into consideration in parallel with the effect of K-doping on the selectivity to CO_2 in SMR. These data support the idea that a direct reversible way from CO_2 to CH_4, without the intermediacy of gaseous phase CO, indeed exists and is predominant in both senses. Thus, MCO2 and GRR (Reactions 2.3 and 2.5) are real inverse reaction whose reaction rates are both slowed down by K doping in both directions. The increased production of CO by the hydrogenation side and to CO_2 from the steam reforming side by K doping is a secondary effect: it indicates that revWGS reaction 2.6 is both parallel to CO_2 methanation and consecutive to CH_4 steam reforming, and is hindered at least at high temperature by K doping.

On the other hand, it can be interesting to remark that we have performed experiments in closely similar conditions at 773 K both feeding methane + water and feeding CO_2 + hydrogen. At this temperature, the reaction is under (or near) equilibrium conditions from both sides only on the HMMC catalyst. With the two industrial catalysts, at 773 K the reaction is, in our experiments, near equilibrium from the hydrogenation side, while is far from equilibrium from the steam reforming side. This is likely associated to the water excess in our SMR experiments, while in the conditions of MCO2 experiments water is a stoichiometric product, and to the need of large nickel particles to activate water for SMR at low temperature.

2.6 Conclusions

Regarding MCO2 and SMR catalysis on three different commercial and laboratory catalysts, it can be concluded that:

1. K-doped industrial SMR catalysts are less active than K-free samples also in our laboratory reactor conditions in SMR. They however produce higher CO_2 and hydrogen selectivities at low temperature where the reaction is under kinetic control, with respect to K-free catalyst.
2. The industrial SMR catalysts are also active in CO_2 methanation, where K-doping also causes some deactivation and lowers CH_4 selectivity at low temperature where the reaction is under kinetic control.
3. The home-made HMMC catalyst, richer in Nickel, is more active than industrial catalysts in both SMR (95% hydrogen yield at 900 K) and CO_2 hydrogenation (86% methane yield with 100% selectivity at 623 K). Although this catalyst is stable for one-day laboratory experiments, it is clear that composition and properties of industrial catalysts are mostly related to stability issues, for very prolonged use in SMR.
4. The experimental results suggest that the reverse water gas shift reaction is mainly parallel with respect to CO_2 methanation and mainly successive to "global reforming reaction" that produces directly CO_2 from methane and water.

From the point of view of reactor modeling, it can be stated that:

5. A steady-state, pseudo-homogeneous 1D non-isothermal reactor model indicates that temperature non-uniformities can be non-negligible in laboratory experimental reactors for MCO2 and SMR testing.

6. Data at thermodynamic equilibrium give information about possible progress of the WGS reaction in the discharge piping, which can be more easily included into the simulation model rather than prevented in the experimental apparatus [41–43].

Comparison between modeling results and experimental data allows to state that:

7. The Xu and Froment kinetic model [8] is applied successfully to both high and low steam-to-carbon operating conditions.
8. Three set of values for the parameters of the Xu and Froment kinetic model [8] are proposed, adapted to the three catalysts under consideration.
9. In the kinetic model, the H_2O adsorption coefficient adopted for the commercial catalysts is about two orders of magnitude higher than for the laboratory made catalyst, and this is in line with the expectations, considering that the commercial catalysts are added with Ca and K in order to promote H_2O adsorption.
10. The WGS reaction occurring in the metal piping downstream the reactor is well simulated again through the corresponding kinetic equation proposed by Xu and Froment [8].

Chapter 3

Model of Full-Scale Industrial SMR Reactor

Diagnostics and prognostics of natural gas steam reforming (NGSR) reactors are of utmost importance for solid oxide fuel cell (SOFC) systems, where a fuel processor fault can cause damage to the SOFC stack. Most common faults are due to carbon deposition. We investigate this phenomenon through a model based on microscopic mass, energy and momentum balances of a tubular NGSR reactor. The model includes a detailed local reaction kinetics specific for Ni-based catalysts, and is integrated with a finite element method (FEM) implemented through COMSOL Multiphysics® 5.2. Results obtained from the simulation of a laboratory scale reactor are validated on the basis of literature data. Furthermore, the model is applied to an NGSR fuel processor designed for a 1.1 kW SOFC system. The model allows to identify the area where carbon deposition is expected to occur, which is a key feature in view of developing specific diagnostic and prognostic tools. The simulation results demonstrate that safety criteria based on the feedstock steam to carbon (S/C) ratio can be misleading in a number of operating conditions.

3.1 Introduction

The importance of early detection, isolation, identification and possibly correction of faults has been evidenced by previous research works on solid oxide fuel cell (SOFC) plants [90–92]. With reference to the SOFC power plant scheme reported in Figure 3.1, the possible types of faults have been grouped into four main categories (classes) [90, 91]: (i) *air leakage*: this fault consists in leakage of air between the air blower and the SOFC stack itself; (ii) *fuel leakage*: in the reformer, the methane/steam feed is converted into a hydrogen rich mixture. Leakage is likely to occur between the exit of the reformer and the entrance of the SOFC stack because of the small dimensions and high diffusivity of the hydrogen molecule; (iii) *SOFC stack degradation*: an increase of the SOFC internal losses (activation, ohmic and diffusion losses) leads to a reduced electrochemical performance and efficiency. SOFC internal losses can rise progressively or abruptly. A progressive increase is related to functional degradation during the working life of the cell, while an abrupt increase is due to an unexpected breakdown in the stack [90]; and (iv) *reformer degradation*: deterioration of the reformer catalyst reduces hydrocarbons conversion.

In [91], it was demonstrated that faults of the natural gas steam reforming (NGSR) reactor are particularly dangerous. Indeed, when natural gas (NG) conversion in the NGSR reactor is reduced, high amounts of NG are fed directly into the SOFC stack.

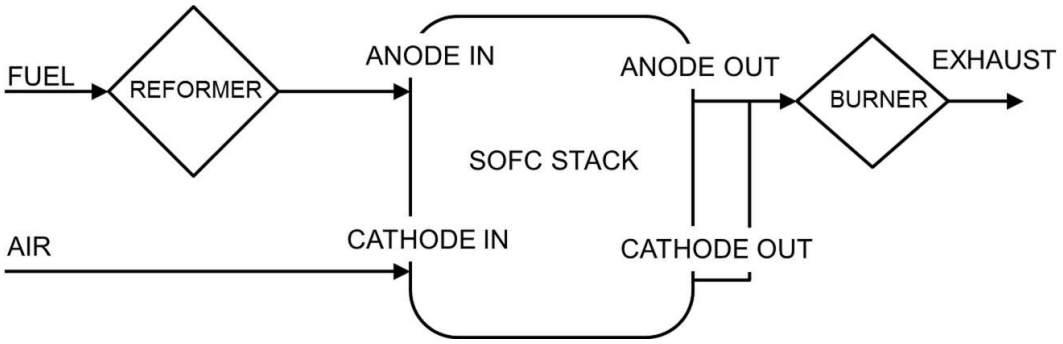

FIGURE 3.1: Scheme of the SOFC system.

In these conditions, NG can undergo steam reforming inside the SOFC stack, causing steep thermal gradients, which can easily exceed the maximum threshold allowed by the SOFC stack materials.

Despite NGSR reactors implement an established technology, they still present some issues. In particular, carbon can deposit and coat the active sites of the catalyst, reducing its activity and limiting gas diffusion through the catalytic bed. Carbon can deposit under various different forms, including graphitic form, amorphous carbon, carbon nanotubes and carbon nanofibers [93, 94]. It is well known that coke deposition is inhibited by a high steam to carbon ratio (S/C, defined as the ratio between the number of water molecules and the total number of carbon atoms present). Even if generally S/C is in the range 2-6, nevertheless, the problem of carbon deposition is still not solved, as widely discussed in the literature [1, 95–98].

In the present work, a model is proposed for the NGSR reactor. Modelling of industrial NGSR reactors has received wide attention so far [6, 99–102], mainly aimed at optimizing operating conditions and identifying innovative geometries, particularly with reference to the arrangement of the burners within the combustion chamber where the NGSR reactor tubes are situated. These studies include the kinetics of the NGSR reactions, but to date there are no literature papers in which the kinetics of the coke deposition reaction is embedded into the NGSR reactor model, and this is a distinctive feature of the present work. The kinetics of the coke deposition reaction has been included into a kinetic subroutine taking into account also the rate of all the other main reactions involved, in particular steam reforming of methane, ethane, propane and butane (SMR, ESR, PSR and BSR respectively). All these kinetics have been derived from the published literature for Ni-based catalysts, which are widely applied in NGSR reactors for SOFC plants [103, 104].

The model has been applied to two reactors of different scale: (i) laboratory scale; (ii) SOFC plant reactor [105]. The results obtained for the laboratory scale reactor have allowed model validation through comparison with previous literature results for a similar type of NGSR reactor [55]. Application to a reactor designed for a 1.1 kW SOFC system is discussed as well, and is intended to provide the basis for the development of a diagnosis and prognosis tool based on pattern recognition techniques, which will be developed in a subsequent phase. A number of fault detection and isolation (FDI) methods have been proposed and applied to a variety of systems. A survey can be found in [106], where they are classified as: (i) quantitative model-based; (ii) qualitative model-based, and (iii) process history-based methods. In practice, the classification regards the approach used to produce the fault data for the FDI: in the

first two cases, the data are obtained from a model developed for the system under analysis, while the latter approach is based on historical experimental data.

In a previous work [107], we have demonstrated a general fault diagnosis tool for SOFC-based power plants, designed using quantitative models of the whole generation plant coupled to a support vector machine (SVM) classifier. This FDI tool has been proved to be robust against modelling and measurement errors and is compliant with practical deployment, correctly functioning with different operating conditions and fault sizes. The work presented in this paper is intended to provide the basis for the development of a similar tool, specifically devoted to the diagnosis and prognosis of the NGSR reactor of an SOFC power plant.

The paper is structured as follows: in Section 3.2, the NGSR reaction scheme is depicted; in Section 3.3 the geometry is described for the two NGSR reactors simulated in the paper: laboratory size and SOFC system reactor size. Section 3.4 illustrates the main equations included into the model, in particular mass, energy and momentum balances. These are coupled to the local kinetics, including primarily the kinetics of hydrocarbon steam reforming (SR) and of carbon formation. Simulation of thermodynamic equilibrium is discussed in depth. Section 3.5 presents, at first, the results obtained for the evaluation of possible carbon formation according to the thermodynamic equilibrium approach. Then, simulation results for the laboratory NGSR reactor are discussed and validated by comparison to previous literature results. Finally, simulation results for a 1.1 kW SOFC system NGSR reactor are presented, with emphasis on carbon formation; discrepancies with carbon formation predictions derived from the thermodynamic approach are highlighted. In Section 3.6, the main conclusions and future perspectives are summarized.

3.2 Reaction Scheme

The general formulation of steam reforming reactions of hydrocarbons is [108]:

$$C_nH_m + nH_2O \rightleftharpoons nCO + \left(n + \frac{m}{2}\right) H_2 \tag{3.1}$$

In the case of methane steam reforming, this becomes:

$$CH_4 + H_2O \rightleftharpoons CO + 3\,H_2 \qquad \text{(SMR)} \tag{3.2}$$

It is widely accepted [6, 37, 53, 99, 109] that this is accompanied by the water gas shift (WGS) reaction:

$$CO + H_2O \rightleftharpoons CO_2 + H_2 \tag{3.3}$$

In the reaction scheme, the methane cracking (MC) reaction [96] is included as well, which deposits carbon on the catalyst, mainly under the form of filamentous carbon or carbon nanotubes [110]:

$$CH_4 \rightleftharpoons C + 2\,H_2 \tag{3.4}$$

The ΔH^0_{298K} of the reactions are reported in Table 3.1, showing that reforming reactions are strongly endothermal, while WGS is slightly exothermal and MC is endothermal.

TABLE 3.1: Standard enthalpy change of the reactions involved in the NGSR process.

Reaction	ΔH^0_{298K} [kJ mol^{-1}]	**Source**
3.1	206.27 (for CH_4)	[111]
	348 (for C_2H_6)	[112]
	498 (for C_3H_8)	[113]
	649.9 (for C_4H_{10})	[114]
3.3	-41.19	[111]
3.4	74.91	[111]

In the reaction scheme, further reactions leading to coke deposition, such as the Boudouard reaction, are not taken into account:

$$2\,CO \rightleftharpoons C + CO_2 \tag{3.5}$$

Even though nickel catalysts for NGSR are reported to be active towards reaction 3.5 [115, 116], only few studies have been carried out to determine the kinetics law. Furthermore, the higher the amount of steam and hydrogen, the lower the reaction extent [117]. In addition, reaction 3.5 is not favoured by high temperatures [96], such as the typical NGSR operative conditions. Therefore, in the typical operating conditions considered in our simulations, the Boudouard reaction is assumed to be inhibited, and, as previously suggested by Tøttrup [117], it is not included in the reaction scheme taken as a basis for model development.

NG fed into the reactor is assumed to be desulphurized, and thus no sulphur-containing compounds are taken into account in the reaction scheme.

3.3 Reactor Geometry

3.3.1 Laboratory Scale NGSR Reactor

The laboratory scale fixed-bed catalytic tubular reactor is depicted in Figure 3.2. The catalytic section is placed inside a quartz tube and is kept in position by two holders made out of glass wool. The tube has an inner diameter of 6 mm, and the catalyst fixed-bed is 10 mm long. The two sections filled with glass wool, upstream and downstream the catalyst, are each about 1.5 cm long. The catalyst is Ni oxide on calcium aluminate, JM57-4 Johnson Matthey series. The pellets are crunched in particles of about 0.2 mm size, dispersed with silica glass particles and then loaded into the quartz tube. The entire reactor is placed inside a tubular furnace with controlled temperature.

On the one hand, the reactor described above is set up at DICCA (University of Genoa) [118]; however, no NGSR experimental campaigns have been carried out yet. On the other hand, the geometry described above is very similar to one previously reported in the literature [55], allowing comparison and validation of the results obtained by the NGSR reactor simulation tool presented in this work.

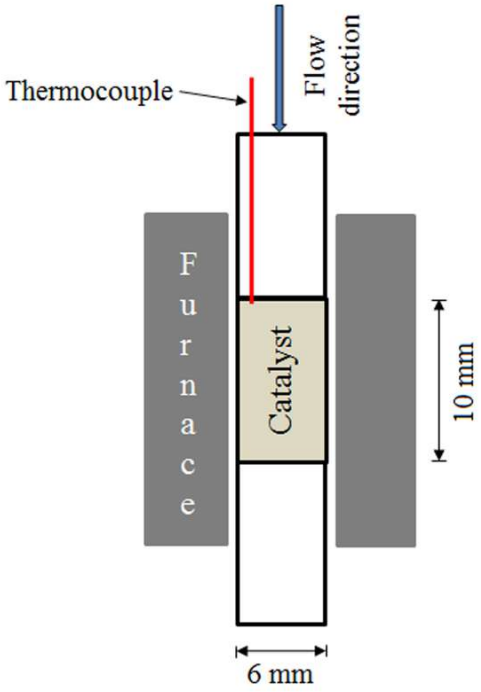

FIGURE 3.2: Scheme of laboratory scale NGSR reactor.

3.3.2 SOFC Plant Scale NGSR Reactor

The tubular NGSR reactor depicted in Figure 3.3, employed in an experimental 1.1 kW SOFC system [90, 91], is simulated in the present work. The reactor has an inner diameter of 125 mm and a length of 700 mm, it is coated with a 50 mm thick thermal insulation on all surfaces and heated through an electrical heating jacket surrounding the reactor itself. The catalyst fills a 400 mm long portion of the tubular reactor, and is assumed to be the same Ni-based catalyst described in Section 3.3.1 - Laboratory Scale NGSR Reactor. The reactor is fed with a mixture of steam and desulphurized NG; fuel and steam are mixed in the proportioning nozzle and then the mixture is fed into the catalytic section of the reformer.

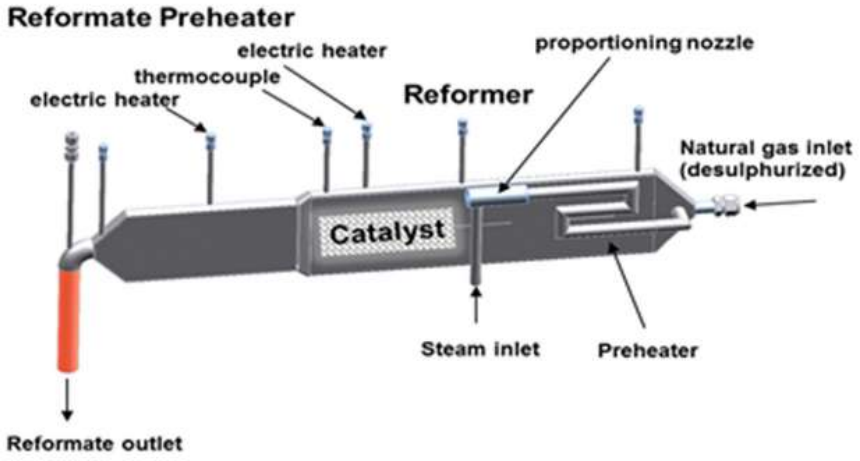

FIGURE 3.3: Scheme of experimental NGSR reactor for an 1.1 kW SOFC system [91].

3.4 Modeling

The mathematical model is developed for three different NGSR reactors: (i) a fictitious 0-D batch reactor, for thermodynamic validation of the equilibrium compositions evaluated by the kinetic subroutine; (ii) the steady-state laboratory scale tubular reactor; and (iii) the steady-state tubular reactor for application in a 1.1 kW SOFC system. In simulating the tubular reactors, the main underlying assumption is that of cylindrical symmetry, based on which we have developed 2-D simulation models in function of radial and axial reactor co-ordinates. The radial coordinate has its origin at the axis of the tube, and the axial co-ordinate collapses with the reactant flow direction, with origin located at the tube entrance. Table 3.2 highlights the differences between the three reactor models, in terms of type and mathematical formulation of the balance equations considered.

TABLE 3.2: Equations implemented in the three NGSR reactor models. (S-S: Steady state; T-D: Time-dependent)

NGSR reactor	**Microscopic balances**					
	Mass		**Energy**		**Momentum**	
	S-S	T-D	S-S	T-D	S-S	T-D
0-D batch		X				
tubular S-S (laboratory size)	X		X			
tubular S-S (1.1 kW SOFC system size)	X		X		X	

Generally speaking, current fixed-bed reactor modeling approaches are based on simplifying assumptions, such as pseudo homogeneity, effective transport parameters and unidirectional plug-flow [119]. In our modelling approach, some of these hypothesis have been retained, and are common to all the cases depicted in Table 3.2: (i) the fixed-bed catalytic reactor is simulated as a pseudo-continuum, where both fluid and solid phases are modelled as inter-penetrating continua, i.e. as if they coexist at every point in the tube; (ii) the catalyst is Ni oxide supported on calcium aluminate, in particles of about 0.2 mm size, dispersed with silica glass particles; the fixed-bed void degree is uniform and equal to 0.4; (iii) due to the small dimensions of the catalyst particles, no convection and diffusion inside the catalyst pores is taken into account; (iv) the fuel feedstock is composed by a mixture of steam and natural gas; (v) carbon, when formed, is considered to be in solid phase, without differentiating among the different forms of carbon (graphitic form, amorphous carbon, carbon nanotubes and carbon nanofibers); (vi) carbon accumulation during time and consequent catalyst deactivation is not simulated.

The model implements mass, energy and momentum balances, coupled to a kinetics subroutine. The equations are all written in local form for the fixed catalytic bed of the reactor, with reference to Eulerian coordinates, accounting for transport of mass, energy and momentum through a granular medium. All the equations are written in the typical form for non-ideal tubular reactors [48]. In the following sections, the equations are presented in the most general form, and simplifications will be discussed when presenting the application to the three different reactor types.

3.4.1 Mass balance

The mass balance (Eq. 3.6) is written in transient form, and includes mass accumulation (*i.e.* the time derivative term), diffusive and convective fluxes, and the reaction

term [48]:

$$\rho \frac{\partial \omega_i}{\partial t} + \nabla \cdot \mathbf{j}_i + \rho \left(\mathbf{u} \cdot \nabla \right) \omega_i = R_i \tag{3.6}$$

where ω_i is the mass fraction of the i-th component. The diffusive flux $\mathbf{j}_i$ is expressed by Fick's law:

$$\mathbf{j}_i = -\rho \mathcal{D}_i^M \nabla \omega_i \tag{3.7}$$

where:

$$\mathcal{D}_i^M = \frac{1 - \omega_i}{\sum_{k \neq i} \frac{x_k}{\mathcal{D}_{ik}}} \tag{3.8}$$

The reaction rate of the i-th component is defined according to Eq. 3.9, which accounts for the contributions of all the reactions included in the reaction scheme; ν_i is the stoichiometric coefficient, negative for reactants and positive for reaction products:

$$R_i = \sum_j \nu_{ij} r_j \tag{3.9}$$

3.4.2 Energy balance

The energy balance (Eq. 3.10), is written in steady-state form, considering that the fluid and the solid phase have the same temperature at each point of the catalytic bed. Convective and conductive energy fluxes, and the enthalpy change of the reactions involved [48], are included:

$$\rho c_P \mathbf{u} \cdot \nabla T + \nabla \cdot \mathbf{q} = Q_P \tag{3.10}$$

where the heat flux $\mathbf{q}$ is expressed through the Fourier's law:

$$\mathbf{q} = -k \nabla T \tag{3.11}$$

In Eq. 3.10 and 3.11, the specific heat c_P and the heat transport properties of the catalytic bed (k) are effective parameters accounting for the fluid flow through the catalyst particles through the following averaged approach:

$$c_P = c_P^{fluid} \, \varepsilon + c_P^{solid} \, (1 - \varepsilon) \tag{3.12}$$

$$k = k^{fluid} \, \varepsilon + k^{solid} \, (1 - \varepsilon) \tag{3.13}$$

The enthalpy change of the reactions involved is represented by the term Q_P:

$$Q_P = \sum_j \left(-\Delta H_j \right) \, r_j \tag{3.14}$$

3.4.3 Momentum balance

As already mentioned, current fixed-bed reactor modelling approaches are often based on simplifying assumptions, mainly regarding the fluid flow field, which is

often approximated as unidirectional plug-flow [119]. These simplifications are justified by the need of computational time saving, whose importance is currently getting reduced. In parallel, alternative and more comprehensive approaches based on computational fluid dynamics (CFD) are under development and are rapidly becoming standard tools for the analysis of chemical reacting flows. The contribution of CFD to simulate geometrically complex flows is a more fundamental understanding of the transport and reaction phenomena in such kind of reactors. However, for multiphase reactors, such as fixed or fluidized beds, the use of CFD is relatively new and methods are still under development.

One CFD methodology applied to fixed-bed simulation is to solve the actual flow field between the particles. This approach does not simplify the geometrical complexities of the packing, or replace them by the pseudo-continuum. The governing equation for the interstitial fluid flow itself are solved directly [120]. The equations of the interstitial approach are well established; however, the geometric modelling and grid generation become complicated and the computational demand rise significantly [119].

An alternative approach in the application of CFD to packed bed reactor modelling involves the replacement of the actual packing structure with an effective continuum [121, 122]. The velocity field can be obtained from a modified momentum balance [123] or a form of the Brinkmann-Forcheimer-extended Darcy (BFD) equation, which accounts for convection and diffusion into the catalyst pores [124]. This approach provides an averaged superficial velocity field, usually in the form of radially varying axial component of velocity, which is an improvement over the classical assumption of plug-flow. These velocity fields have been used in improved models of the fixed-bed transport and reaction [125].

In this framework, as already stated in hypothesis (i), we simulate the catalytic fixed-bed through a pseudo-continuum approach, where both fluid and solid phases are modelled as inter-penetrating continua. According to hypothesis (iii) no convection and diffusion inside the catalyst pores is taken into account. Also, steady state operating conditions are considered. Thus the classical form of the Darcy equation is implemented in the model:

$$\mathbf{u} = -\frac{\kappa}{\mu}\nabla p \tag{3.15}$$

3.4.4 Local Kinetics

A distinctive feature of this work is the kinetic simulation of the reaction scheme considered. The various kinetics models proposed in the literature for the various steam reforming reactions are reviewed in the specific sections below, in particular Section 3.4.4.1 - SMR kinetics, and Section 3.4.4.2 - Heavier-than-methane hydrocarbons kinetics. Reversible reaction rates vanish at thermodynamic equilibrium; a detailed check of the reliability of the evaluation of thermodynamic equilibrium performed by the local kinetic subroutine is presented in Section 3.5.1.2 - Thermodynamic Validation of the Kinetic Model.

3.4.4.1 SMR kinetics

The kinetic subroutine contains the kinetic rate law of hydrocarbons steam reforming and, in particular, of methane which is the major component of NG. The kinetics of the SMR process have been widely studied in the literature [126–128], and an overview for Ni-based catalysts is given by [129, 130]. In [130], activation energies in the range 29-182 kJ mol^{-1} are reported, together with kinetic rate laws with first order dependencies in p_{CH_4}. Detailed equations accounting for the presence of the other reactants and products, and including the coverage of the catalyst active sites by reactants, intermediates and products, are reported as well. More comprehensive approaches include an analysis of the elementary step mechanisms, and in particular Aparicio [131] has presented a 13-step micro-kinetic model in which the surface reaction is rate-determining. Methane dissociation has been found to be rate-limiting in several experimental studies [132, 133]. Other studies have concluded that oxidation with surface oxygen is rate-limiting [99, 126, 130, 134]. Xu and Froment [99] have suggested that methane is only partially dehydrogenated before reacting with surface oxygen, and three independent oxidation channels have been considered rate-determining for the overall reactions. Xu and Froment [99] have proposed an activation energy of 240 kJ mol^{-1} and detailed kinetics equations. Further developments have incorporated the density functional theory (DFT) modelling [135, 136].

In this complex scenario, the detailed rate equations proposed by Xu and Froment [99] have been widely applied in a number of works on SMR reactors simulation [6, 101, 102]. Recently, this approach has been followed also for the simulation of internal SMR in SOFCs [137], even if, following a pioneering approach proposed by Achenbach [138], the SMR kinetics models previously adopted in SOFC simulation have been first order dependencies in p_{CH_4} [139–146], with an activation energy in the range 95-210 kJ mol^{-1}. Recently, Wang *et al.* [140, 141] have proposed an innovative first order kinetics expression and have pointed out that first order kinetics are more suitable in the low S/C range (S/C < 1) desirable for internal SMR in SOFCs. On the other hand, the detailed rate equations by Xu and Froment [99] have been developed for the high S/C range (S/C > 1). In the present paper we simulate NGSR reactors with S/C ratios in the range 2-4, and thus we adopt the latter model, whose main equations are reported below. The reaction scheme proposed by [99] includes the combination between SMR and WGS:

$$CH_4 + 2\,H_2O \rightleftharpoons CO_2 + 4\,H_2 \tag{3.16}$$

referred to as global reforming reaction (GRR).

Xu and Froment SMR, WGS and GRR reaction rates are based on a Langmuir-Hinshelwood approach [99] and are reported in Section 2.3.1.4

3.4.4.2 Heavier-than-methane hydrocarbon kinetics

Ethane, propane and butane SR kinetics are included as well. NG includes only a small fraction of these hydrocarbons, which produce a significant amount of hydrogen (per mole of carbon) while causing issues in the process [147, 148]. The open literature about ESR, PSR and BSR on Ni-based catalysts is rather restricted. In all cases, at thermodynamic equilibrium, the higher hydrocarbons SR reactions are considered completely shifted towards the products, and thus irreversible kinetic expressions are used. Christiensen [149] has investigated the adiabatic pre-reforming of hydrocarbons, identifying the rate determining steps. He has considered the kinetic expression

previously proposed by Tøttrup [150] for the steam reforming of n-heptane on a Ni catalyst supported by magnesium oxide, at industrial test conditions. Christiensen [149] has extended this expression also to the kinetics of the steam reforming of ethane, butane and higher hydrocarbons:

$$r_{C_nH_m} = k_{C_nH_m} \frac{\exp\left(-\frac{E_a}{RT}\right) p_{C_nH_m}}{\left[1 + 25.2\, p_{C_nH_m}\left(\frac{p_{H_2}}{p_{H_2O}}\right) + 0.077\left(\frac{p_{H_2O}}{p_{H_2}}\right)\right]^2} \tag{3.17}$$

The values of the activation energies and pre-exponential factor for ethane and butane have been retrieved from Rostrup–Nielsen [151]. The values of the kinetic parameters are reported in Table 3.3.

TABLE 3.3: Parameters of ESR and BSR kinetics (from [151]).

	k [mol h^{-1} m^{-2}]	E_a [kJ mol^{-1}]
C_2H_6	120	75.73
C_4H_{10}	138	77.82

Li *et al.* [152] has proposed an expression for the PSR kinetics. In their work, the authors have developed a rate law for PSR for both Rh based and Rh-Ni catalysts. The kinetic results have shown that the rate of propane steam reforming strongly depends on the partial pressures of both propane and steam. According to these kinetic features, a Langmuir–Hinshelwood model has been applied and the rate of propane reforming has been deduced as:

$$r_{C_3H_8} = \frac{k_{C_3H_8} K_1 p_{C_3H_8} K_2 p_{H_2O}}{\left(1 + K_1 p_{C_3H_8} + K_2 p_{H_2O}\right)^2} \tag{3.18}$$

$$k_{C_3H_8} = A \exp\left(-\frac{E_a}{RT}\right) \tag{3.19}$$

The values of the kinetic parameters appearing in equations 3.18 and 3.19 and applied in our simulation model are those for Rh-Ni catalysts, and are listed in Table 3.4.

TABLE 3.4: Parameters of the PSR kinetics (from [152]).

K_1 [bar^{-1}]	K_2 [bar^{-1}]	$k_{C_3H_8}$ [mmol g^{-1} s^{-1}]	A [mmol g^{-1} s^{-1}]	E_a [kJ mol^{-1}]
73.34	1.13	4.63	4.3×10^4	42.5

3.4.4.3 Carbon formation kinetics

A kinetic equation for carbon formation via methane decomposition is included as well. Previous literature works [153, 154] have proposed a kinetic model, derived from experimental data of carbon formation in a mixture of methane and hydrogen over a Ni–Al_2O_3 catalyst. More in detail, in [153], the dependence of r_{MC} as function of p_{CH_4}, p_{H_2} and T has been deduced by analyzing the mechanism of methane decomposition

(reaction 3.4) into carbon and hydrogen, and keep in consideration the catalyst properties through a parameter n representing the number of catalyst active centers involved in the adsorption of one molecule of methane. Catalyst deactivation during time, due to carbon deposition, has been addressed as well. When the catalyst if fully active, *i.e.* carbon deposition has not occurred yet, the rate of carbon formation has been found to be:

$$r_{MC} = k_C \frac{p_{CH_4} - \frac{p_{H_2}^2}{K_{p,MC}}}{\left(1 + k_H \sqrt{p_{H_2}}\right)^n} \tag{3.20}$$

The kinetic terms in Eq. 3.20 are expressed as follows:

$$k_C = \exp\left(K - \frac{E}{RT}\right) \tag{3.21}$$

$$k_H = \exp\left(K_H - \frac{E_H}{RT}\right) \tag{3.22}$$

According to hypotheses (v) and (vi) of the model, we apply the kinetic equations for solid carbon formation without differentiating among the different forms of carbon, while catalyst deactivation as a consequence of carbon formation is not taken into account. Values of the kinetic parameters are given in Table 3.5.

TABLE 3.5: Parameters of the MC kinetics (from [153]).

Parameter	**Value for $n = 2$**	**Units**
K	20.417	–
E	1.037×10^5	$\mathrm{J\,mol^{-1}}$
K_H	-20.91	–
E_H	-1.4874×10^5	$\mathrm{J\,mol^{-1}}$

3.4.5 Thermodynamics

As already pointed out, at thermodynamic equilibrium, all the higher hydrocarbons SR reactions are considered completely shifted towards the products, and thus irreversible kinetic expressions are used. Instead, the kinetic equations 2.28-2.30 and 3.20 reported above for SMR and MC respectively are reversible kinetics; as such, they embed the thermodynamic equilibrium constant K_P, and vanish when equilibrium conditions hold. The thermodynamic constants K_P are expressed through temperature dependent equations, which are reported in Table 3.6. The K_P of SMR and WGS reactions are interpolation of literature data [12]. The K_P of MC is taken from [153].

In parallel, an additional and independent model for thermodynamic equilibrium analysis, based on the classical method of minimization of the total Gibbs free energy [62, 116, 155, 156], has been developed. The values of the $\Delta G_{fi}^0(T)$ have been taken from the literature [157]. The chemical species which are supposed to be present in the mixture under study are CH_4, H_2O, H_2, CO_2, CO for the gas phase and graphitic carbon for the solid phase. No higher hydrocarbons are considered. Also in this case

TABLE 3.6: Thermodynamic equilibrium constant K_P: expressions implemented in the simulation model.

Equation	Source
$\log K_{P,SMR} = -11269.82\,T^{-1} + 12.63$	Interpolation of data from [12]
$\log K_{P,WGS} = 2022.33\,T^{-1} - 1.89$	Interpolation of data from [12]
$K_{P,GSR} = K_{P,SMR}\,K_{P,WGS}$	
$K_{P,MC} = 5.088 \times 10^5 \exp\left(\frac{9.12 \times 10^4}{R\,T}\right)$	Equation from [153]

graphitic carbon has been considered representative of all the different forms of carbon. The method of minimizing of the total Gibbs energy of the mixture allows to evaluate the amount of each species which is obtained when, starting from a mixture with a certain composition, all the possible chemical reactions occur among the different species until conditions of thermodynamic equilibrium are reached. These conditions of thermodynamic equilibrium change with temperature and pressure. This method is based on a system of algebraic equations to be solved numerically [93, 158]:

$$\begin{cases} \sum_i n_i\,a_{ik} - A_k = 0 \qquad i = CH_4, H_2O, H_2, CO_2, CO \\ \Delta G^0_{fi}(T) + R\,T \ln a_i + \sum_k \lambda_k a_{ik} = 0 \end{cases} \tag{3.23}$$

We point our that the minimal Gibbs free energy approach equations have not been embedded into the overall NGSR reactor model. Instead, they have been solved (in C language) as an independent modelling tool, and used to check the reliability of the thermodynamic equilibrium predicitons of the overall NGSR reactor model.

3.4.6 Model integration

The NGSR reactor model equations form a partial differential and algebraic equation (PDAE) system. The boundary conditions for the differential equations are flowrate, composition and temperature of the feeding mixture. A further boundary condition expresses the heat exchange through the reactor wall, when applying the microscopic energy balance equation to the SOFC scale NGSR reactor. In that case, the contribution of the heat source Q_{vd} at the reactor wall is taken into account, accounting for the presence of an electrical heating jacket surrounding the reactor:

$$Q_{vd} = \frac{R_{el}\,I^2}{2\pi\,r\,L} \tag{3.24}$$

The resolution of the PDAE system needs the implementation of a numerical method. To this end, the finite element method (FEM) is selected, which is implemented by COMSOL Multiphysics, version 5.2 [159]. The simulations have been run using the stationary solver MUMPS (MUltifrontal Massively Parallel sparse direct Solver), embedded in COMSOL Multiphysics 5.2. Sensitivity analysis of model results towards mesh number has been investigated, and the results are reported in Table 3.7. We consider simulation number 3 as a reference, employing a very dense mesh (4.91×10^5 mesh elements). Simulation number 2, with a smaller number of mesh elements (2.98×10^5) allows to obtain very similar results (average difference $< 0.5\%$ in the resulting distributions of the chemical-physical variables within the NGSR reactor).

Further runs of the model with a further reduced number of mesh elements have displayed increased deviation of the values of the chemical-physical variables compared to the reference simulation number 3. In particular, simulation number 1 (3.16×10^4 mesh elements) has not even reached convergence. In the light of the considerations above, the NGSR reactor simulations presented in this work have been run with a number of mesh elements ranging between 3×10^5 and 5×10^5. With this mesh number, the model runs typically in 10 minutes on an Intel Core i5® CPU running at 3.20 GHz with 16 GB of RAM (Table 3.7). This running time is acceptable in order to generate the large pool of data required to train diagnostics and prognostics tools.

TABLE 3.7: Model sensitivity against number of mesh elements.

Simulation no	**No of mesh elements**	**Duration** [s]	**RAM use** [GB]
1	3.16×10^4	165 (no convergence)	1.77
2	2.98×10^5	533	5.03
3	4.91×10^5	842	6.83

Input data of the model are the geometrical data of the reactor, inlet temperature and composition of the reacting mixture, resistance and electrical current supplied to the electrical heating jacket, when present. Then, model results are the distributions of all the chemical-physical variables within the NGSR reactor, and in particular the composition and temperature of the reactant gas along the reactor length.

3.5 Results and discussion

3.5.1 Thermodynamics

The evaluation of the gas composition at thermodynamic equilibrium under given operating conditions is of central importance, because it is a reference point for the detailed NGSR reactor simulation. First, the results obtained from the minimal Gibbs free energy approach are presented. Then, the agreement between the minimal Gibbs free energy approach and the thermodynamic equilibrium as evaluated by the kinetic subroutine of the NGSR model is discussed.

3.5.1.1 Evaluation of carbon formation on the basis of the minimal Gibbs free energy approach

At first, the minimal Gibbs free energy approach, Eq. 3.23, has been applied to the study of the thermodynamic equilibrium of starting binary mixtures of methane and water with different S/C values and at different temperatures and pressures.

The results reported in Figure 3.4 have been obtained with 1 kmol of starting CH_4-H_2O mixtures with various S/C ratio; the results reported in the figures show the amount (in kmol) of the various chemical species obtained when all the possible chemical reactions occur and equilibrium is reached at a well-defined temperature and pressure. Carbon formation occurs, according to the present thermodynamic analysis, only when the concentration of solid graphitic carbon (red line in all the figures) is above zero. It should be pointed out that, according to thermodynamics, the equilibrium carbon concentration can be very small, but not zero; in our case, the threshold under which the amount of formed carbon is neglected is assumed of 10^{-5} kmol. In this situation, the line representing solid graphitic carbon collapses onto the abscissa,

and no carbon deposition is expected to take place. Figure 3.4 a) shows the results obtained for an S/C ratio equal to 1. In this case, graphitic carbon is predicted to deposit in a range of temperatures between 680 K and 1130 K. By increasing the steam to carbon ratio, the analysis based on thermodynamic equilibrium shows that the window of temperatures, where carbon deposition takes place, shrinks. This is displayed in Figure 3.4 b), where for S/C = 1.5 carbon is present in the mixture the temperature range 800-900 K, while for S/C = 2 (Figure 3.4 c)) it is not present at all. These results (in particular, Figure 3.4 a) and b)) agree with previous results published in the literature and based on a similar theoretical approach [93]. In the present work, the effect of pressure is investigated as well, and Figure 3.4 d) and e) display simulations at 7 atm, showing that, increasing pressure, the amount of carbon produced, according to the equilibrium analysis, decreases. Additional simulation results focusing only on carbon formation in the operating temperature range 600-1300 K and p = 1-7 atm, are reported in Figure 3.4 f) for the case S/C = 1.

Considering the operating range 950-1300 K in terms of temperature, and 1-7 atm in terms of pressure, the results in Figure 3.4 f) indicate that both an increase of temperature and pressure are beneficial in view of reducing carbon formation. However, this must must not be considered as a general rule, and care must be taken when extrapolating this result outside this operating window. For example,the same Figure 3.4 f) shows that, at p = 1 atm, carbon formation is enahnced by an increase of temperature in the range 670-870 K. This opposite effect of temperature is explained considering the reaction scheme (reported in Section 3.2 - Reaction Scheme), where both the SMR reaction and the MC reaction are endothermal. Thus, on the one hand, the increase of temperature shifts the endothermal MC reaction towards carbon deposition; however, on the other hand, this also favours hydrogen production from the SMR reaction, which is endothermal as well. This hydrogen production tends to shift the MC reaction to the left, i.e. unfavouring carbon deposition. As a result, the maxima in Figure 3.4 a), b), d) and f) are a trade-off between the two opposite effects of temperature described above.

Pressure might be expected to display a similar effect, since both the SMR and the MC reaction are hindered by a pressure increase, as they involve an increase in moles number; nevertheless, Figure 3.4 f) displays a continuous decrease of carbon formation, which means that the shift of the MC reaction to the left, against carbon deposition, is the prevailing effect in the range of operating conditions investigated here.

On the basis of the results presented above, it might seem possible to conclude that for a binary mixture, no carbon formation should take place with a S/C equal or higher than 2 in the typical operating range of NGSR fuel processors for SOFC systems, *i.e.* temperature 600-1300 K, and pressure 1-7 atm. Actually, some literature studies fix a value of S/C = 2 as a 'safety threshold' to avoid carbon formation under atmospheric conditions [160]. However, further results from the minimal Gibbs free energy approach pursued here, highlight that a safety criterion simply based upon the S/C value can be misleading, already on the basis of a purely thermodynamic approach. For example, considering multicomponent mixtures, Figure 3.5 a) and b) report the results obtained with two ternary mixtures CH_4 – H_2O – H_2 characterised by different compositions, but the same S/C = 1. Figure 3.5 shows that, at thermodynamic equilibrium, they lead to very different compositions and different behaviour from the carbon formation point of view (carbon formation in the 850-1050 K range in Figure 3.5 a), no carbon formation in Figure 3.5 b). In addition, these results are

different also from those already reported in Figure 3.4 a) for a binary mixture CH_4 – H_2O, again with S/C = 1.

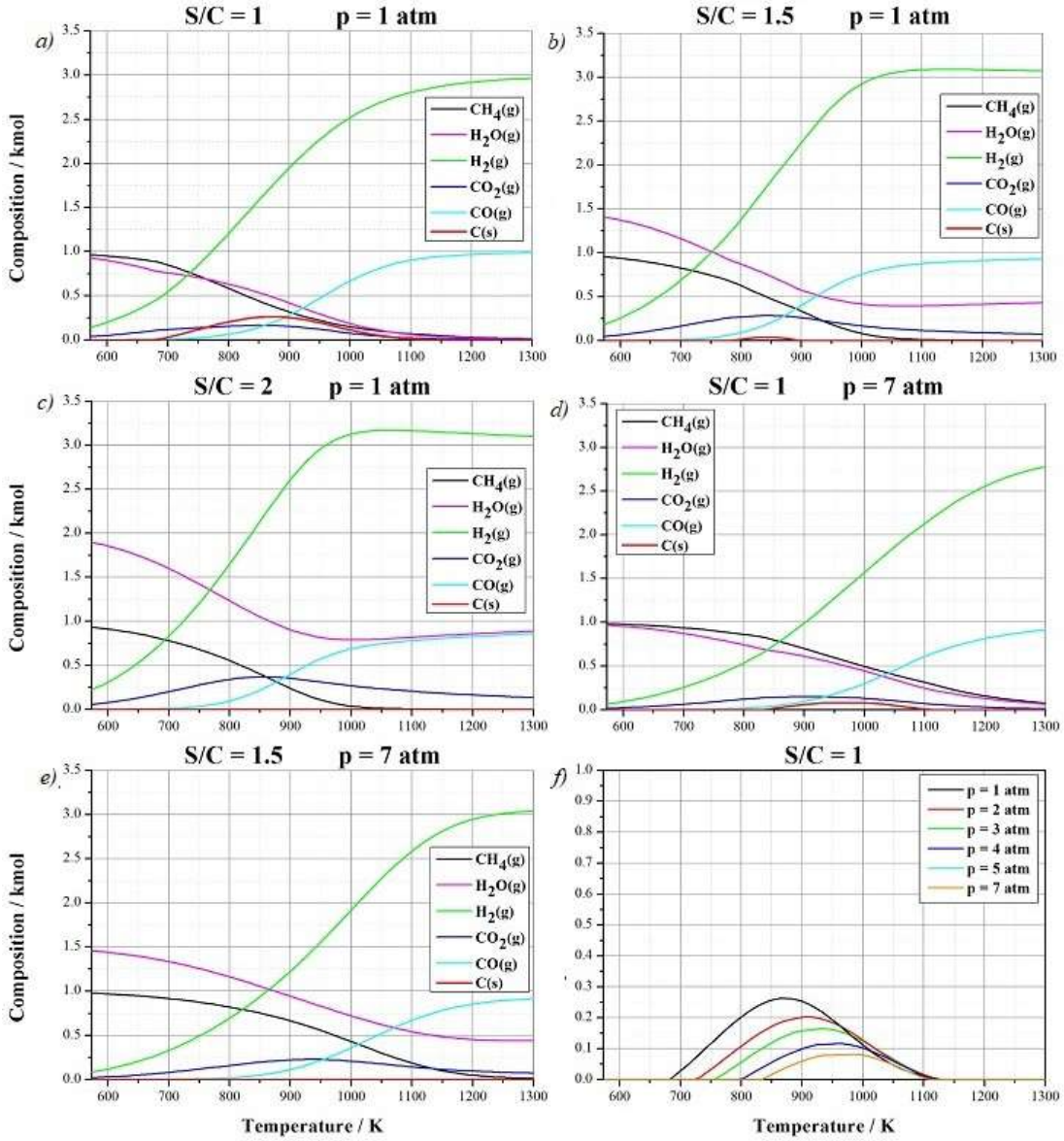

FIGURE 3.4: Equilibrium compositions calculated through the minimisation of the Gibbs free energy for CH_4–H_2O starting mixtures with different S/C ratio and at various pressures: a) S/C = 1 and p = 1 atm; b) S/C = 1.5 and p = 1 atm; c) S/C = 2 and p = 1 atm; d) S/C = 1 and p = 7 atm; e) S/C = 1.5 and p = 7 atm; f) Carbon amount for a S/C = 1 mixture and p between 1–7 atm.

While Figure 3.5 demonstrates that multicomponent mixtures with the same S/C ratio can have different behaviour from the point of view of carbon formation, also the opposite consideration holds, i.e. mixtures with different values of the S/C ratio can have exactly the same behaviour from the point of view of carbon formation, as demonstrated by a comparison between Figure 3.6 (S/C = 1) and Figure 3.4 c) (S/C = 2).

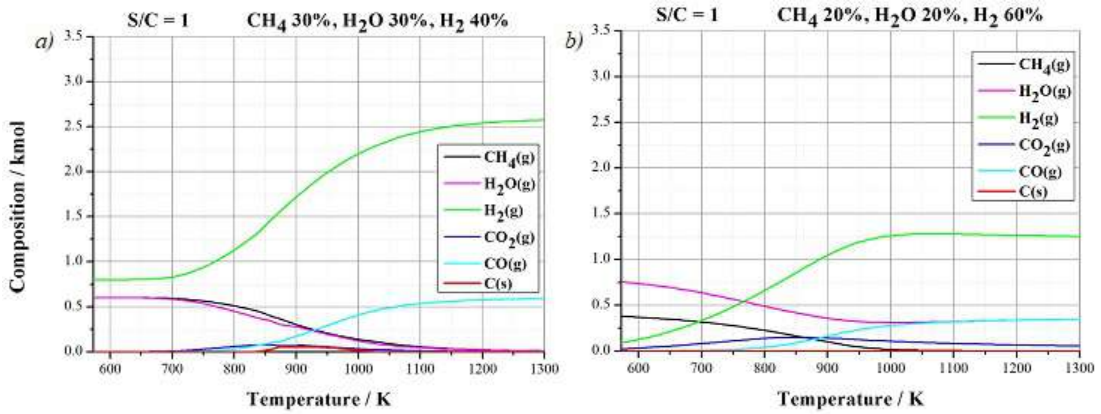

FIGURE 3.5: Equilibrium compositions calculated through the minimisation of the Gibbs free energy for various starting multicomponent mixtures at S/C = 1 and p = 1 atm: a) 30% CH_4, 30% H_2O and 40% H_2; b) 20% CH_4, 20% H_2O and 60% H_2.

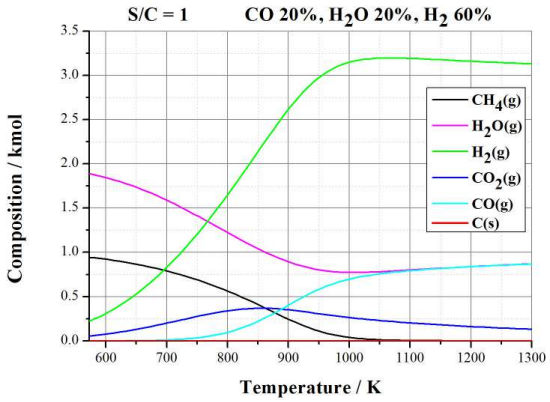

FIGURE 3.6: Equilibrium compositions calculated through the minimisation of the Gibbs free energy for a starting multicomponent mixture with S/C = 1 (20% CO, 20% H_2O and 60% H_2) and p = 1 atm.

On the basis of the thermodynamic equilibrium results reported above, it is obvious that with multicomponent mixtures (which is the case with NG) it is impossible to define a 'safety criterion' only in terms of the feedstock S/C ratio. In addition, care must be taken in appying the previous results to full-size reactor. It has already been reported by literature studies [93, 158] that carbon formation can occur in NGSR reactors even if the feedstock mixture falls inside the 'carbon free' region estimated by the thermodynamic equilibrium analysis. However, in NGSR reactors, the composition of the reacting mixture varyies along the reactor according to the reaction kinetics. Thermodynamic equilibrium can eventually occur only in the portions of the reactor close to the outlet, but everywhere else, and in particular in the portions of the reactor close to the inlet, significant deviation from equilibrium may be associated to carbon formation. Thus, a reliable investigation of carbon formation in NGSR reactors cannot be based only on a thermodynamic approach, but requires also an evaluation of

the local kinetics, as already pointed out by [93]. The results of our investigation on carbon formation based on a detailed local kinetics in the context of a complete model of an NGSR reactor, are reported in the subsequent Section 3.5.2.2 - SOFC Plant Scale NGSR Reactor.

3.5.1.2 Thermodynamic validation of the kinetic model

The kinetic model described in Section 3.4.4 - Local Kinetics, includes a number of reversible reactions, embedding the appropriate equilibrium constants K_P, whose values have been derived from the literature. The reaction rates vanish when thermodynamic equilibrium is reached. This approach for the evaluation of thermodynamic equilibrium is independent from that based on the minimization of the total Gibbs energy of the reacting mixture, also because the values of K_P, and the values of the Gibbs free energies, have been derived from different literature sources, as evidenced in the previous sections. Nevertheless, the results must coincide, and this is checked in the present Section. For this purpose, the kinetic model described in Section 3.4.4 - Local Kinetics is implemented in COMSOL as a fictitious isothermal 0-D batch reactor. The features of the 0-D batch reactor are described in Section 3.4 and in Table 3.2. In particular, the kinetic equations are implemented, together with the mass balances written under transient conditions. The simulations consist in running a time dependent simulation for a very long time (about 1000 h of simulated time) and then check if steady-state has been reached inside the reactor. The simulations have been carried out at different temperatures, pressures and S/C values. As an example, in Figure 3.7, some steady-state results are compared to the thermodynamic equilibrium results obtained by the minimization of the Gibbs free energy, demonstrating full agreement. In addition, the same results coincide with thermodynamic equilibrium data published in the literature [93]. This validates the reliability of the thermodynamic equilibrium predicted by the local kinetics model described in Section 3.4.4 - Local Kinetics, and then embedded into the NGSR complete model.

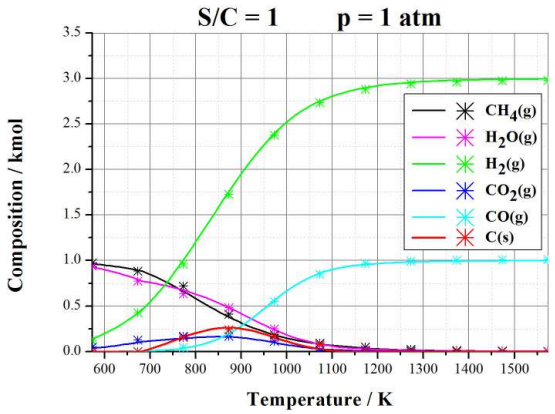

FIGURE 3.7: Equilibrium composition of a starting CH_4–H_2O mixture with S/C = 1 at p = 1 atm. Solid lines: results of the minimisation of the Gibbs free energy algorithm. Asterisks: COMSOL simulations.

3.5.2 NGSR reactor simulation

The laboratory scale and the 1.1 kW SOFC system size reactors are simulated through specific models, whose features are described in Section 3.4 and in Table 3.2. In this case, simulations are 2-D and steady-state. Model results are the distributions of all

the chemical-physical variables within the NGSR reactors, which are reported and discussed.

3.5.2.1 Laboratory scale NGSR reactor

The simulation model is applied to the laboratory NGSR reactor geometry depicted in Figure 3.2. The simulation addresses only the catalytic section of the reactor, while the glass wool holders, upstream and downstream the catalyst, are not simulated. Results are presented and discussed in comparison with reference experimental and modelling results reported in the literature for a similar laboratory reactor [55]. The main differences between the two reactors are highlighted in Table 3.8. The different catalysts employed (Ni-based in our case, Rh-based in [55]) explain the different kinetic models applied in the two cases (Table 3.8). Concerning the catalyst geometrical arrangement, in our case the catalyst is under the form of particles of about 0.2 mm diameter (further details in Section 3.3.1 - Laboratory Scale NGSR Reactor). In the case of [55], the catalyst is a honeycomb monolith, 900 cpsi (channels per square inch), hydraulic radius 0.45 mm and length 10 mm. The different geometries explain the different models adopted for the fluid dynamics (Table 3.8). In [55] [19], the channels of the honeycomb are considered to be all identical to each other, and thus only one single channel is modelled. A boundary layer model has been applied to the channel, which has a length/hydraulic radius ratio in the order of 22. The chemical reaction occurs onto the channel walls, and is treated as a model boundary condition. In our case, the features of the flow field are considered different, as it is a fixed-bed catalytic reactor with length/radius ratio is in the order of 1.7. Furthermore, a section filled with glass wool is placed upstream the reactor, in order to obtain a flat velocity profile at the entrance of the subsequent fixed-bed catalytic section. In view of this, the plug-flow assumption has been applied, and no momentum balance equations have been embedded into the model (Table 3.2). Further differences between the simulation model presented here and the reference literature work [55] regard the energy balance. As highlighted in Table 3.8, modelling and experimental results reported in [55] have been obtained in isothermal conditions. Thus, even if in our case the model includes the energy balance, nevertheless all the simulations have been run in isothermal mode (Table 3.2). The reactor feedstock composition is identical in both cases, as reported in Table 3.8.

The results obtained for conversion and selectivity are reported. Conversion and selectivity at the reactor outlet are evaluated according to the definition given by [55]:

$$X_i = \frac{\omega_{i,0} - \omega_{i,e}}{\omega_{i,0}} \tag{3.25}$$

$$X_i = \frac{x_i}{x_{CO} + x_{CO_2} + x_{CH_4}} \tag{3.26}$$

TABLE 3.8: Comparison between the NGSR laboratory reactor and related model presented in this paper, and the reference literature work [55].

	This work	**Schädel *et al.* [55]**
Catalyst	Johnson Matthey 57–4Q Ni–Al_2O_3 crunched pellets ($\sim$ 0.2 mm)	monolithic honeycomb of Rh-based catalyst
NGSR reactor model	energy balance: isothermal reactor momentum balance: plug flow reactor	energy balance: isothermal reactor momentum balance: boundary layer equations
Kinetic model	literature kinetics [99, 149, 152, 153] for SR of hydrocarbons (CH_4, C_2H_6, C_3H_8, C_4H_{10}) + WGS + MC	detailed mechanicistic studies on SR of hydrocarbons (CH_4, C_2H_6, C_3H_8, C_4H_{10}) + 765 G/S reactions
Numerical integration	FEM numerical integration through COMSOL Multiphysics	in-house developed code
Fuel composition	sulfur-free North Sea NG (86.72% CH_4, 8.10% C_2H_6, 2.03% C_3H_8, 0.44% C_4H_{10}, 1.87% CO_2, 0.84% N_2, <0.01% O_2) (mol%); S/C = 4 mixture diluted with 75% vol. He flow rate: GHSV 40 000 h^{-1} (before dilution)	

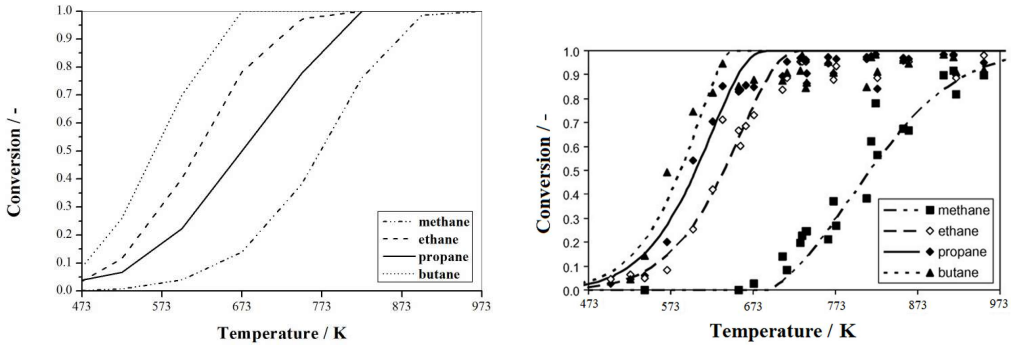

FIGURE 3.8: Methane, ethane, propane, and butane conversion as function of temperature for S/C = 4 in a laboratory scale NGSR reactor (p = 1 atm): a) results of the model presented in this paper, b) results from [55] (reproduced with permission); symbols: experiments; lines: model predictions.

Figure 3.8 reports results obtained for conversion and selectivity at S/C = 4 and in the range of temperature 473 - 973 K, demonstrating a qualitative agreement between our modelling results (Figure 83.8a) and the previous literature simulations and experimental data [55] (Figure 3.8 b). Nevertheless, some discrepancies appear as well. For example, the literature model and experimental data demonstrate that, with the Rh-based catalyst, hydrocarbon conversion has different features in two different temperature operating ranges, delimited by the value T = 670 K. Indeed, below that threshold temperature, no SMR occurs, while the SR of all the higher hydrocarbons (ESR, PSR and BSR) proceed almost simultaneously. More in detail, the previous literature model [55] predicts that, increasing the reactor operating temperature, C_4H_{10} is converted first, followed by C_3H_8, C_2H_6. In practice, ESR, PSR and BSR reactions are all complete around 670 K, where SMR conversion starts. Our model, developed for a Ni-based catalyst, predicts that the conversion of the higher hydrocarbons occurs before that of methane, without a visible sharp split. Another difference related to the different catalysts employed, and thus to the different kinetic models, is that the order of the conversion of higher hydrocarbons is different. In our case, C_4H_{10} is converted first again, but it is followed by C_2H_6 and then by C_3H_8. Finally, a further remark about Figure 3.8 a) is that the conversions of the higher hydrocarbons do not follow strictly the order of their activation energies (75.73 kJ mol^{-1} for ESR, 42.5 kJ mol^{-1} for PSR and 77.82 kJ mol^{-1} for BSR, from Tables 3.3 and 3.4). This is due to the fact that ESR, PSR and BSR have activation energies quite similar to each other, and thus other factors modify the order, in particular the different kinetic expressions adopted and the values of the other kinetic parameters, all derived from the literature and specific for Ni-based catalysts. Nevertheless, in spite of the differences, there are also several similarities between Figure 3.8 a) and b), and in particular both simulation models predict practically identical temperature-dependent behaviour of ESR and BSR conversion.

In Figure 3.9, detailed contour maps of molar fractions inside the reactor, obtained from our simulation model run in isothermal mode at 850 K (Figure 3.9 a), are compared to the reference literature simulation results [55] (Figure 3.9 b). We recall that in our case the whole fixed-bed reactor is simulated (radius 3×10^{-3} m), while in [55] one single channel of the honeycomb structure is simulated (hydraulic radius 4.5×10^{-4} m), which explains the mismatch of the radial coordinates in Figure 3.9. The molar fraction profiles retrieved from [55] display a clear deviation from the plug-flow behaviour. Indeed, in an isothermal simulation, the only reason for the visibly bending

iso-concentration profiles is due to the velocity profiles. In our results, this effect is not observable due to the plug-flow assumption made in developing the simulation model.

An analysis of the concentration maps of ethane and butane highlights practically complete agreement between the two simulations. In particular, the consumption of these reactants is calculated to be practically complete at the outlet of the reactor, with both simulations. This good agreement is in accordance with the results reported in Figure 3.8, which display that both simulation models predict practically identical temperature-dependent behaviour of ESR conversion; the same hold also for BSR conversion. On the contrary, our simulated map of propane molar fraction displays higher concentration values than those reported by [55], in particular at the outlet of the reactor, and this is also in agreement with the results reported in Figure 3.8, which display that the literature reference model predicts the PSR reaction to achieve complete conversion at about 670 K, versus 800 K in our model. Concerning methane, Figure 3.8 displays that our model predicts higher conversion, and indeed this is visible also in the concentration maps of Figure 3.9. Concerning the other components of the gaseous flow, hydrogen and carbon dioxide maps are again very similar to each other. Differences are more remarkable for CO, which is our case undergoes visible formation in the first 2 mm of the reactor, where a maximum is reached. Afterwards, CO is consumed by the WGS reaction, until a value of 0.5% is reached at the reactor outlet. On the contrary, the results retrieved from [55] show a continuous increase of CO molar fraction, until a value of 0.55% is reached at the reactor outlet.

For water, the inlet molar fraction is 20.3%, and it continuously decreases along the reactor due to the consumption of the SR reactions. The outlet molar fraction is 11.6% with our model, and 11.7% with the literature reference model. In Figure 3.9, for a better results visualization of the results obtained for H_2O, the bottom of the colour scale is 0 in the left hand panel, and it is 0.117 in the right hand panel.

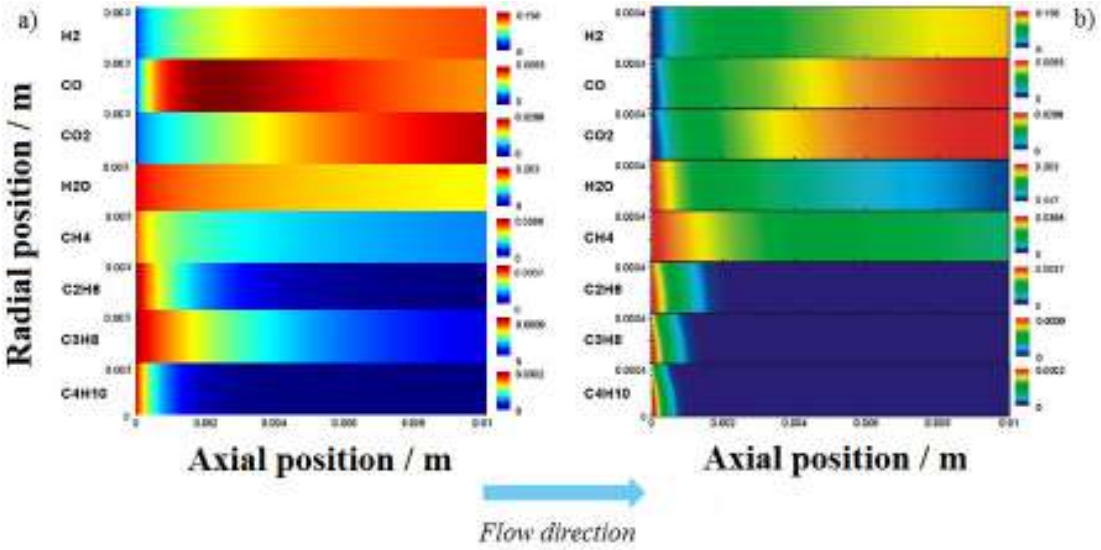

FIGURE 3.9: Maps of species mole fractions in the laboratory scale NGSR reactor at 850 K, S/C = 4 (p = 1 atm): a) results of the model presented in this paper, b) modeling results from [55] (reproduced with permission). For H_2O, for better results visualization, the bottom of the color scale is 0 in the left hand panel, and it is 0.117 in the right hand panel.

Based on our detailed analysis, we can state that the comparison between our model and the reference literature model [55] demonstrates overall qualitative agreement, and also quantitative agreement in several aspects.

3.5.2.2 SOFC plant scale NGSR reactor

Results obtained when applying the simulation model to an NGSR reactor developed for a 1.1 kW SOFC system (reactor scheme in Figure 3.3) are reported. The model is steady state and includes the local mass balance, the local energy balance and also the momentum balance under the form of Darcy's law (Table 3.2). The operating conditions, derived from previous SOFC system simulations [91], are as follows: operating pressure 1 atm, fuel flow rate 2×10^{-3} m^3 min^{-1} (referred to normal conditions: 1 atm, 273.15 K); fuel composition 90% methane, 10% hydrogen. The fuel is then mixed with steam (S/C = 2), and fed into the reactor with an inlet temperature 844 K. In order to keep the reactor at the desired temperature, 0.16 kW electrical power is considered to be supplied to the external heating jacket.

Figure 3.10 reports the simulated temperature map. The first remark is that, in this case, a deviation from the plug-flow behaviour of the reactor is clearly visible, with clearly visible profiles of temperature which are due to both the velocity field and the energy transport from the heated wall towards the reactor centre, obviously colder due to the development of the endothermal SMR reactions. Along the flow direction, the reacting mixture, after entering the reactor at 844 K, quickly cools down to about 837 K after 2 cm, again due to the endothermal effect of the fast SMR reactions. Then, the reactions kinetics slows down, the heat transfer through the external walls becomes the prevailing effect, and the temperature of the reacting mixture raises up to a value of about 910 K at the reactor outlet. The temperature operating range of the reactor is in line with that previously reported for a simulated fuel processor embedded into an SOFC system [91].

Carbon molar fraction is reported in Figure 3.11. Even if thermodynamic considerations lead to the general assumption that a S/C = 2 is safe for coke free operation in SOFC systems, as previously discussed in Section 3.5.1.1 - Evaluation of Carbon Formation on the Basis of the Minimal Gibbs Free Energy Approach, in Figure 3.11 it is possible to spot the formation of carbon in the first 7-8 millimetres after the reactor entrance. In Figure 3.11, the presence of carbon is visualized if its molar fraction exceeds the threshold value of 6.9×10^{-5}; the maximum percentage value is 1.18%. The explanation for the presence of carbon is based on the combined effect of thermodynamics and kinetics. For a better understanding, the kinetic rates evaluated by the model are reported in Figure 3.12.

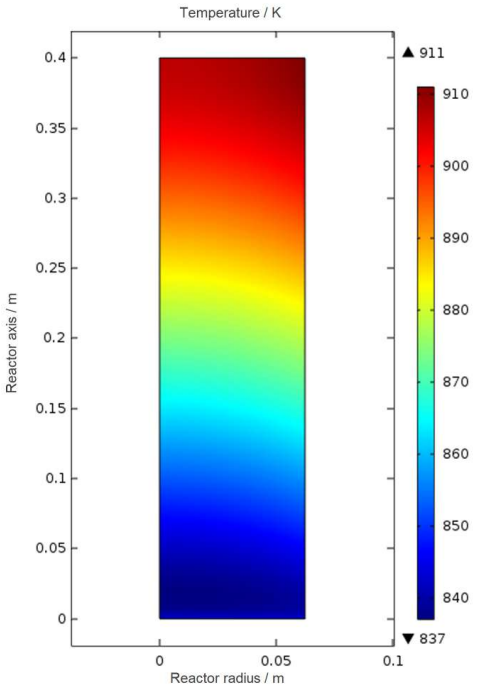

FIGURE 3.10: NGSR reactor for 1.1 kW SOFC system applications, p = 1 atm and S/C=2. Simulation results: temperature map.

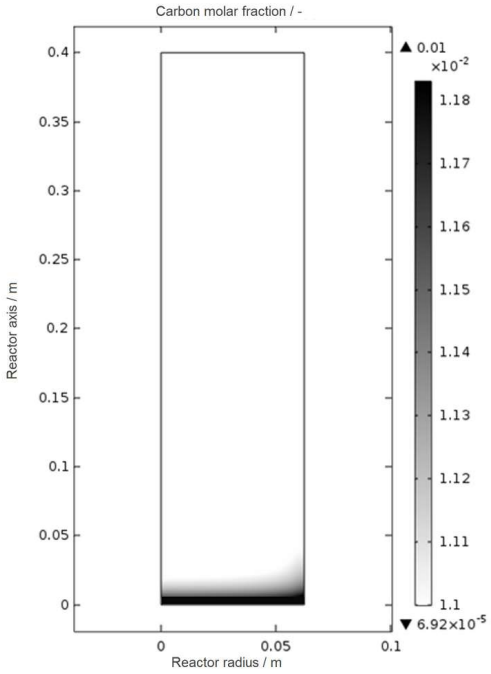

FIGURE 3.11: NGSR reactor for 1.1 kW SOFC system applications, p = 1 atm and S/C=2. Simulation results: carbon mole fraction.

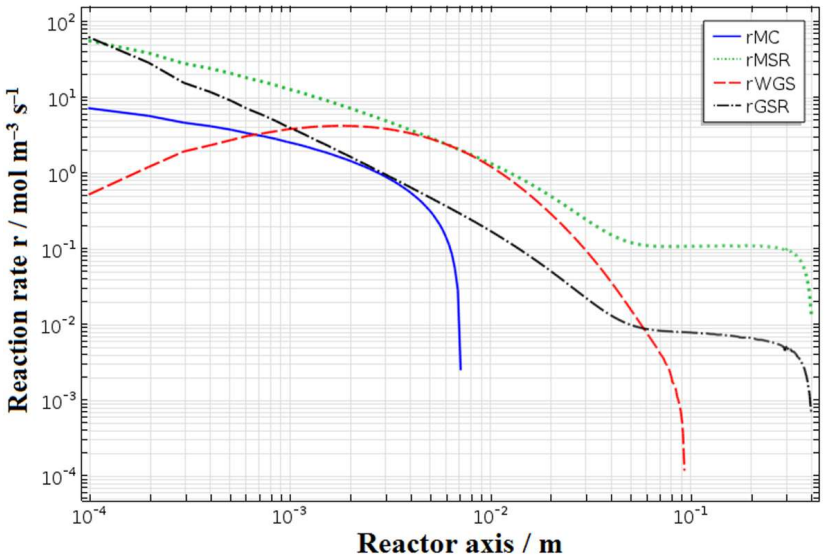

FIGURE 3.12: NGSR reactor for 1.1 kW SOFC system applications, p = 1 atm and S/C=2. Simulation results: reaction rates for SMR (= MSR), WGS, GSR and MC along the reactor axis.

Figure 3.13 reports molar fractions along the axis of the reactor, displaying CH_4 and H_2O consumption occurring together with H_2 and CO and CO_2 production. At the reactor entrance, the molar fraction is high for methane and small for hydrogen (Figure 3.13 11), and thus there is thermodynamic driving force driving the MC reaction towards the right hand side, *i.e.* carbon formation, as confirmed by the high value or the reaction rate r_{MC} reported in Figure 3.12. Simultaneously, due to the SMR, WGS and GSR reactions, with fast kinetics at the reactor entrance (displayed again in Figure 3.12), the amount of hydrogen increases significantly. This, after the first 7-8 mm, reduces to zero the thermodynamic driving force for further MC and coke formation. Indeed, Figure 3.12 shows that after the first 7-8 mm r_{MC} drops to 2×10^{-3} mol m^{-3} s^{-1} and thus, no more carbon formation is detected in the reactor. In particular, no carbon formation is displayed at the reactor outlet, where all the reaction rates have values as low as 10^{-3} mol m^{-3} s^{-1}, the composition is at thermodynamic equilibrium and collapses with that reported in Figure 3.4 c) at a temperature of 910 K.

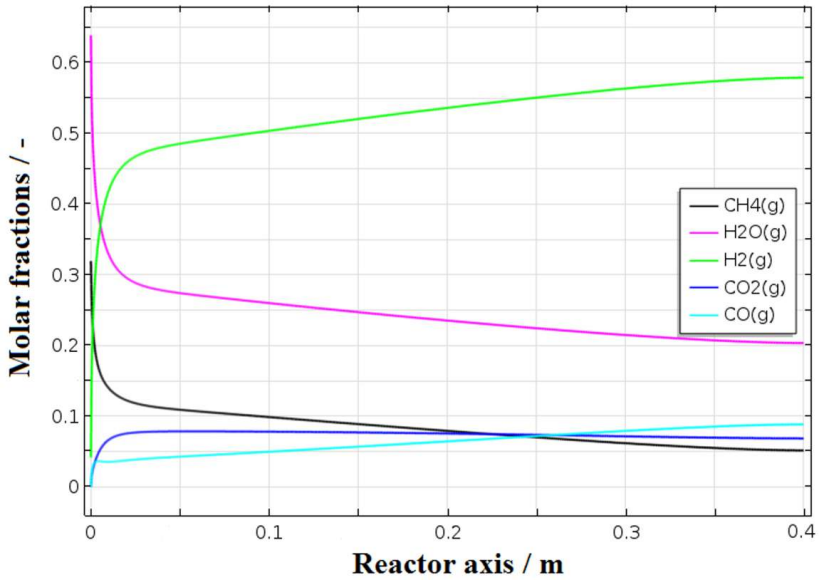

FIGURE 3.13: NGSR reactor for 1.1 kW SOFC system applications, p = 1 atm and S/C=2. Simulation results: composition profiles along the reactor axis.

Generally speaking, on the basis of previous thermodynamic investigations [93] recalled and discussed in Section 3.5.1.1 - Evaluation of Carbon Formation on the Basis of the Minimal Gibbs Free Energy Approach, carbon deposition is expected to reduce by increasing the S/C ratio. Our reactor simulations confirm this result, as displayed in Table 3.9, which reports the thickness of the carbon deposition area in the reactor as a function of the S/C parameter. Indeed, an increase of the S/C ratio results in: (i) reduction of methane mole fraction, (ii) increase of the water mole fraction, leading to faster WGS reaction and hydrogen production. Further simulation (not reported here) show that the effect (ii) is practically negligible, while effect (i) dominates, resulting in a reduction of the thermodynamic driving force for the MC reaction towards the right hand side, and thus towards reduced carbon formation.

Even if the extension of carbon formation is predicted to be narrow, below 7-8 mm in the simulations presented above, nevertheless, according to previous literature works [153, 154] carbon is expected to deposit and progressively clog the catalyst active sites, inhibiting the catalytic activity and shifting all the reaction downwards the reactor.

TABLE 3.9: NGSR reactor for SOFC scale applications, p=1 atm. Simulated results of carbon extension as a function of S/C.

S/C ratio	**C extension** [mm]
2	7.3
3	5.4
4	4.6

Thus, the area of carbon formation identified in Figure 3.11 is expected to extend during time, reducing the performance of the reactor, which eventually releases a significant amount of unreacted methane.

3.6 Conclusion and future developments

In solid oxide fuel cell (SOFC) plants, failure of the fuel processor can result in increased levels of methane being fed into the fuel cell stack, with possible consequent damage. In view of this, diagnostics of the fuel processor through fault detection and isolation (FDI) tools, and possibly also prognostics, are of utmost importance.

We are developing methods for early prediction and detection of faults in chemical reactors based on numerical tools for the steady-state and transient reactor simulation. In this paper, we present a model for a tubular NGSR reactor, developed including a detailed local kinetics for the main reactions occurring in a mixture of natural gas and steam, fed into a tubular fixed-bed reactor with Ni based catalyst. The model includes mass, energy and momentum balances, coupled to appropriate boundary conditions, and it is integrated through an FEM method through the COMSOL Multiphysics software. The model is applied to a laboratory scale reactor and also to a typical reactor for application in a 1.1 kW SOFC systems.

The results obtained can be summed up as follows: (i) the model allows the evaluation of 2-D maps of temperature, compositions and reaction rates in tubular NGSR reactors in steady-state conditions; (ii) the model simulates healthy and faulty operation due to carbon formation; (iii) the model is validated against reference literature results [19] for a laboratory size NGSR reactor; (iv) simulation results for an NGSR fuel processor for a 1.1 kW SOFC system are presented, showing that safety criteria based on the feedstock S/C ratio are demonstrated to fail in a number of operating conditions.

Future developments for this work are planned in terms of: (i) refinement of kinetic parameters and further model validation on the basis of experimental data provided by in-house laboratory-scale reactor (DICCA Catalysis Lab, University of Genoa); and (ii) use of simulated temperature and composition results under faulty and unfaulty operating conditions to produce data to train diagnostic and prognostic tools, specific for the fuel processor of an SOFC power plant.

Chapter 4

Experimental Analysis of End-of-Life Commercial Catalyst from a Full-Scale Industrial SMR Reactor

Even if the SMR process implements an old and well known technology, it involves the risk of carbon formation, which may cause serious operational problems. Carbon may be formed via different routes, each influencing the morphology of the carbon. The most common types are (i) whisker-like, (ii) encapsulating, and (iii) pyrolytic carbon. In this chapter an experimental investigation on the different carbon morphologies, which can be found over industrial SMR catalyst, is proposed.

4.1 Introduction

Carbon is formed by dissociation of CO, CH_4 and higher hydrocarbons over metal particles [161]. In particular, C whiskers typically grow as a carbon fiber with a metal crystal at the top [162]. Whisker carbon is an important phenomenon in the process industry since the whisker has high strength and destroys the catalyst particle when it hits the pore wall. In a tubular NG reformer broken catalyst pellets and carbon may have a serious impact on the operation of the reformer by maldistribution of feed and overheating of the tubes [162]. Whisker carbon may also be formed in other processes (*i.e.* methanation for synthetic natural gas or Fischer–Tropsch synthesis [162]) and be involved in coking of tube walls in steam crackers [96] and in nucleation of metal dusting corrosion [163]. The so-called carbon nanotubes and other carbon-based nanofiber structures are also considered for a variety of nanotechnological applications including the use as catalyst support [161].

4.2 Experimental analysis

4.2.1 Catalyst samples

During one of the periodic shut down of the IPLOM S.p.A. refinery, samples of the Johnson-Matthey catalysts for steam reforming have been collected. The steam reforming furnace of IPLOM (unit F-1801) is constituted by 52 tubes each filled by:

- KATALCO 57-4Q, for the first half of the reactor
- KATALCO 25-4Q, in the second part of the reactor

The two catalyst are both NiO supported on calcium aluminate ($CaAl_2O_4$) with the second being a lightly alkalized (K_2O addition) version of the first one [18].

In Figure 4.1 a schematic view of the Johnson-Matthey catalyst contained in the reactor is displayed. The figure allows the identification of the catalyst peculiar shape, technically called *quadralobe*. Furthermore, in Figure 4.1 are also illustrated the catalyst sampling points.

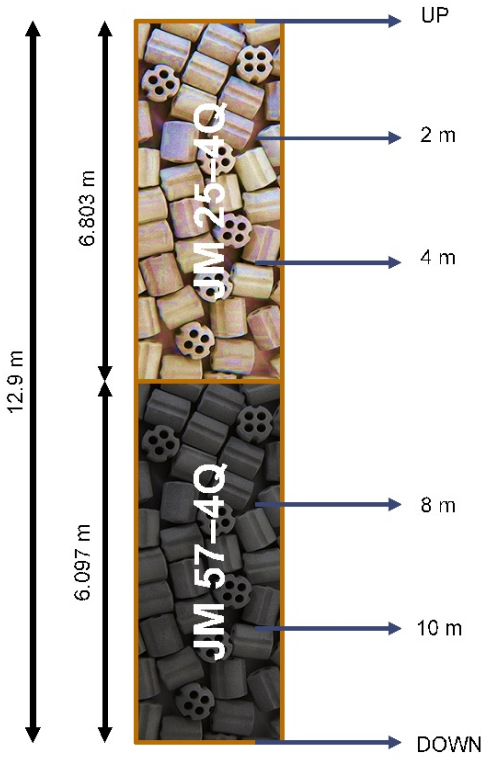

FIGURE 4.1: Catalyst sampling points.

The catalyst has been in use for 7 years and it has been carefully taken out from the tubes, to avoid its damage.

From internal temperature-monitoring sheets, it is possible to determine the mean temperature of the tubes. The catalyst samples come from two different tubes which have been chosen considering their average temperature. The temperature measurements (data collected by IPLOM from 5th January to 19th April, 2018) allowed to state that tube 4 has the lower average temperature while tube 42 has the higher average temperature.

In Figure 4.2 are reported the average temperature values of the two tubes. The mean value (calculated over the time interval) for tube 4 is around 1072 K, while for tube 42 is around 1082 K.

The catalyst pellets are prepared cutting longitudinally to expose the inside of the pellet itself and directly placed into the SEM microscope after glueing them on the support using carbon tape.

4.2.2 Analytical technique: SEM & EDS

A scanning electron microscope (SEM) (TM 3000, Hitachi) is a type of electron microscope that produces images of a sample by scanning the surface with a focused

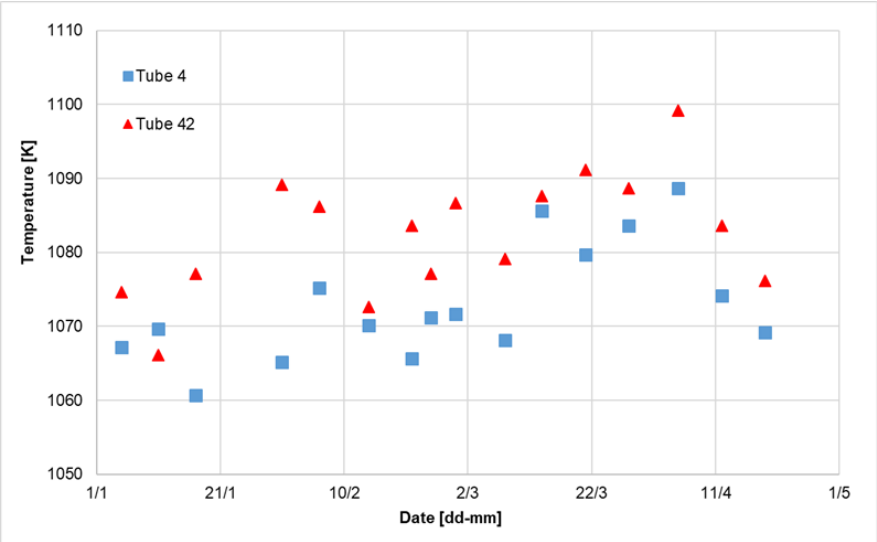

FIGURE 4.2: Average temperature for tubes 4 and 42.

beam of electrons. The electrons interact with atoms in the sample, producing various signals that contain information about the surface topography and composition of the sample. The most common SEM mode is the detection of secondary electrons emitted by atoms excited by the electron beam by scanning the sample and collecting the secondary electrons that are emitted using a special detector. Thus, an image displaying the topography of the surface is created.

Energy-dispersive X-ray spectroscopy (EDS, or EDX) (Quantax 70, Bruker Nano GmbH) is an analytical technique used for the elemental analysis or chemical characterization of a sample. It relies on the interaction of some source of X-ray excitation and a sample. Furthermore, its characterization capabilities are due in large part to the fundamental principle that each element has a unique atomic structure allowing a unique set of peaks on its electromagnetic emission spectrum. In particular, when available, the elemental distributions of Ni, K, C, Ca or Al are illustrated.

4.3 SEM & EDS results

In the following sections are reported some SEM and EDS images useful for the discussion. Each sample is labelled with the tube number (see Section 4.2.1) and its position according to Figure 4.1.

4.3.1 Tube 4

At the very beginning of the reactor, the SEM image (Figure 4.3) points out that carbon seems to deposit into the larger pores covering their internal surface, leading to their clogging. The main probable reason for this behavior is that inside the larger pores there is a higher mass flux (*i.e.* more reagents pass through them). The equilibrium of reactions 1.6 and 1.7 is shifted towards the carbon side both for the higher reagent flux (in particular methane) and the relatively low amount of hydrogen coming with the feedstock. In addition to this, the small quantity of H_2 prevents eventual gasification of C, which is also inhibited by the C filling and, probably, closing the pores.

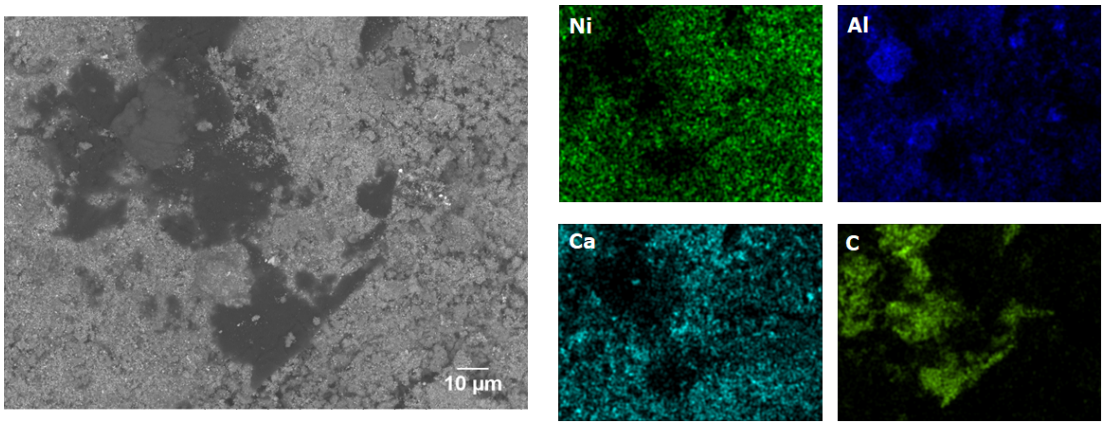

FIGURE 4.3: (left) SEM micrograph and (right) EDS elemental analysis of the catalyst in Tube 4 – Position UP.

At about 2 m, the SEM image shows a filamentous structure (Figure 4.4). According to the EDS analysis this structure is mainly composed by Ca (Al is not displayed here, but it is substantially equal to the Ca EDS image) and a finer dispersion of C particles. This agglomerate can be identified as the catalyst support, being mainly composed by $CaAl_2O_3$. The carbon here is deposited in form of finer particles all over the support, revealing a probable nature of pyrolytic carbon.

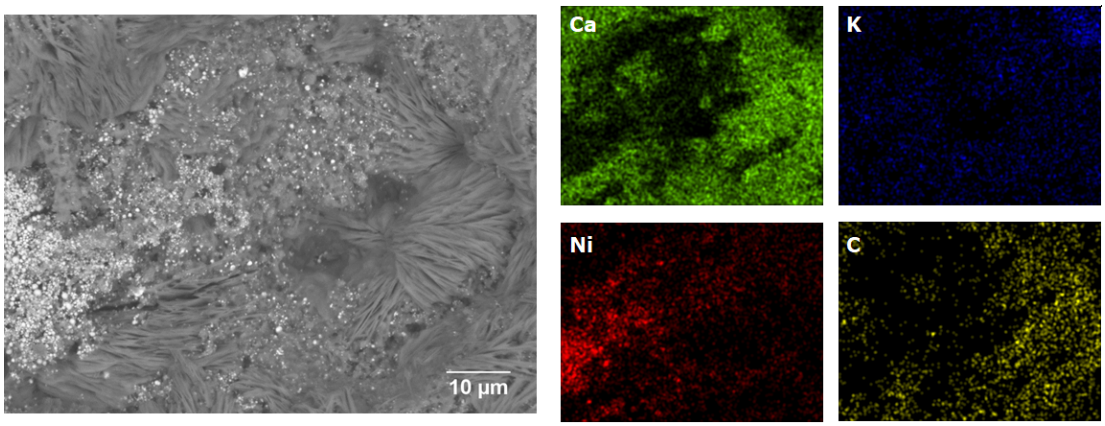

FIGURE 4.4: (left) SEM micrograph and (right) EDS elemental analysis of the catalyst in Tube 4 – Position 2 m.

Further down in the reactor (Figures 4.5 and 4.6), an interesting phenomena can be highlighted. In both cases, a presence of Fe and Cr is revealed. Their presence can be explained by the solid-state diffusion of the main components of the chromium/nickel steel alloy, which deposits onto the catalyst. This deposition can be due to the temperature gradient inside the reformer tube: the tube wall experiences a high temperature being in "direct" contact with the flame inside the furnace, while the catalyst inside the tube is at a lower temperature because the low thermal conductivity of the ceramic support. Another possible explanation is related to the growth of carbon whiskers on the tube wall causing a detachment of Fe and Cr atoms from the steel alloy [164]. However, in this section no carbon is retrieved.

Going down along the reactor, another filamentous structure in the catalyst is retrieved (Figure 4.7). It looks similar to the one found in the same tube in Position 2 m (Figure 4.4), but the filaments constituting this structure have a bigger length and

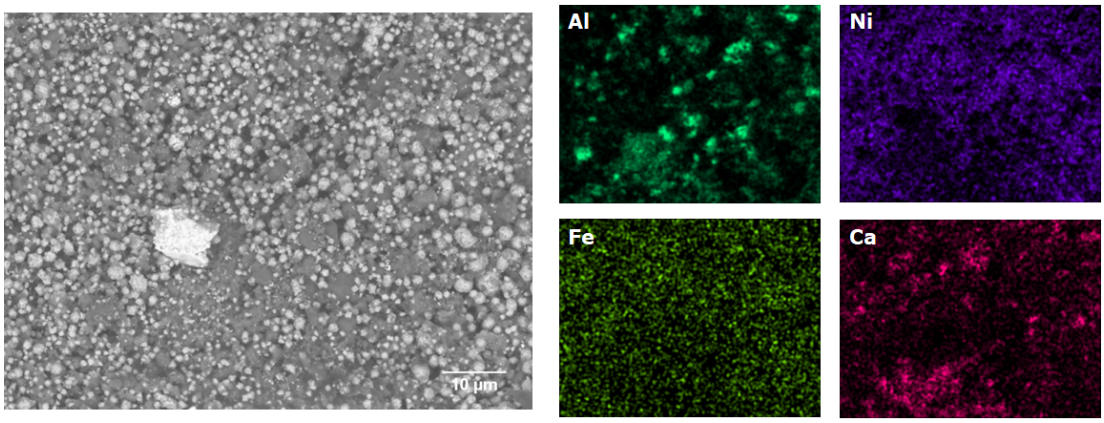

FIGURE 4.5: (left) SEM micrograph and (right) EDS elemental analysis of the catalyst in Tube 4 – Position 4 m.

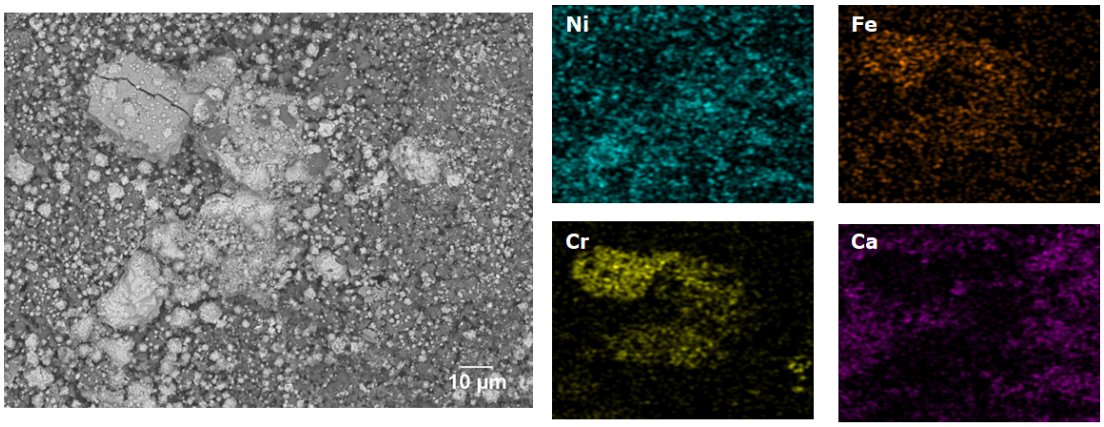

FIGURE 4.6: (left) SEM micrograph and (right) EDS elemental analysis of the catalyst in Tube 4 – Position 8 m.

diameter. However, also in this case the same hypothesis for concluding that this filamentous structure is the catalyst support holds. In addition, at this location inside the tube, carbon is present again. It looks finely dispersed in correspondence of the Ni particles, leading us to suppose C being in the form of nanotubes.

In the last part of the tube, C is found again (Figure 4.8). It is finely dispersed onto the catalyst in correspondence of the Ni particles. Carbon presence can be explained by the higher temperature at the tube outlet, which promotes the kinetic of methane decomposition (reaction 1.6).

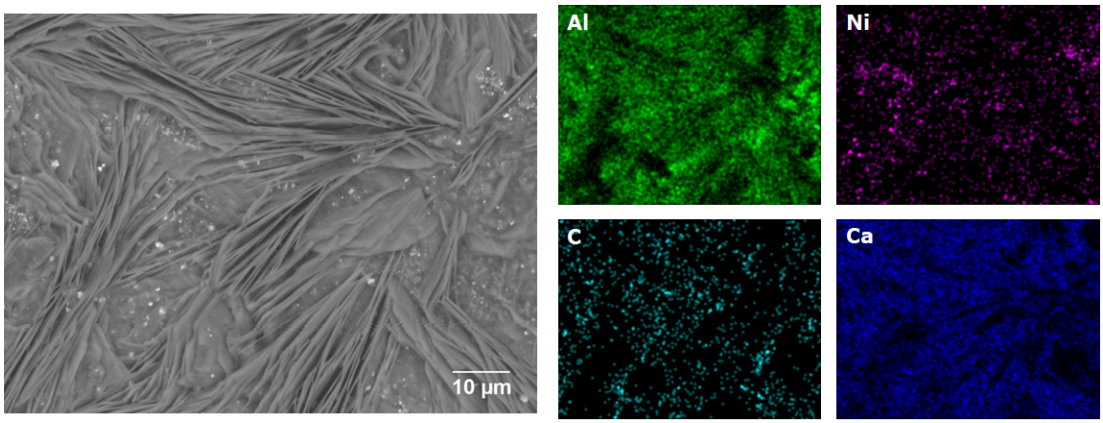

FIGURE 4.7: (left) SEM micrograph and (right) EDS elemental analysis of the catalyst in Tube 4 – Position 10 m.

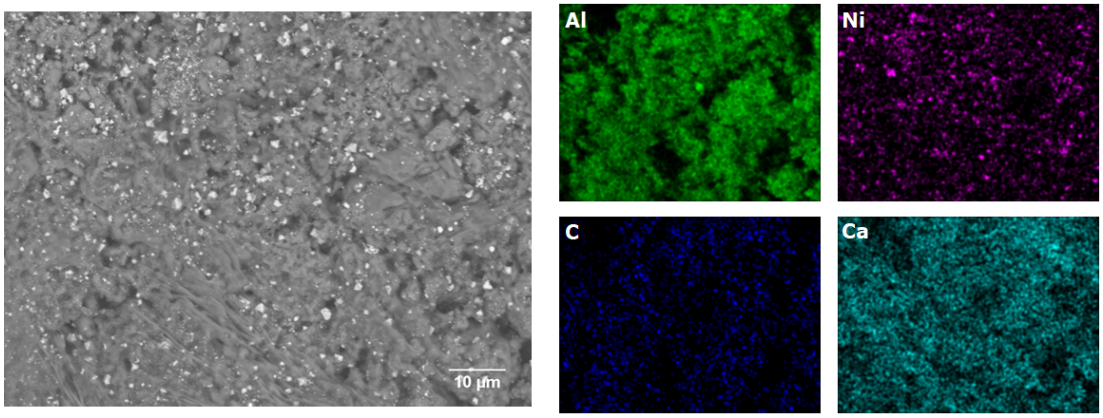

FIGURE 4.8: (left) SEM micrograph and (right) EDS elemental analysis of the catalyst in Tube 4 – Position DOWN.

4.3.2 Tube 42

In the first section of the second tube, the SEM image (Figure 4.9) shows a highly porous structure with a large grain in the middle of the micrograph. This formation is supposed to be Ni and our assumption is confirmed by the corresponding EDS image. In this section, it is possible to spot the presence of carbon finely dispersed. In particular, from Figure 4.9, C accumulates mainly in correspondence of the Ni particle, as it has been described in Section 1.2.3.1.

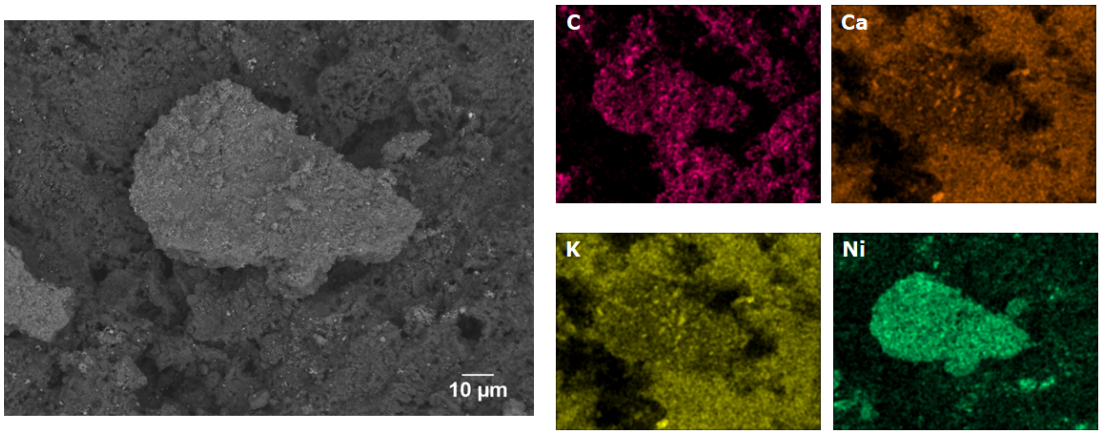

FIGURE 4.9: (left) SEM micrograph and (right) EDS elemental analysis of the catalyst in Tube 42 – Position UP.

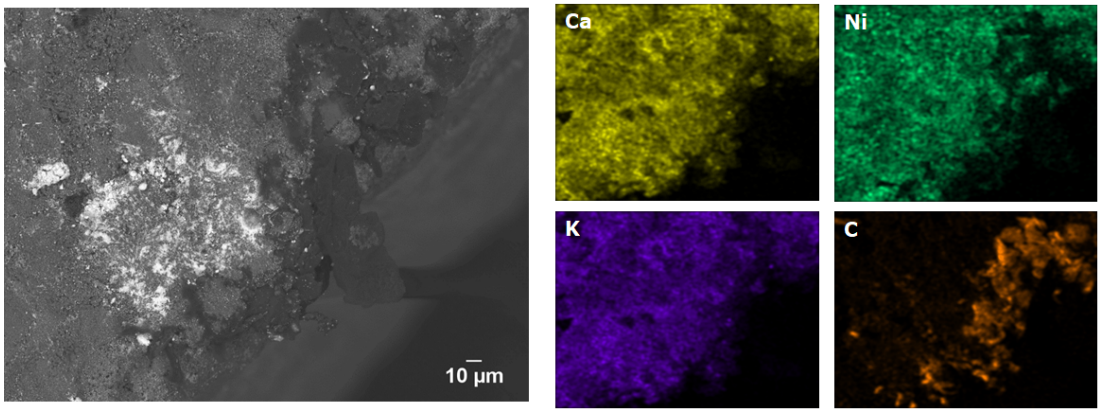

FIGURE 4.10: (left) SEM micrograph and (right) EDS elemental analysis of the catalyst in Tube 42 – Position 2 m.

Moving down in the reactor is possible to spot the presence of an agglomerate (Figure 4.10) which is mainly composed of Ni. This is confirmed by the EDS image. At the corner of the catalyst, C is retrieved. In particular, a comparison between the SEM image and the EDS C map permits to visualize a dendritic structure emerging from the catalyst side.

At about 4 m down in the reactor, the SEM image (Figure 4.11) reveals an almost homogeneous structure with finely dispersed Ni and K particles. In addition, a fine particulate of carbon is retrieved leading to the hypothesis of pyrolytic carbon formation.

In the second part of the reactor (*i.e.* after the catalyst change), the SEM image (Figure 4.12) highlights the presence of a large white structure which, according to the

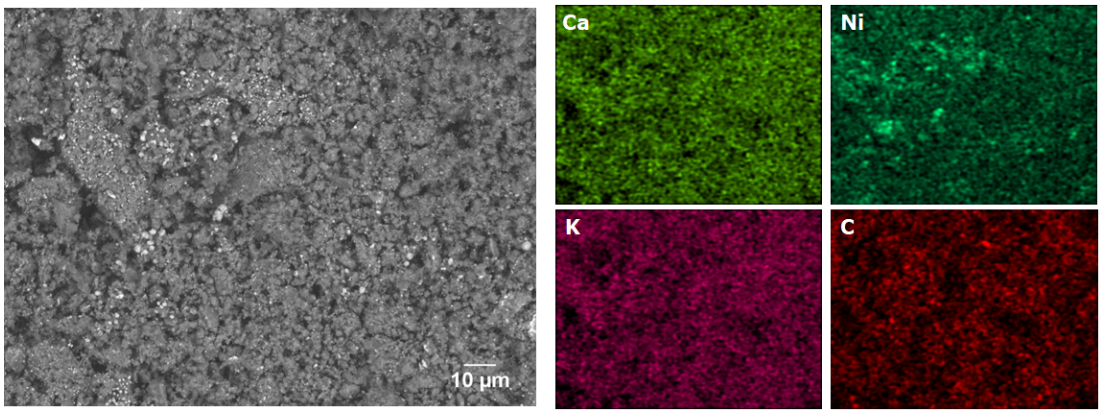

FIGURE 4.11: (left) SEM micrograph and (right) EDS elemental analysis of the catalyst in Tube 42 – Position 4 m.

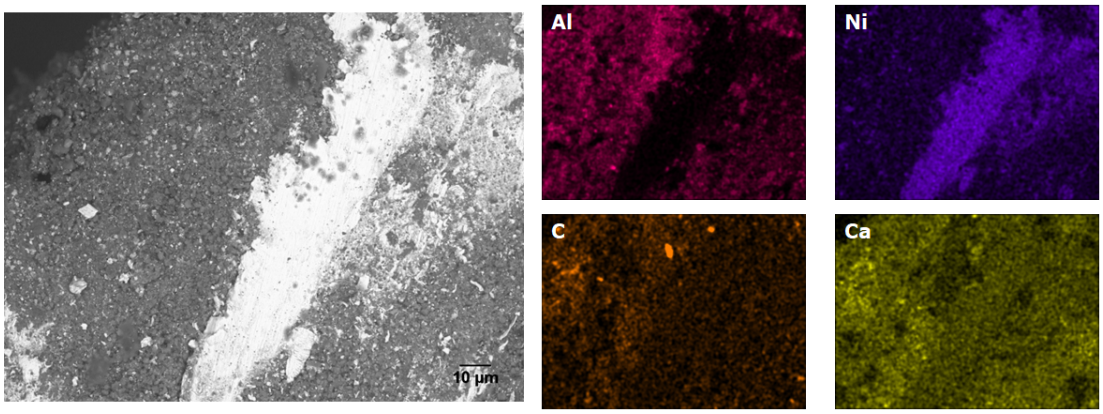

FIGURE 4.12: (left) SEM micrograph and (right) EDS elemental analysis of the catalyst in Tube 42 – Position 8 m.

EDS analysis, is a Ni agglomerate. Furthermore, from Figure **17(b)**, a diffused carbon presence is highlighted.

In the last section of the reactor (*i.e.* at 10 m from the top), the SEM image (Figure 4.13) reveals the presence of a worm-like structure. The composition of this structure could be a mixture of C and Ni, according to the EDS images.

At the very bottom for the reactor (Position DOWN), the SEM micrograph (Figure 4.14) reveals the presence of large particles made of Ni. Furthermore, a diffuse and finely dispersed presence of carbon is detected.

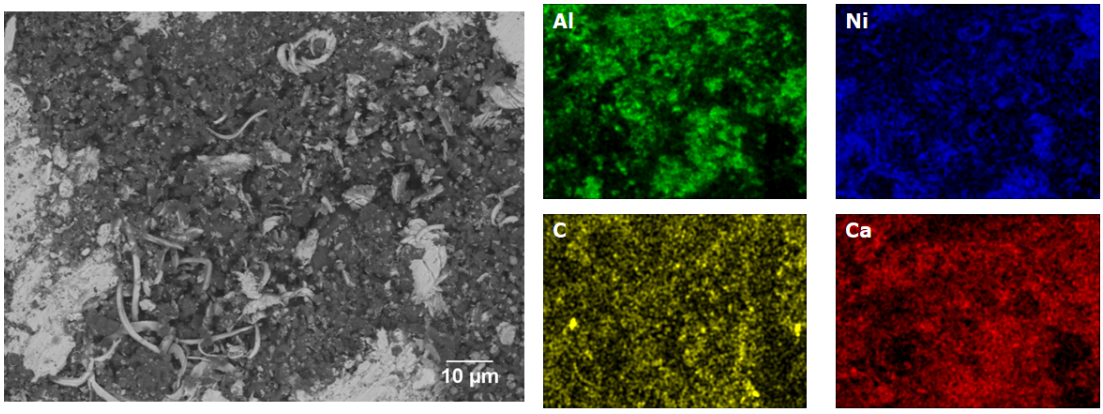

FIGURE 4.13: (left) SEM micrograph and (right) EDS elemental analysis of the catalyst in Tube 42 – Position 10 m.

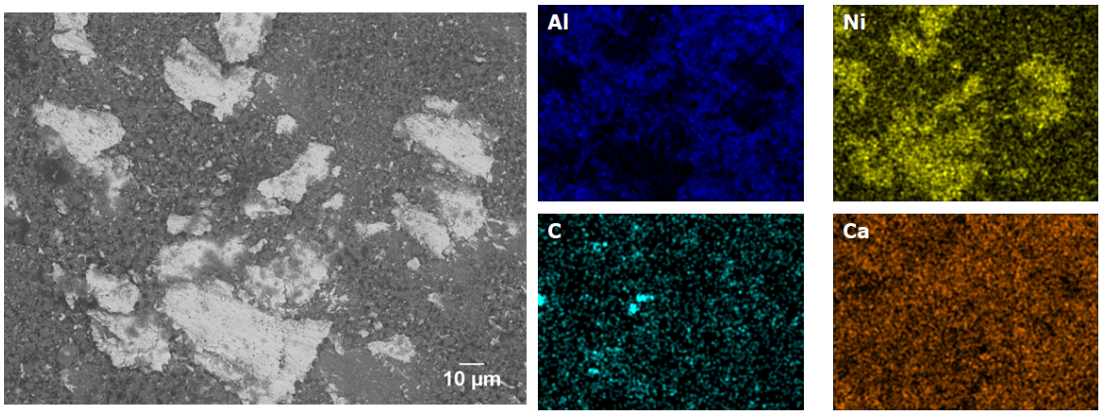

FIGURE 4.14: (left) SEM micrograph and (right) EDS elemental analysis of the catalyst in Tube 42 – Position DOWN.

4.3.3 Comparative analysis

To gain a deeper understanding of the SEM results, it is interesting to compare the images for both tubes at the same position (i.e. Position UP for Tube 4 and 42, Position 2 m for Tube 4 and 42, etc.).

Considering the catalyst near the tube inlet, the SEM images show a diffused presence of carbonaceous deposits as confirmed by the corresponding EDS images. Here carbon sits mainly in the larger pores which have an average dimension of 1 µm. In addition, according to the classification of carbon deposits (see Section 1.2.3.1), carbon could be in the polymeric (or gum) form. These deposits lead to pore blocking and consequently to the inability of further gasification processes. These consideration seems to hold for the catalyst in Position 2 m, as well.

Moving down in the reactor, carbon morphology starts to change and from the pyrolytic we have the whisker form. These whiskers begin to be formed on the Ni grain and continue to grow leading to the detachment of the Ni particles from the support. Furthermore, during the shutdown, water vapour is flowed inside the tube in order to reduce its temperature. This procedure can lead to the expansion of the C whiskers which consequently detach the Ni particles where C is formed. So the support is left completely uncovered by Ni (as it can be seen at the tube outlet (Position DOWN)).

A possible explanation of the different kind of carbon deposition is related both to the temperature profile in the tubes and to the feedstock composition.

Table 4.1 reports the typical feedstock composition and temperature. The reforming reactor is fed by two different gaseous flow: natural gas (NG) coming from the Italian national gas grid, and refinery gas (RG) coming from other unit operations in the refinery. The table highlights the presence of significant amount of CH_4 and higher hydrocarbon in the mixture.

TABLE 4.1: Typical composition and temperature of the reformer feed at IPLOM refinery.

Variable	Value	Units
Flow Rate	1411.47	$kg\,h^{-1}$
x_{CH_4}	15.22	%mol
$x_{C_2H_6}$	0.94	%mol
$x_{C_3H_8}$	0.63	%mol
$x_{i-C_4H_{10}}$	0.12	%mol
$x_{n-C_4H_{10}}$	0.28	%mol
$x_{i-C_5H_{12}}$	0.03	%mol
$x_{n-C_5H_{12}}$	0.01	%mol
x_{C_6}	0.04	%mol
x_{CO}	-	%mol
x_{CO_2}	0.08	%mol
x_{H_2}	2.29	%mol
x_{N_2}	0.18	%mol
x_{H_2O}	80.19	%mol
Inlet temperature	569.44	°C

Considering the composition and the temperature it is possible to relate the C morphology to them. In fact at the inlet the temperature is sufficiently high to promote

carbon formation via methane cracking (reaction 1.6). Further down in the reactor the methane content decreases while the CO amount increases. This can thermodynamically promote C deposition via the Boudouard reaction (reaction 1.7).

Furthermore, the different C morphology can be related to the different phases in which the Al_2O_3 support can be found. The most common form of crystalline aluminium oxide is known as corundum, which is the thermodynamically stable form and its crystalline Bravais lattice is the trigonal one. Aluminium oxide also exists in other phases, including the cubic γ and η phases, the monoclinic θ phase, the hexagonal χ phase, the orthorhombic κ phase and the δ phase that can be tetragonal or orthorhombic. Cubic $\gamma - Al_2O_3$ has important technical applications.

It is important to bear in mind that a carbon amount of less 0.4% can be considered 0. The eventual carbonaceous deposits can be the NGSR reaction intermediated which are adsorbed on the catalyst surface and not any C deposition.

An important observation after a comparative analysis of the SEM images is the different structure of the catalyst. It is not regular: in some points, it looks highly porous, in others the support seems to be fibrous; in other, it is possible to retrieve large nickel particles while in others Ni is finely dispersed.

4.4 Conclusions and further developments

It is possible to summarise the main conclusion regarding carbon deposition.

A possible explanation for the different C morphologies found in the samples is connected to the gas composition all along the reactor. Table 4.1 reports the feedstock composition for two different days. The reforming reactor is fed by two different gaseous flow: natural gas (NG) coming from the Italian national gas grid, and refinery gas (RG) coming from other unit operations in the refinery. The table highlights the presence of significant amount of CH_4 and higher hydrocarbons in the mixture;

- at the tube inlet there is a high amount of methane and heavier-then-methane compounds. In particular, the higher hydrocarbons tend to crack leading to C deposition. The C deposited is not gasified by hydrogen (which is present in small amounts since the reforming reaction has not stared or has been proceeding slow);
- at the tube outlet we see relatively high amount of C deposited. We wonder whether C deposition could be due to methane cracking (reaction 1.6), since in that area the amount of CH_4 is relatively small (the CH4 conversion is almost complete);
- otherwise C deposition could be due to the Boudouard reaction (reaction 1.7) which could take place since there is a high concentration of CO at the reactor outlet;

Also, the temperature at the reactor inlet can influence the morphology of the carbonaceous deposits. The last row of Table 4.1 shows the reformer inlet temperature. The inlet temperature is probably sufficiently high to promote the hydrocarbon cracking reactions:

- at low reaction temperature (lower than 598 K), when the rate of atomic carbon gasification exceeds that of formation, no carbon would be deposited . However, if the reaction temperature is higher than 598 K, the rate of C formation exceeds

that of C gasification, which would result in the carbon accumulation on the catalyst surface;

- at 723 K, low-density polymeric carbon and vermicular filaments are formed, while at 823 K, high-density graphitic filamentous carbon is formed on the surface, which is more stable and may retain its overall film or vermicular structure [165]. If these types of amorphous and filamentous carbons predominate the carbon-deposition process, the metal particle gradually becomes encapsulated with the inactive carbon to speed up the catalyst deactivation. In addition to encapsulation, formation of large amounts of filamentous carbon can cause other forms of catalyst deactivation, namely plugging of catalyst micro- and mesopores and reactor voids [166] and destruction of catalyst pellets. Thus, the surface properties of the catalysts deteriorated with drastic changes, especially at high reaction temperatures (823 K). Consequently, the catalytic performance declines;
- the decomposition of hydrocarbons on metal catalysts to form coke and carbons is very complex involving: (i) reactions of adsorbed carbon to form amorphous, filamentous, and graphitic carbons, and (ii) condensation of C_nH_z, radicals on the nickel surface to form a high molecular weight, polymeric coke. In addition, at sufficiently high temperatures (>873 K) thermal cracking or catalytic cracking on the support occurs, resulting in the production and deposition of carbon precursors on the catalyst particle and ultimate encapsulation of the catalyst particle with pyrolytic carbon [165];

Furthermore, the impurities of Fe and Cr on the catalyst (retrievable in Figure 4.5 and 4.6) could be connected to the solid state diffusion of steel components [164].

Regarding the catalyst support (Al_2O_3) morphology,it can be in different crystalline forms. The most common form of crystalline aluminium oxide is known as corundum, which is the thermodynamically stable form and its crystalline Bravais lattice is trigonal. Aluminium oxide also exists in other phases, including the cubic γ and η phases, the monoclinic θ phase, the hexagonal χ phase, the orthorhombic κ phase, and the δ phase that can be tetragonal or orthorhombic. In particular γ-Al_2O_3 has important technical applications. The different support morphologies can be observed in some SEM images.

Future perspectives can be related to the fact that in the way EDS is performed is not a reliable quantitative measurement, we should use different techniques to calculate the C amount in the sample. Possible quantitative techniques: burning completely the sample in a furnace and measuring the weight loss, TPO (temperature programmed oxidation). Also, other imaging techniques to analyse in detail the C form (such as Raman spectroscopy) could be used to obtain a quantitative measurement.

Bibliography

[1] C. Song, "Global challenges and strategies for control, conversion and utilization of CO2 for sustainable development involving energy, catalysis, adsorption and chemical processing", *Catalysis Today*, vol. 115, no. 1-4, pp. 2–32, 2006. DOI: 10.1016/j.cattod.2006.02.029.

[2] ——, "Introduction to Hydrogen and Syngas Production and Purification Technologies", in *Hydrogen and syngas production and purification technologies*, L. Ke, C. Song, and V. Subramani, Eds., Hoboken: John Wiley & Sons, 2010, ch. 1, pp. 1–13.

[3] "Annual Energy Review 2007", Energy Information Administration, U.S. Department of Energy, Washington D.C., Tech. Rep., 2007.

[4] M. C. Williams, J. P. Strakey, W. A. Surdoval, and L. C. Wilson, "Solid oxide fuel cell technology development in the U.S.", *Solid State Ionics*, vol. 177, pp. 2039–2044, 2006. DOI: 10.1016/j.ssi.2006.02.051.

[5] H. Gunardson, *Industrial Gases in Petrochemical Processing*, M. Dekker, Ed. New York, 1998.

[6] G. Pantoleontos, E. S. Kikkinides, and M. C. Georgiadis, "A heterogeneous dynamic model for the simulation and optimisation of the steam methane reforming reactor", *International Journal of Hydrogen Energy*, vol. 37, no. 21, pp. 16 346–16 358, 2012. DOI: 10.1016/j.ijhydene.2012.02.125.

[7] N. Z. Muradov, "Production of Hydrogen from Hydrocarbons", in *Hydrogen Fuel: Production, Transport, and Storage*, R. B. Gupta, Ed., Boca Raton: CRC Press, 2009, ch. 2, pp. 33–102, ISBN: 9781420045758.

[8] J. Xu and G. F. Froment, "Methane Steam Reforming, Methanation and Water-Gas Shift: I. Intrinsic Kinetics", *AIChE Journal*, vol. 35, no. 1, pp. 88–96, 1989. DOI: 10.1002/aic.690350109.

[9] G. Wietzel, J. Jannek, and W. Hennicke, *Process for the catalytic conversion of hydrocarbons*, 1927.

[10] G. Schiller and G. Wietzel, *Production of hydrogen from hydrocarbons*, 1932.

[11] F. J. Dent, R. G. Cockerham, and G. Percival, *Process for the production of gases containing methane from hydrocarbons*, 1959.

[12] J. R. Rostrup-Nielsen, "Catalytic Steam Reforming", in *Catalysis - Science and Technology*, J. R. Anderson and M. Boudart, Eds., New York: Springer, 1984, ch. 1, pp. 3–117.

[13] M. Twigg, *Catalyst Handbook*. Manson, 1996, p. 608, ISBN: 1874545359.

[14] Johnson Matthey, *Primary-reforming catalysts*. [Online]. Available: https://matthey.com/products-and-services/chemical-processes/chemical-catalysts/primary-reforming-catalysts.

[15] J. R. Rostrup-Nielsen, J. Sehested, and J. K. Nørskov, "Hydrogen and Synthesis Gas by Steam and CO2 Reforming", *Advances in Catalysis*, vol. 47, pp. 65–139, 2002. DOI: 10.1016/S0360-0564(02)47006-X.

[16] K. Aasberg-Petersen, I. Dybkjær, C. Ovesen, N. Schjødt, J. Sehested, and S. Thomsen, "Natural gas to synthesis gas – Catalysts and catalytic processes",

Journal of Natural Gas Science and Engineering, vol. 3, no. 2, pp. 423–459, 2011. DOI: 10.1016/j.jngse.2011.03.004.

[17] C. H. Bartholomew and R. J. Farrauto, *Fundamentals of industrial catalytic process*, second ed. Hoboken, New Jersey: Wiley Interscience, 2005, p. 994, ISBN: 9780471457138.

[18] M. Carlsson, "Carbon Formation in Steam Reforming and Effect of Potassium Promotion", *Johnson Matthey Technology Review*, vol. 59, no. 4, pp. 313–318, 2015. DOI: 10.1595/205651315X688992.

[19] S. E. Nielsen, *Ammonia - Methanation*. [Online]. Available: https://www.topsoe.com/processes/ammonia/methanation.

[20] J. Kopyscinski, T. J. Schildhauer, and S. M. Biollaz, "Production of synthetic natural gas (SNG) from coal and dry biomass - A technology review from 1950 to 2009", *Fuel*, vol. 89, no. 8, pp. 1763–1783, 2010. DOI: 10.1016/j.fuel.2010.01.027.

[21] J. Gao, Q. Liu, F. Gu, B. Liu, Z. Zhong, and F. Su, "Recent advances in methanation catalysts for the production of synthetic natural gas", *RSC Advances*, vol. 5, no. 29, pp. 22 759–22 776, 2015. DOI: 10.1039/c4ra16114a.

[22] I. Wender, "Reactions of synthesis gas", *Fuel processing technology*, vol. 48, pp. 189–297, 1996.

[23] B. Pearce, M. Twigg, and C. Woodward, "Methanation", in *Catalyst Handbook*, M. V. Twigg, Ed., second ed., Frome, UK: Wolfe Publishing Ltd, 1989, ch. Chapter 7, ISBN: 9780723408572.

[24] Z. Zhang, T. Wei, G. Chen, C. Li, D. Dong, W. Wu, Q. Liu, and X. Hu, "Understanding correlation of the interaction between nickel and alumina with the catalytic behaviors in steam reforming and methanation", *Fuel*, vol. 250, no. March, pp. 176–193, 2019. DOI: 10.1016/j.fuel.2019.04.005.

[25] R. Mauri, *Non-Equilibrium Thermodynamics in Multiphase Flows*. Springer, 2013, ISBN: 978-94-007-5460-7. DOI: 10.1007/978-94-007-5461-4.

[26] W. Wang and J. Gong, "Methanation of carbon dioxide: An overview", *Frontiers of Chemical Engineering in China*, vol. 5, no. 1, pp. 2–10, 2011. DOI: 10.1007/s11705-010-0528-3.

[27] G. Garbarino, P. Riani, L. Magistri, and G. Busca, "A study of the methanation of carbon dioxide on Ni/Al2O3 catalysts at atmospheric pressure", *International Journal of Hydrogen Energy*, vol. 39, no. 22, pp. 11 557–11 565, 2014. DOI: 10.1016/j.ijhydene.2014.05.111.

[28] G. Garbarino, D. Bellotti, P. Riani, L. Magistri, and G. Busca, "Methanation of carbon dioxide on Ru/Al2O3 and Ni/Al2O3 catalysts at atmospheric pressure: Catalysts activation, behaviour and stability", *International Journal of Hydrogen Energy*, vol. 40, no. 30, pp. 9171–9182, 2015. DOI: 10.1016/j.ijhydene.2015.05.059.

[29] G. Garbarino, C. Wang, T. Cavattoni, E. Finocchio, P. Riani, M. Flytzani-Stephanopoulos, and G. Busca, "A study of Ni/La-Al2O3 catalysts: A competitive system for CO2 methanation", *Applied Catalysis B: Environmental*, vol. 248, pp. 286–297, 2019. DOI: 10.1016/j.apcatb.2018.12.063.

[30] S. Rönsch, J. Schneider, S. Matthischke, M. Schlüter, M. Götz, J. Lefebvre, P. Prabhakaran, and S. Bajohr, "Review on methanation - From fundamentals to current projects", *Fuel*, vol. 166, pp. 276–296, 2016. DOI: 10.1016/j.fuel.2015.10.111.

[31] M. Zeppieri, P. L. Villa, N. Verdone, M. Scarsella, and P. De Filippis, "Kinetic of methane steam reforming reaction over nickel- and rhodium-based catalysts",

Applied Catalysis A: General, vol. 387, no. 1-2, pp. 147–154, 2010. DOI: 10.1016/j.apcata.2010.08.017.

[32] K. Delgado, L. Maier, S. Tischer, A. Zellner, H. Stotz, and O. Deutschmann, "Surface Reaction Kinetics of Steam- and CO2-Reforming as Well as Oxidation of Methane over Nickel-Based Catalysts", *Catalysts*, vol. 5, no. 2, pp. 871–904, 2015. DOI: 10.3390/catal5020871.

[33] M. Khzouz and E. I. Gkanas, "Experimental and Numerical Study of Low Temperature Methane Steam Reforming for Hydrogen Production", *Catalysts*, vol. 8, no. 5, 2017. DOI: 10.3390/catal8010005.

[34] N. R. Parlikkad, S. Chambrey, P. Fongarland, N. Fatah, A. Khodakov, S. Capela, and O. Guerrini, "Modeling of fixed bed methanation reactor for syngas production: Operating window and performance characteristics", *Fuel*, vol. 107, pp. 254–260, 2013. DOI: 10.1016/j.fuel.2013.01.024.

[35] D. Schlereth and O. Hinrichsen, "Chemical Engineering Research and Design A fixed-bed reactor modeling study on the methanation of CO 2", *Chemical Engineering Research and Design*, vol. 92, no. 4, pp. 702–712, 2013. DOI: 10.1016/j.cherd.2013.11.014.

[36] E. M. A. Mokheimer, M. Ibrar Hussain, S. Ahmed, M. A. Habib, and A. A. Al-Qutub, "On the Modeling of Steam Methane Reforming", *Journal of Energy Resources Technology*, vol. 137, no. 1, p. 012 001, 2014. DOI: 10.1115/1.4027962.

[37] G. Pantoleontos, G. Skevis, G. Karagiannakis, and A. G. Konstandopoulos, "A Heterogeneous Multiscale Dynamic Model for Simulation of Catalytic Reforming Reactors", *International Journal of Chemical Kinetics*, vol. 48, no. 5, pp. 239–252, 2016. DOI: 10.1002/kin.20985.

[38] F. Pugliese, A. Trucco, G. Moser, and P. Costamagna, "Diagnostics and Prognostics-Oriented Modeling of an NGSR Fuel Processor for Application in SOFC Systems", *Fuel Cells*, vol. 17, no. 4, pp. 517–534, 2017. DOI: 10.1002/fuce.201600187.

[39] S. Z. Abbas, V. Dupont, and T. Mahmud, "Modelling of high purity H2 production via sorption enhanced chemical looping steam reforming of methane in a packed bed reactor", *Fuel*, vol. 202, pp. 271–286, 2017. DOI: 10.1016/j.fuel.2017.03.072.

[40] D. Pashchenko, "Numerical study of steam methane reforming over a preheated Ni-based catalyst with detailed fluid dynamics", *Fuel*, vol. 236, pp. 686–694, 2019. DOI: 10.1016/j.fuel.2018.09.033.

[41] K. Ahmed and K. Föger, "Approach to equilibrium of the water-gas shift reaction on a Ni/zirconia anode under solid oxide fuel-cell conditions", *Journal of Power Sources*, vol. 103, no. 1, pp. 150–153, 2001. DOI: 10.1016/S0378-7753(01)00836-9.

[42] F. Bustamante, R. M. Enick, A. V. Cugini, R. P. Killmeyer, B. H. Howard, K. S. Rothenberger, M. V. Ciocco, B. D. Morreale, S. Chattopadhyay, and S. Shi, "High-temperature kinetics of the homogeneous reverse water-gas shift reaction", *AIChE Journal*, vol. 50, no. 5, pp. 1028–1041, 2004. DOI: 10.1002/aic.10099.

[43] F. Bustamante, R. M. Enick, R. P. Killmeyer, B. H. Howard, K. S. Rothenberger, A. V. Cugini, B. D. Morreale, and M. V. Ciocco, "Uncatalyzed and wall-catalyzed forward water-gas shift reaction kinetics", *AIChE Journal*, vol. 51, no. 5, pp. 1440–1454, 2005. DOI: 10.1002/aic.10396.

[44] A. Adrados, A. Lopez-Urionabarrenechea, E. Acha, J. Solar, B. M. Caballero, and I. de Marco, "Hydrogen rich reducing gases generation in the production of charcoal from woody biomass carbonization", *Energy Conversion and Management*, vol. 148, pp. 352–359, 2017. DOI: 10.1016/j.enconman.2017.06.010.

[45] S. J. K. Forrest, J. G. Oliver, S. A. French, and M. P. U. Carlsson, *Catalyst preparation method*, 2016.

[46] J. Cross, G. Jones, and M. A. Kent, "An introduction to pre-reforming catalysis", in *Nitrogen+Syngas 341*, 2016, pp. 40–48.

[47] G. Garbarino, S. Chitsazan, T. K. Phung, P. Riani, and G. Busca, "Preparation of supported catalysts: A study of the effect of small amounts of silica on Ni/Al2O3 catalysts", *Applied Catalysis A: General*, vol. 505, pp. 86–97, 2015. DOI: 10.1016/j.apcata.2015.07.017.

[48] H. S. Fogler, *Elements of Chemical Reaction Engineering*, fourth ed. Upper Saddle River, New Jersey: Prentice Hall, 2005, ISBN: 9780130473944.

[49] O. Levenspiel, *Chemical Reaction Engineering*, third ed. New York, New York: John Wiley & Sons, 1999, ISBN: 047125424X. DOI: 10.1016/0009-2509(64)85017-X. [Online]. Available: http://pubs.acs.org/doi/abs/10.1021/ie990488g.

[50] N. O. Lemcoff, S. I. Pereira Duarte, and O. M. Martinez, "Heat transfer in packed beds", *Reviews in Chemical Engineering*, vol. 6, no. 4, pp. 229–292, 1990.

[51] G. W. Koning, "Heat and mass transport in tubular packed bed reactors at reacting and non-reacting conditions. Experiments and models", PhD thesis, University of Twente, 2002, p. 297, ISBN: 903651813X.

[52] G. F. Froment, K. B. Bischoff, and J. De Wilde, *Chemical Reactor Analysis and Design*, third ed. John Wiley & Sons, 2011, ISBN: 9780470565414.

[53] K. R. Rout and H. A. Jakobsen, "A numerical study of fixed bed reactor modelling for steam methane reforming process", *Canadian Journal of Chemical Engineering*, vol. 93, no. 7, pp. 1222–1238, 2015. DOI: 10.1002/cjce.22202.

[54] E. L. Oliveira, C. A. Grande, and A. E. Rodrigues, "Steam methane reforming in a Ni/Al2O3 Catalyst: Kinetics and diffusional limitations in extrudates", *Canadian Journal of Chemical Engineering*, vol. 87, no. 6, pp. 945–956, 2009. DOI: 10.1002/cjce.20223.

[55] B. T. Schädel, M. Duisberg, and O. Deutschmann, "Steam reforming of methane, ethane, propane, butane, and natural gas over a rhodium-based catalyst", *Catalysis Today*, vol. 142, no. 1-2, pp. 42–51, 2009. DOI: 10.1016/j.cattod.2009.01.008.

[56] S. Z. Abbas, V. Dupont, and T. Mahmud, "Kinetics study and modelling of steam methane reforming process over a NiO/Al2O3 catalyst in an adiabatic packed bed reactor", *International Journal of Hydrogen Energy*, vol. 42, no. 5, pp. 2889–2903, 2017. DOI: 10.1016/j.ijhydene.2016.11.093.

[57] I. Champon, A. Bengaouer, A. Chaise, S. Thomas, and A.-C. Roger, "Carbon dioxide methanation kinetic model on a commercial Ni/Al2O3 catalyst", *Journal of CO2 Utilization*, vol. 34, no. March, pp. 256–265, 2019. DOI: 10.1016/j.jcou.2019.05.030. [Online]. Available: https://doi.org/10.1016/j.jcou.2019.05.030.

[58] G. W. Koning, A. E. Kronberg, and W. P. M. Van Swaaij, "Improved one-dimensional model of a tubular packed bed reactor", *Chemical Engineering Science*, vol. 61, no. 10, pp. 3167–3175, 2006. DOI: 10.1016/j.ces.2005.11.057.

[59] A.G. Dixon, "Thermal resistance models of packed-bed effective heat transfer parameters", *AIChE Journal*, vol. 31, no. 5, pp. 826–834, 1985. DOI: 10.1002/aic.690310519.

[60] Y. A. Cengel, *Heat Transfer*, second ed. New York: McGraw-Hill, 2003, ISBN: 9780072456733.

[61] P. N. Dwivedi and S. N. Upadhyay, "Particle-Fluid Mass Transfer in Fixed and Fluidized Beds", *Industrial and Engineering Chemistry Process Design and Development*, vol. 16, no. 2, pp. 157–165, 1977. DOI: 10.1021/i260062a001.

[62] R. H. Perry and D. W. Green, *Perry's Chemical Engineers' Handbook*, eighth ed. New York, New York: McGraw-Hill, 2008.

[63] P. Zehner and E. U. Schlünder, "Warmeleitfahigkeit von Schuttungen bei mässigen Temperaturen", *Chemie Ingenieur Technik*, vol. 42, pp. 933–941, 1970.

[64] W. Van Antwerpen, C. G. Du Toit, and P. G. Rousseau, "A review of correlations to model the packing structure and effective thermal conductivity in packed beds of mono-sized spherical particles", *Nuclear Engineering and Design*, vol. 240, no. 7, pp. 1803–1818, 2010. DOI: 10.1016/j.nucengdes.2010.03.009.

[65] P. Cheng and C. T. Hsu, "Fully-developed, forced convective flow through an annular packed-sphere bed with wall effects", *International Journal of Heat and Mass Transfer*, vol. 29, no. 12, pp. 1843–1853, 1986. DOI: 10.1016/0017-9310(86)90003-7.

[66] N. P. Bansal and R. H. Doremus, *Handbook of Glass Properties*. Orlando, Florida: Academic Press Inc, 1986, pp. 1–680, ISBN: 9780080523767. DOI: 10.1016/C2009-0-21785-5.

[67] S. N. Gupta, R. B. Chaube, and S. N. Upadhyay, "Fluid-particle heat transfer in fixed and fluidized beds", *Chemical Engineering Science*, vol. 29, no. 3, pp. 839–843, 1974. DOI: 10.1016/0009-2509(74)80203-4.

[68] N. Wakao, S. Kaguei, and T. Funazkri, "Effect of fluid dispersion coefficients on particle-to-fluid heat transfer coefficients in packed beds. Correlation of nusselt numbers", *Chemical Engineering Science*, vol. 34, no. 3, pp. 325–336, 1979. DOI: 10.1016/0009-2509(79)85064-2.

[69] D. J. Gunn, "Transfer of heat or mass to particles in fixed and fluidised beds", *International Journal of Heat and Mass Transfer*, vol. 21, no. 4, pp. 467–476, 1978. DOI: 10.1016/0017-9310(78)90080-7.

[70] N. G. Deen, E. A. Peters, J. T. Padding, and J. A. Kuipers, "Review of direct numerical simulation of fluid-particle mass, momentum and heat transfer in dense gas-solid flows", *Chemical Engineering Science*, vol. 116, pp. 710–724, 2014. DOI: 10.1016/j.ces.2014.05.039.

[71] N. G. Deen, S. H. L. Kriebitzsch, M. A. van der Hoef, and J. A. M. Kuipers, "Direct numerical simulation of flow and heat transfer in dense fluid-particle systems", *Chemical Engineering Science*, vol. 81, pp. 329–344, 2012. DOI: 10.1016/j.ces.2012.06.055.

[72] B. Sun, S. Tenneti, and S. Subramaniam, "Modeling average gas-solid heat transfer using particle-resolved direct numerical simulation", *International Journal of Heat and Mass Transfer*, vol. 86, pp. 898–913, 2015. DOI: 10.1016/j.ijheatmasstransfer.2015.03.046.

[73] S. Tenneti, B. Sun, R. Garg, and S. Subramaniam, "Role of fluid heating in dense gas-solid flow as revealed by particle-resolved direct numerical simulation", *International Journal of Heat and Mass Transfer*, vol. 58, no. 1-2, pp. 471–479, 2013. DOI: 10.1016/j.ijheatmasstransfer.2012.11.006.

[74] A. Singhal, S. Cloete, S. Radl, R. Quinta-Ferreira, and S. Amini, "Heat transfer to a gas from densely packed beds of monodisperse spherical particles", *Chemical Engineering Journal*, vol. 314, pp. 27–37, 2016. DOI: 10.1016/j.cej.2016.12.124.

[75] A. Jourak, V. Frishfelds, J. G. I. Hellström, T. S. Lundström, I. Herrmann, and A. Hedström, "Longitudinal Dispersion Coefficient: Effects of Particle-Size Distribution", *Transport in Porous Media*, vol. 99, no. 1, pp. 1–16, 2013. DOI: 10.1007/s11242-013-0159-5.

[76] D. J. Gunn, "Axial and radial dispersion in fixed beds", *Chemical Engineering Scienc*, vol. 42, no. 2, pp. 363–373, 1987. DOI: 10.1016/0009-2509(87)85066-2.

[77] P. Y. Lanfrey, Z. V. Kuzeljevic, and M. P. Dudukovic, "Tortuosity model for fixed beds randomly packed with identical particles", *Chemical Engineering Science*, vol. 65, no. 5, pp. 1891–1896, 2010. DOI: 10.1016/j.ces.2009.11.011.

[78] L. C. Young and B. A. Finlayson, "Axial Dispersion in Nonisothermal Packed Bed Chemical Reactors", *Industrial and Engineering Chemistry Fundamentals*, vol. 12, no. 4, pp. 412–422, 1973. DOI: 10.1021/i160048a004.

[79] R. Khanna and J. H. Seinfeld, "Mathematical modeling of packed bed reactors: Numerical solutions and control model development", *Advances in Chemical Engineering*, vol. 13, no. C, pp. 113–191, 1987. DOI: 10.1016/S0065-2377(08)60017-4.

[80] S. Yagi, D. Kunii, and N. Wakao, "Studies on axial effective thermal conductivities in packed beds", *AIChE Journal*, vol. 6, no. 4, pp. 543–546, 1960. DOI: 10.1002/aic.690060407.

[81] K. B. Bischoff, "Axial thermal conductivities in packed beds", *The Canadian Journal of Chemical Engineering*, vol. 40, no. 4, pp. 161–163, 1962. DOI: 10.1002/cjce.5450400408.

[82] R. Krupiczka, "Analysis of thermal conductivity in granular materials", *International chemical engineering*, vol. 7, no. 1, pp. 122–144, 1967.

[83] J. Votruba, V. Hlaváček, and M. Marek, "Packed bed axial thermal conductivity", *Chemical Engineering Science*, vol. 27, no. 10, pp. 1845–1851, 1972. DOI: 10.1016/0009-2509(72)85046-2.

[84] R. L. Keiski, O. Desponds, Y. F. Chang, and G. A. Somorjai, "Kinetics of the water-gas shift reaction over several alkane activation and water-gas shift catalysts", *Applied Catalysis A, General*, vol. 101, no. 2, pp. 317–338, 1993. DOI: 10.1016/0926-860X(93)80277-W.

[85] F. A. Fernandes and A. B. Soares, "Modeling of methane steam reforming in a palladium membrane reactor", *Fuel*, vol. 85, pp. 569–573, 2006. DOI: 10.1016/j.fuel.2005.08.002.

[86] E. L. Oliveira, C. A. Grande, and A. E. Rodrigues, "Methane steam reforming in large pore catalyst", *Chemical Engineering Science*, vol. 65, no. 5, pp. 1539–1550, 2010. DOI: 10.1016/j.ces.2009.10.018.

[87] L. Lao, A. Aguirre, A. Tran, Z. Wu, H. Durand, and P. D. Christofides, "CFD modeling and control of a steam methane reforming reactor", *Chemical Engineering Science*, vol. 148, pp. 78–92, 2016. DOI: 10.1016/j.ces.2016.03.038.

[88] A. Tran, A. Aguirre, H. Durand, M. Crose, and P. D. Christofides, "CFD modeling of a industrial-scale steam methane reforming furnace", *Chemical Engineering Science*, vol. 171, pp. 576–598, 2017. DOI: 10.1016/j.ces.2017.06.001.

[89] S. D. Angeli, G. Monteleone, A. Giaconia, and A. A. Lemonidou, "State-of-the-art catalysts for CH4 steam reforming at low temperature", *International Journal of Hydrogen Energy*, vol. 39, no. 5, pp. 1979–1997, 2014. DOI: 10.1016/j.ijhydene.2013.12.001.

[90] A. Sorce, A. Greco, L. Magistri, and P. Costamagna, "FDI oriented modeling of an experimental SOFC system, model validation and simulation of faulty states", *Applied Energy*, vol. 136, pp. 894–908, 2014. DOI: 10.1016/j.apenergy.2014.03.074.

[91] A. Greco, A. Sorce, R. Littwin, P. Costamagna, and L. Magistri, "Reformer faults in SOFC systems: Experimental and modeling analysis, and simulated fault maps", *International Journal of Hydrogen Energy*, vol. 39, no. 36, pp. 21 700–21 713, 2014. DOI: 10.1016/j.ijhydene.2014.09.063.

[92] P. Polverino, C. Pianese, M. Sorrentino, and D. Marra, "Model-based development of a fault signature matrix to improve solid oxide fuel cell systems on-site diagnosis", *Journal of Power Sources*, vol. 280, pp. 320–338, 2015. DOI: 10.1016/j.jpowsour.2015.01.037.

[93] K. Sasaki and Y. Teraoka, "Equilibria in fuel cell gases. I. Equilibrium compositions and reforming conditions", *Journal of the Electrochemical Society*, vol. 150, no. 7, pp. 878–884, 2003. DOI: 10.1149/1.1577337.

[94] J. G. McCarty and H. Wise, "Hydrogenation of surface carbon on alumina-supported nickel", *Journal of Catalysis*, vol. 57, no. 3, pp. 406–416, 1979. DOI: 10.1016/0021-9517(79)90007-1.

[95] S. Helveg, J. Sehested, and J. R. Rostrup-Nielsen, "Whisker carbon in perspective", *Catalysis Today*, vol. 178, no. 1, pp. 42–46, 2011. DOI: 10.1016/j.cattod.2011.06.023.

[96] D. L. Trimm, "Catalysts for the control of coking during steam reforming", *Catalysis Today*, vol. 49, no. 1-3, pp. 3–10, 1999. DOI: 10.1016/S0920-5861(98)00401-5.

[97] J. R. Rostrup-Nielsen, "Sulfur-passivated nickel catalysts for carbon-free steam reforming of methane", *Journal of Catalysis*, vol. 85, no. 1, pp. 31–43, 1984. DOI: 10.1016/0021-9517(84)90107-6.

[98] J. W. Snoeck, G. F. Froment, and M. Fowles, "Kinetic study of the carbon filament formation by methane cracking on a nickel catalyst", *Journal of Catalysis*, vol. 169, no. 1, pp. 250–262, 1997. DOI: 10.1006/jcat.1997.1635.

[99] J. Xu and G. F. Froment, "Methane steam reforming: II. Diffusional limitations and reactor simulation", *AIChE Journal*, vol. 35, no. 1, pp. 97–103, 1989. DOI: 10.1002/aic.690350110.

[100] M. Behnam, A. G. Dixon, P. M. Wright, M. Nijemeisland, and E. H. Stitt, "Comparison of CFD simulations to experiment under methane steam reforming reacting conditions", *Chemical Engineering Journal*, vol. 207-208, pp. 690–700, 2012. DOI: 10.1016/j.cej.2012.07.038.

[101] J. H. Ghouse and T. A. Adams, "A multi-scale dynamic two-dimensional heterogeneous model for catalytic steam methane reforming reactors", *International Journal of Hydrogen Energy*, vol. 38, no. 24, pp. 9984–9999, 2013. DOI: 10.1016/j.ijhydene.2013.05.170.

[102] H. Ebrahimi, A. Zamaniyan, R. Hosseini, and K. Forsat, "Analysis of reformer furnace tubes for hydrogen production using radiative zonal model", *International Journal of Hydrogen Energy*, vol. 39, no. 25, pp. 13 164–13 173, 2014. DOI: 10.1016/j.ijhydene.2014.06.131.

[103] A. Baldinelli, L. Barelli, G. Bidini, A. Di Michele, and R. Vivani, "SOFC direct fuelling with high-methane gases: Optimal strategies for fuel dilution and upgrade to avoid quick degradation", *Energy Conversion and Management*, vol. 124, pp. 492–503, 2016. DOI: 10.1016/j.enconman.2016.07.051.

[104] V. N. Nguyen, R. Deja, R. Peters, and L. Blum, "Methane/steam global reforming kinetics over the Ni/YSZ of planar pre-reformers for SOFC systems", *Chemical Engineering Journal*, vol. 292, pp. 113–122, 2016. DOI: 10.1016/j.cej.2016.01.087.

[105] P. Costamagna, S. Rossi, F. Pugliese, F. Gugliotta, and A. Enrico, "FDI Oriented Simulation of an MSR Reactor for Application in SOFC Systems", *ECS Transactions*, vol. 68, no. 1, pp. 3143–3150, 2015. DOI: 10.1149/06801.3143ecst.

[106] V. Venkatasubramanian, R. Rengaswamy, K. Yin, and S. N. Kavuri, "Multiple faults detection using artificial neural network", *Computers & Chemical Engineering*, vol. 27, pp. 293–311, 2003.

[107] P. Costamagna, A. De Giorgi, L. Magistri, G. Moser, L. Pellaco, and A. Trucco, "A Classification Approach for Model-Based Fault Diagnosis in Power Generation Systems Based on Solid Oxide Fuel Cells", *IEEE Transactions on Energy Conversion*, vol. 31, no. 2, pp. 676–687, 2016. DOI: 10.1109/TEC.2015.2492938.

[108] I. Dybkjær, "Tubular reforming and autothermal reforming of natural gas - an overview of available processes", *Fuel Processing Technology*, vol. 42, pp. 85–107, 1995.

[109] P. Sadooghi and R. Rauch, "Experimental and modeling study of catalytic steam reforming of methane mixture with propylene in a packed bed reactor", *International Journal of Heat and Mass Transfer*, vol. 78, no. 2014, pp. 515–521, 2014. DOI: 10.1016/j.ijheatmasstransfer.2014.06.084.

[110] A. M. Amin, E. Croiset, and W. Epling, "Review of methane catalytic cracking for hydrogen production", *International Journal of Hydrogen Energy*, vol. 36, no. 4, pp. 2904–2935, 2011. DOI: 10.1016/j.ijhydene.2010.11.035.

[111] M. W. J. Chase, *NIST-JANAF Thermochemical Tables*. Woodbury, New York: American Chemical Society, 1998, vol. Part I, p. 1952, ISBN: 9781563968193.

[112] X. Huang and R. Reimert, "Kinetics of steam reforming of ethane on Ni/YSZ (yttria-stabilised zirconia) catalyst", *Fuel*, vol. 106, pp. 380–387, 2013. DOI: 10.1016/j.fuel.2012.09.081. [Online]. Available: http://dx.doi.org/10.1016/j.fuel.2012.09.081.

[113] P. S. Bulutoglu, S. Koc, and A. K. Avci, "Simulation of exhaust gas reforming of natural gas in a microchannel reactor", *International Journal of Hydrogen Energy*, vol. 41, no. 19, pp. 8184–8192, 2016. DOI: 10.1016/j.ijhydene.2015.10.126.

[114] M. Seong, M. Shin, J. H. Cho, Y. C. Lee, Y. K. Park, and J. K. Jeon, "Reactor sizing for butane steam reforming over Ni and Ru catalysts", *Korean Journal of Chemical Engineering*, vol. 31, no. 3, pp. 412–418, 2014. DOI: 10.1007/s11814-013-0225-2.

[115] D. C. Gardner and C. H. Bartholomew, "Kinetics of Carbon Deposition During Methanation of CO", *Industrial & Engineering Chemistry, Product Research and Development*, vol. 20, no. 1, pp. 80–87, 1981. DOI: 10.1021/i300001a007.

[116] W. J. Jang, D. W. Jeong, J. O. Shim, H. M. Kim, H. S. Roh, I. H. Son, and S. J. Lee, "Combined steam and carbon dioxide reforming of methane and side reactions: Thermodynamic equilibrium analysis and experimental application", *Applied Energy*, vol. 173, pp. 80–91, 2016. DOI: 10.1016/j.apenergy.2016.04.006.

[117] P. B. Tøttrup, "Kinetics of decomposition of carbon monoxide on a supported nickel catalyst", *Journal of Catalysis*, vol. 42, no. 1, pp. 29–36, 1976. DOI: 10.1016/0021-9517(76)90087-7.

[118] G. Garbarino, D. Bellotti, E. Finocchio, L. Magistri, and G. Busca, "Methanation of carbon dioxide on Ru/Al2O3 : Catalytic activity and infrared study", *Catalysis Today*, vol. 277, pp. 21–28, 2016. DOI: 10.1016/j.cattod.2015.12.010.

[119] A. G. Dixon, M. Nijemeisland, and E. H. Stitt, "Packed Tubular Reactor Modeling and Catalyst Design using Computational Fluid Dynamics", *Advances in Chemical Engineering*, vol. 31, no. 06, pp. 307–389, 2006. DOI: 10.1016/S0065-2377(06)31005-8.

[120] J. Tobiś, "Influence of bed geometry on its frictional resistance under turbulent flow conditions", *Chemical Engineering Science*, vol. 55, no. 22, pp. 5359–5366, 2000. DOI: 10.1016/S0009-2509(00)00155-X.

[121] H. M. Kvamsdal, H. F. Svendsen, T. Hertzberg, and O. Olsvik, "Dynamic simulation and optimization of a catalytic steam reformer", *Chemical Engineering Science*, vol. 54, no. 13-14, pp. 2697–2706, 1999. DOI: 10.1016/S0009-2509(98)00329-7.

[122] M. N. Pedernera, J. Piña, D. O. Borio, and V. Bucalá, "Use of a heterogeneous two-dimensional model to improve the primary steam reformer performance", *Chemical Engineering Journal*, vol. 94, no. 1, pp. 29–40, 2003. DOI: 10.1016/S1385-8947(03)00004-4.

[123] O. Bey and G. Eigenberger, "Fluid flow through catalyst filled tubes", *Chemical Engineering Science*, vol. 52, no. 8, pp. 1365–1376, 1997. DOI: 10.1016/S0009-2509(96)00509-X.

[124] M. Giese, K. Rottschäfer, and D. Vortmeyer, "Measured and Modeled Superficial Flow Profiles in Packed Beds with Liquid Flow", *AIChE Journal*, vol. 44, no. 2, pp. 484–490, 1998. DOI: 10.1002/aic.690440225.

[125] M. Winterberg, E. Tsotsas, A. Krischke, and D. Vortmeyer, "A simple and coherent set of coefficients for modelling of heat and mass transport with and without chemical reaction in tubes filled with spheres", *Chemical Engineering Science*, vol. 55, no. 5, pp. 967–979, 2000. DOI: 10.1016/S0009-2509(99)00379-6.

[126] K. Hou and R. Hughes, "The kinetics of methane steam reforming over a Ni/α-Al2O catalyst", *Chemical Engineering Journal*, vol. 82, pp. 311–328, 2001.

[127] M. Maestri, D. G. Vlachos, A. Beretta, G. Groppi, and E. Tronconi, "Steam and dry reforming of methane on Rh: Microkinetic analysis and hierarchy of kinetic models", *Journal of Catalysis*, vol. 259, no. 2, pp. 211–222, 2008. DOI: 10.1016/j.jcat.2008.08.008.

[128] M. H. Halabi, M. H. De Croon, J. Van Der Schaaf, P. D. Cobden, and J. C. Schouten, "Intrinsic kinetics of low temperature catalytic methane-steam reforming and water-gas shift over Rh/CeαZr1-αO2 catalyst", *Applied Catalysis A: General*, vol. 389, no. 1-2, pp. 80–91, 2010. DOI: 10.1016/j.apcata.2010.09.005.

[129] S. S. E. H. Elnashaie, A. S. Al-Ubaid, M. A. Soliman, and A. M. Adris, "On the kinetics and reactor modelling of the stream reforming of methane - a review", *Journal of engineering sciences*, vol. 14, no. 2, pp. 247–273, 1988.

[130] C. Sprung, B. Arstad, and U. Olsbye, "Methane steam reforming over a Ni/Nial2o4 model catalyst - Kinetics", *ChemCatChem*, vol. 6, no. 7, pp. 1969–1982, 2014. DOI: 10.1002/cctc.201402017.

[131] L. M. Aparicio, "Transient isotopic studies and microkinetic modeling of methane reforming over nickel catalysts", *Journal of Catalysis*, vol. 165, no. 2, pp. 262–274, 1997. DOI: 10.1006/jcat.1997.1468.

[132] J. Wei and E. Iglesia, "Isotopic and kinetic assessment of the mechanism of reactions of CH4 with CO2 or H2O to form synthesis gas and carbon on nickel catalysts", *Journal of Catalysis*, vol. 224, no. 2, pp. 370–383, 2004. DOI: 10.1016/j.jcat.2004.02.032.

[133] W. Akers and D. Camp, "Kinetics of the Methane-steam Reaction", *AIChE Journal*, vol. 4, no. 1, pp. 471–475, 1955.

[134] T. Osaki, T. Horiuchi, K. Suzuki, and T. Mori, "CH4/CD4 isotope effect on the reaction of adsorbed hydrocarbon species in CO2-reforming over Ni/Al2O3 catalyst", *Catalysis Letters*, vol. 44, no. 1-2, pp. 19–21, 1997.

[135] H. S. Bengaard, J. K. Nørskov, J. Sehested, B. S. Clausen, L. P. Nielsen, A. M. Molenbroek, and J. R. Rostrup-Nielsen, "Steam reforming and graphite formation on Ni catalysts", *Journal of Catalysis*, vol. 209, no. 2, pp. 365–384, 2002. DOI: 10.1006/jcat.2002.3579.

[136] D. W. Blaylock, Y. A. Zhu, and W. H. Green, "Computational investigation of the thermochemistry and kinetics of steam methane reforming over a multifaceted nickel catalyst", *Topics in Catalysis*, vol. 54, no. 13-15, pp. 828–844, 2011. DOI: 10.1007/s11244-011-9704-z.

[137] S. Wahl, A. G. Segarra, P. Horstmann, M. Carré, W. G. Bessler, F. Lapicque, and K. A. Friedrich, "Modeling of a thermally integrated 10 kWe planar solid oxide fuel cell system with anode offgas recycling and internal reforming by discretization in flow direction", *Journal of Power Sources*, vol. 279, pp. 656–666, 2015. DOI: 10.1016/j.jpowsour.2014.12.084.

[138] E. Achenbach and E. Riensche, "Methane/steam reforming kinetics for solid oxide fuel cells", *Journal of Power Sources*, vol. 52, no. 2, pp. 283–288, 1994. DOI: 10.1016/0378-7753(94)02146-5.

[139] P. Aguiar, C. S. Adjiman, and N. P. Brandon, "Anode-supported intermediate temperature direct internal reforming solid oxide fuel cell. I: Model-based steady-state performance", *Journal of Power Sources*, vol. 138, no. 1-2, pp. 120–136, 2004. DOI: 10.1016/j.jpowsour.2004.06.040.

[140] B. Wang, J. Zhu, and Z. Lin, "A theoretical framework for multiphysics modeling of methane fueled solid oxide fuel cell and analysis of low steam methane reforming kinetics", *Applied Energy*, vol. 176, pp. 1–11, 2016. DOI: 10.1016/j.apenergy.2016.05.049.

[141] B. X. Wang, Z. Jiang, and Z. J. Lin, "Multi-physics modeling of solid oxide fuel cell fueled by methane and analysis of carbon deposition", *Chinese Journal of Chemical Physics*, vol. 28, no. 3, pp. 299–307, 2015. DOI: 10.1063/1674-0068/28/cjcp1503033.

[142] A. L. Dicks, "Advances in catalysts for internal reforming in high temperature fuel cells", *Journal of Power Sources*, vol. 71, no. 1-2, pp. 111–122, 1998. DOI: 10.1016/S0378-7753(97)02753-5.

[143] A. L. Dicks, K. D. Pointon, and A. Siddle, "Intrinsic reaction kinetics of methane steam reforming on a nickel/zirconia anode", *Journal of Power Sources*, no. 86, pp. 523–530, 2000.

[144] S. Bebelis, A. Zeritis, C. Tiropani, and S. G. Neophytides, "Intrinsic Kinetics of the Internal Steam Reforming of CH4 over a Ni-YSZ-Cermet Catalyst-Electrode", *Industrial & Engineering Chemistry Research*, vol. 39, no. 12, pp. 4920–4927, 2000. DOI: 10.1021/ie000350u.

[145] H. Yakabe, T. Ogiwara, M. Hishinuma, and I. Yasuda, "3-D model calculation for planar SOFC", *Journal of Power Sources*, vol. 102, no. 1-2, pp. 144–154, 2001. DOI: 10.1016/S0378-7753(01)00792-3.

[146] R. Peters, R. Dahl, U. Klüttgen, C. Palm, and D. Stolten, "Internal reforming of methane in solid oxide fuel cell systems", *Journal of Power Sources*, vol. 106, no. 1-2, pp. 238–244, 2002. DOI: 10.1016/S0378-7753(01)01039-4.

[147] S. D. Angeli, F. G. Pilitsis, and A. A. Lemonidou, "Methane steam reforming at low temperature: Effect of light alkanes' presence on coke formation", *Catalysis Today*, vol. 242, no. Part A, pp. 119–128, 2015. DOI: 10.1016/j.cattod.2014.05.043.

[148] D. L. Trimm, "Coke formation and minimisation during steam reforming reactions", *Catalysis Today*, vol. 37, no. 3, pp. 233–238, 1997. DOI: 10.1016/S0920-5861(97)00014-X.

[149] T. S. Christensen, "Adiabatic prereforming of hydrocarbons - An important step in syngas production", *Applied Catalysis A: General*, vol. 138, no. 2, pp. 285–309, 1996. DOI: 10.1016/0926-860X(95)00302-9.

[150] P. B. Tøttrup, "Evaluation of Intrinsic Steam Reforming Kinetic Parameters from Rate Measurement on Full Particle Size", *Applied Catalysis*, vol. 4, pp. 377–389, 1982.

[151] J. R. Rostrup-Nielsen, "Activity of nickel catalysts for steam reforming of hydrocarbons", *Journal of Catalysis*, vol. 31, no. 2, pp. 173–199, 1973. DOI: 10.1016/0021-9517(73)90326-6.

[152] Y. Li, X. Wang, C. Xie, and C. Song, "Influence of ceria and nickel addition to alumina-supported Rh catalyst for propane steam reforming at low temperatures", *Applied Catalysis A: General*, vol. 357, no. 2, pp. 213–222, 2009. DOI: 10.1016/j.apcata.2009.01.025.

[153] S. G. Zavarukhin and G. G. Kuvshinov, "The kinetic model of formation of nanofibrous carbon from CH4-H2 mixture over a high-loaded nickel catalyst with consideration for the catalyst deactivation", *Applied Catalysis A: General*, vol. 272, no. 1-2, pp. 219–227, 2004. DOI: 10.1016/j.apcata.2004.05.044.

[154] ——, "Mathematic modeling of the process of production of nanofibrous carbon from methane in an isothermal reactor with a fixed bed of the Ni-Al2O3 catalyst", *Chemical Engineering Journal*, vol. 120, no. 3, pp. 139–147, 2006. DOI: 10.1016/j.cej.2006.03.004.

[155] K. Faungnawakij, R. Kikuchi, and K. Eguchi, "Thermodynamic evaluation of methanol steam reforming for hydrogen production", *Journal of Power Sources*, vol. 161, no. 1, pp. 87–94, 2006. DOI: 10.1016/j.jpowsour.2006.04.091.

[156] L. Zhu, L. Li, Z. Zhang, H. Chen, L. Zhang, and F. Wang, "Thermodynamics of Hydrogen Production Based on Coal Gasification Integrated with a Dual Chemical Looping Process", *Chemical Engineering and Technology*, vol. 39, no. 10, pp. 1912–1920, 2016. DOI: 10.1002/ceat.201400609.

[157] J. H. Koh, B. S. Kang, H. C. Lim, and Y. S. Yoo, "Thermodynamic analysis of carbon deposition and electrochemical oxidation of methane for SOFC anodes", *Electrochemical and Solid-State Letters*, vol. 4, no. 2, pp. 12–15, 2001. DOI: 10.1149/1.1339237.

[158] T. Takeguchi, Y. Kani, T. Yano, R. Kikuchi, K. Eguchi, K. Tsujimoto, Y. Uchida, A. Ueno, K. Omoshiki, and M. Aizawa, "Study on steam reforming of CH4 and C2 hydrocarbons and carbon deposition on Ni-YSZ cermets", *Journal of Power Sources*, vol. 112, no. 2, pp. 588–595, 2002. DOI: 10.1016/S0378-7753(02)00471-8.

[159] *COMSOL Multiphysics®*. [Online]. Available: https://www.comsol.com/comsol-multiphysics.

[160] A.-L. Sauvet and J. T. S. Irvine, "Catalytic and Electrocatalytic Studies of New Type of Anode Materials for SOFC under Methane", in *5th European Solid Oxide Fuel Cell Forum*, J. Huijsmans, Ed., Lucerne, 2002, pp. 490–498.

[161] M. K. Van Der Lee, A. J. Van Dillen, J. W. Geus, K. P. De Jong, and J. H. Bitter, "Catalytic growth of macroscopic carbon nanofiber bodies with high bulk density and high mechanical strength", *Carbon*, vol. 44, no. 4, pp. 629–637, 2006, ISSN: 00086223. DOI: 10.1016/j.carbon.2005.09.031.

[162] S. Helveg, J. Sehested, and J. R. Rostrup-Nielsen, "Whisker carbon in perspective", *Catalysis Today*, vol. 178, no. 1, pp. 42–46, 2011, ISSN: 09205861. DOI: 10.1016/j.cattod.2011.06.023.

[163] Z. Zeng and K. Natesan, "Relationship between the growth of carbon nanofilaments and metal dusting corrosion", *Chemistry of Materials*, vol. 17, no. 14, pp. 3794–3801, 2005, ISSN: 08974756. DOI: 10.1021/cm050712u.

[164] D. J. Young and J. Zhang, "Carbon corrosion of alloys at high temperature", *Journal of the Southern African Institute of Mining and Metallurgy*, vol. 113, no. 2, pp. 149–154, 2013, ISSN: 22256253.

[165] C. H. Bartholomew, "Carbon Deposition in Steam Reforming and Methanation", *Catalysis Reviews: Science and Engineering*, vol. 24, no. 1, pp. 67–112, 1982, ISSN: 0161-4940. DOI: http://dx.doi.org/10.1080/03602458208079650.

[166] E. J. Erekson, E. L. Sughrue, and C. H. Bartholomew, "Catalyst degradation in high temperature methanation", *Fuel Processing Technology*, vol. 5, no. 1-2, pp. 91–101, 1981, ISSN: 03783820. DOI: 10.1016/0378-3820(81)90023-0.